

# Photoassociation of $^{40}\text{Ca}$ at high laser intensities

Von der QUEST-Leibniz-Forschungsschule  
der Gottfried Wilhelm Leibniz Universität Hannover  
zur Erlangung des Grades

Doktor der Naturwissenschaften

Dr. rer. nat.

genehmigte Dissertation

von

MSc. Veit Peter Dahlke

geboren am 12. 03. 1988 in Magdeburg

Erscheinungsjahr 2020

**Referent:** Prof. Dr. rer. nat. Eberhard Tiemann  
Leibniz Universität Hannover

**1. Korreferent:** Prof. Dr. rer. nat. Fritz Riehle  
Physikalisch-Technische Bundesanstalt

**2. Korreferent:** Prof. Dr. rer. nat. Andreas Hemmerich  
Universität Hamburg

**Tag der Promtion:** 25.02.2020

# Zusammenfassung

In dieser Arbeit präsentiere ich die Ergebnisse von Photoassoziationsmessungen in Ensembles von atomaren Calcium über einen Intensitätsbereich von 1 - 600 W/cm<sup>2</sup>. Die Temperatur der Atome wurde mit der Hilfe von Laser- und evaporativer Kühlung auf 1  $\mu$ K reduziert. Anschließend wurden die beiden am schwächsten gebundenen Zustände in den angeregten Molekülpotentialen, welche zur Asymptote  $^3P_1+^1S_0$  dissoziieren, bezüglich des Linienprofils der gemessenen Resonanzen und der absoluten Verlustrate untersucht. Die Untersuchung ergab, dass die gemessenen Raten mehr als eine Größenordnung kleiner sind als theoretische Berechnungen vorhersagen. Die Vorhersagen basieren auf einem Streuformalismus von Bohn & Julienne und den Wellenfunktionen der Quantenzustände, welche aus coupled-channel Rechnungen gewonnen wurden. Das Profil der Resonanzen, insbesondere die Breite der gemessenen Spektren, zeigt eine gute Übereinstimmung mit theoretischen Vorhersagen. Auch bei hoher spektroskopischer Intensität reproduzieren die Messungen die simulierten Linienformen. Weiterhin wurde auch der durch den Photoassoziationslaser induzierte light shift gemessen, welcher ebenfalls von den theoretischen Vorhersagen abweicht.

Im Verlauf der Arbeit wurde die numerische Simulation durch Berücksichtigung zusätzlicher Einflüsse, wie des exakten Verlaufes der Franck-Condon Dichte und der Energieabhängigkeit des light shifts des Spektroskopielasers, weiter verbessert. Außerdem wurde die Modellierung der experimentellen Gegebenheiten, insbesondere des Volumens der optischen Falle und damit der Dichte des atomaren Ensembles verbessert und der Einfluss unterschiedlicher Fallentiefen und Photoassoziationsdauern untersucht. Durch eine Modifikation des Kopplungsparameters und der natürlichen Zerfallsbreite konnten zwar die absoluten Assoziationsraten der Messung reproduziert werden, wobei allerdings im Falle von hohen Intensitäten die Linienform nicht mehr mit dem experimentellen Ergebnis übereinstimmt. Zum Abschluss wird ein verbesserter experimenteller Aufbau vorgeschlagen, bei dem Verbreiterungsmechanismen durch Verwendung eines optischen Gitters unterdrückt werden und dadurch die Analyse der Messergebnisse wesentlich vereinfacht wird.



# Abstract

In this thesis I present the results of photoassociation measurements in ensembles of atomic calcium over an intensity range of below  $1 \text{ W/cm}^2$  up to  $600 \text{ W/cm}^2$ . The temperature of the atoms was reduced to  $1 \mu\text{K}$  by laser and evaporative cooling. Afterwards the two most-weakly bound states in the excited molecular potentials that dissociate to the asymptote  $^3P_1+^1S_0$  have been investigated regarding the shape and absolute rate of the resonances. The investigation showed that the measured rates differ by more than an order of magnitude compared to theoretical calculations. The predictions are based on a scattering formalism by Bohn & Julienne and wave functions derived from coupled-channel calculations. The shape of the resonances, the width in particular, agrees well with the numerical calculations. Especially the power broadening at high intensity is reproduced by the experiment. Further the light shift introduced by the photoassociation laser has been measured which also differs from the predictions.

In the further course of the thesis the numerical simulations were improved by considering additional influences like the exact dependence of the Franck-Condon density and the light shift of the photoassociation laser as a function of the collision energy. Additionally the modeling of the experimental setup with a special emphasis on the volume of the optical trap and thus the density of the atomic ensemble was improved and the influence of varying trap depth and photoassociation duration has been studied. Investigating possible explanations for the discrepancy of the measured rates compared to theory, I show that by a modification of the coupling parameter and the spontaneous decay rate of the molecular state the rates measured in the experiment can be reproduced theoretically, with the restriction that at high intensity the calculated line shape no longer agrees with the measurement. In the last chapter an improved experimental apparatus is presented that by using an optical lattice suppresses thermal broadening and thus simplifies the analysis substantially.

IV

**Schlüsselworte:** Molekülphysik, optische Spektroskopie, Photoassoziation, ultrakalte Atome, spektrale Linienformen

**Keywords:** molecular physics, optical spectroscopy, photoassociation, ultracold atoms, spectral lineshapes

# Contents

<b>1</b>	<b>Introduction</b>	<b>1</b>
<b>2</b>	<b>Theoretical description</b>	<b>5</b>
2.1	Atomic properties of calcium . . . . .	5
2.2	Molecular Potentials . . . . .	6
2.3	Cold atomic collisions . . . . .	7
2.3.1	Franck-Condon densities . . . . .	10
2.4	Photoassociation lineshape . . . . .	11
2.5	Molecular saturation at high intensities . . . . .	14
<b>3</b>	<b>Experimental apparatus</b>	<b>15</b>
3.1	Preparation of cold atomic samples . . . . .	15
3.1.1	Singlet transition MOT . . . . .	17
3.1.2	Intercombination transition MOT . . . . .	18
3.1.3	Evaporative cooling in an optical dipole trap . . . . .	20
3.1.4	Temperature of the atomic sample . . . . .	26
3.2	Spectroscopy laser setup . . . . .	26
3.2.1	Phase locking technique . . . . .	27
3.2.2	Effective photoassociation intensity . . . . .	29
3.3	Experiment control . . . . .	30
<b>4</b>	<b>Photoassociation: From low to high power</b>	<b>33</b>
4.1	Low intensity spectra . . . . .	36
4.2	High intensity spectra . . . . .	39
4.3	Comparison of photoassociation rates: Experiment vs simulation . . . . .	40
4.4	Investigation of intensity-induced line broadening . . . . .	45
4.5	Light shift: Experiment vs theory . . . . .	46

<b>5</b>	<b>Discussion of previously unconsidered effects</b>	<b>51</b>
5.1	Collision-energy dependent Franck-Condon density . . . . .	51
5.2	Influence of atom recapture by the dipole trap . . . . .	54
5.3	Alignment of spectroscopy beam . . . . .	58
5.4	Energy dependence of the PA light shift . . . . .	60
5.5	Influence of the duration photoassociation illumination . . . . .	62
5.6	Extension of the atomic cloud . . . . .	63
5.7	Effect of misaligned dipole trap beams . . . . .	67
<b>6</b>	<b>Adjustment of the theoretical parameters</b>	<b>71</b>
6.1	Adjustment of the Franck-Condon density . . . . .	71
6.2	Additional non radiative decay channels . . . . .	72
<b>7</b>	<b>Summary</b>	<b>79</b>
<b>8</b>	<b>Outlook</b>	<b>83</b>
8.1	Optical lattice . . . . .	83
	<b>Appendices</b>	<b>87</b>



# Chapter 1

## Introduction

During recent years the interest in redefining the second in the international system of units (SI) by means of an optical atomic clock has been a driving force for the development of experimental techniques involving precision experiments in the field of ultracold physics. In order to replace the current primary frequency standard defined in 1967 and based on a transition between two hyperfine ground states of  $^{133}\text{Cs}$  [Ess55, Ger10] a variety of different approaches have been explored. Among those are high precision measurements of optical transitions between electronic and hyperfine states in single ions confined in radio frequency fields [Hun16, Hun14] as well as in ensembles of neutral atoms cooled to micro-kelvin temperatures within optical and magnetic traps [Met99, Fal14, Nic15b]. Compared to the current definition based on a transition in the microwave regime the new experiments rely on transitions in the optical frequency range. Due to the extremely high precision of the involved measurements similar experimental techniques have a variety of other applications including atom interferometry [Müt13], tests of fundamental physics like a time variation of the fine structure constant [Pei04, Rob19], the determination of the electron-to-proton mass ratio [She08, McG15] and the determination of the electric-dipole-moment of polar molecules [Chi01]. While initially most experiments were performed on cold and dense samples of group-I atoms like rubidium [Mil94], with improved experimental techniques cold ensembles of group-II atoms became accessible. These atoms, sometimes referred to as physicist atoms, further sparked the interest of scientist around the world because of their special atomic structure. With their completely filled outermost electronic s-shell they possess distinct optical properties featuring a broad singlet transition that is perfectly suited for cooling while the very narrow triplet transition allows high accuracy for spectroscopic measurements. Among the alkaline-earth elements strontium is one of the most promising candidates for a redefinition of the second [Kat02, Leg08]. Since the group-II atoms have become the basis of a wide range of applications it is

important to understand how they interact with each other in detail. This is the reason why many scientific studies investigate the properties of such elements to verify e.g. their scattering behavior [Yan13, Zel06] to explore ways to improve future experiments and to reduce uncertainties of existing measurements.

The association of two atoms to bound molecular states with large internuclear distances by resonant laser light is a widely used spectroscopic technique for the investigation of atomic interactions between group-II particles and atoms in general. The precise binding energies of excited weakly bound molecular states have been measured by photoassociation spectroscopy for strontium [Zel06, McG15], ytterbium [Eno07, Kit08] and calcium [Vog07, Kah14b, Pac17]. The transition frequency of these photoassociation resonances strongly depends on the long range part of the internuclear interaction potentials. Combining the binding energies of those weakly bound states with measurements of the deeply bound states from molecular spectroscopy [All04, All05] the excited state potentials have been determined using coupled channel calculations. In the same way two-photon transitions have been used to also determine the binding energies of molecular ground states and subsequently the ground state interaction potential was derived for the different alkaline-earth elements [Pac17, Zel06].

Compared to the other alkaline-earth elements calcium features one of the most narrow triplet transitions ( $\gamma = 374$  Hz [Deg05]) while the experimental techniques required for cooling are readily available. Also, the ground state scattering length is known with great precision which makes  $^{40}\text{Ca}$  an ideal testbed for investigation of both how the atoms interact with each other and also for e.g. improved cooling techniques. A prominent example of such techniques are Feshbach resonances that have widely been used to tune the interaction of atoms to e.g. improve evaporative cooling of group-I atom based experiments or to create dense samples of cold molecules [Köh06]. These experiments required that the involved atoms possess a magnetic moment in their atomic ground state and are consequently not suited for bosonic isotopes of calcium or strontium featuring a singlet ground state. In this case, a similar effect can be achieved employing optical Feshbach resonances (OFR) instead that use resonant light to couple molecular bound states to the atomic scattering continuum [Nic15a]. Due to the limited lifetime of the excited molecular states OFRs are accompanied by atomic losses. They are related to photoassociation of atom pairs that are subsequently lost from the sample due to decay of the produced molecules and reduce the density of the investigated ensembles.

The photoassociation losses were theoretically described by a scattering formalism de-

veloped by Bohn and Julienne [Boh96, Boh99] that also predicts the shape of the molecular resonances broadened by the residual kinetic energy of the ultracold atoms and the laser interaction [Nap94, Ciu04]. Special interest lies in the behavior towards higher intensities as one of the proposed solutions to reduce unintentional OFR losses is to use high intensities at large detunings from the resonances. Only for group-I elements there are systematic investigations [Sim02] in this regard while there are no studies in the case of group-II atoms.

This thesis focuses on three main questions:

- a quantitative analysis of the photoassociation rate of  $^{40}\text{Ca}$  at different light intensities
- classification of a high and low intensity regime analogous to saturation in atomic transitions
- the validity of the theoretical formalism with a special focus on high intensities by comparison to numerical simulation of the photoassociation resonances.

I will first introduce the atomic and molecular properties of the bosonic  $^{40}\text{Ca}$  and give a short overview of the theoretical description of the photoassociation process. A formula that serves as the basis of the numerical calculation of the shape and rates of the investigated photoassociation resonances will be given with a special emphasis on the broadening mechanisms introduced through the thermal energy distribution of the atomic sample as well as the intensity of the spectroscopy laser towards higher intensities. Further, the concept of saturation of the photoassociation process is discussed. In chapter 3, I will detail the experimental setup for the creation of dense atomic samples of calcium that rely on sequential cooling in a magneto-optical trap operating at the singlet and triplet transitions of calcium combined with an optical dipole trap. The photoassociation resonances that will be presented are only a few 10 kHz wide, requiring a highly frequency stable spectroscopy light source and a sophisticated mechanism to finely tune its frequency. For this the mechanical stability of a reference Fabry-Perot cavity is transferred to the spectroscopy laser using the Pound-Drever-Hall locking technique [Dre83]. The photoassociation resonances of the two most-weakly bound states in the molecular potentials that dissociate to the  $^3P_1+^1S_0$  asymptote were measured and linewidth and molecule formation rate over a range of 3 decades from below  $1\text{ Wcm}^{-2}$  up to  $600\text{ Wcm}^{-2}$  are deduced from the measurement. The results are then compared to theoretical expectations based on the well-known interatomic potentials.

The influence of both the modeling of the experimental parameters such as the size of the optical trap or the local spectroscopic intensity and theoretical approximations are quantified. Finally, I will present how the experiment could be extended by an optical lattice setup and shortly describe how with this setup the measurement of both the binding energy of the molecular states and the determination of the rate i.e. the coupling between the scattering continuum and bound states can be improved in the future.

## Chapter 2

### Theoretical description

This thesis investigates atomic collisions of calcium at very low temperatures, i.e. low kinetic energies of the involved particles and compares the experimental findings to the established theoretical formalism. Compared to other group II elements that are routinely used in various precision experiments, e.g. the attempt to define a new primary frequency standard, calcium offers some advantages that make it an ideal candidate for a study of the interaction of cold atomic samples with light. It can readily be cooled to ultra-low temperatures [Bin01, Kra09, App13] using laser light in the visible spectrum that can be generated by diode and solid-state lasers at sufficient power under laboratory conditions. Additionally, compared to other elements with the same electronic structure it features a comparatively narrow nearly spin-forbidden intercombination transition  $^1S_0$ - $^3P_1$  with a linewidth of less than a kHz that enables spectroscopic measurements with great accuracy. The narrow line is only surpassed by magnesium and beryllium for which the cooling procedure is more complicated due to the wavelength of the involved lasers. For example, in the case of magnesium the cooling is much more complicated since some of the required cooling light is in the UV range [Kul12]. Furthermore in calcium the relevant molecular potentials are precisely known from a series of measurements of molecular binding energies by molecular spectroscopy [All03, All05] and photoassociation spectroscopy [Vog07, Kah14b, Pac17]. This chapter will introduce the known atomic and molecular parameters that are required to evaluate the measurements that will be presented later in the thesis as well as the underlying theoretical formalism to describe the results.

#### 2.1 Atomic properties of calcium

In the presented study I have analyzed photoassociation spectra of the bosonic calcium isotope  $^{40}\text{Ca}$ . Calcium is a group II element meaning that in its electronic ground

state the outermost  $s$ -shell is completely filled with two electrons which means that in its electronic ground state there is no magnetic moment. The calcium isotope  $^{40}\text{Ca}$  does not possess a nuclear spin which simplifies the electronic structure immensely since there is no hyperfine splitting present in both the atomic and the molecular spectra that are the topic of this thesis. Due to its two valence electrons calcium features a distinct electronic structure with a broad singlet transition from its  $^1S_0$  ground state to the  $^1P_0$  excited state at 423 nm and a strongly spin forbidden triplet transition to the states  $^3P_j$ ,  $j = 0, 1, 2$  at  $\approx 657$  nm. This electronic structure allows efficient cooling down to sub micro-Kelvin temperatures while maintaining high sample densities. At the same time it provides a narrow line for highly accurate spectroscopic measurements. The cooling process is efficient enough that in the past it was possible to achieve Bose-Einstein condensation [Kra09, App13] for calcium with moderate final evaporative cooling. The natural linewidth of the  $^1S_0$ - $^3P_1$  transition  $\gamma_{\text{atom}} = 374(9)$  Hz is smaller by a factor of  $\approx 20$  when compared to strontium [Boy07].

In the low energy limit, as is the case for ultracold atomic samples, the interaction reduces to  $s$ -wave scattering (angular momentum of the scattering state  $l = 0$ ). The interaction can then be described by a single parameter the so-called  $s$ -wave scattering length that is directly related to the molecular potentials described in the next section. For  $^{40}\text{Ca}$  the  $s$ -wave the scattering length was measured to  $a = 308.5(50)a_0$  in units of the Bohr radius  $a_0$  [Pac17].

## 2.2 Molecular Potentials

In the Born-Oppenheimer approximation [Bor27] the potential energy between two atoms separated by  $R$  is given by  $V(R)$ . This includes both the interaction of the nuclei as well as of the electrons. The long-range part of this interaction potential is usually given by an inverse power sum of the form

$$V(R) = \sum \frac{C_n}{R^n}. \quad (2.1)$$

where the coefficients  $C_n$  for each individual potential are closely related to the radiative properties of the atoms [Wei03]. Figure 2.1 shows the potentials that govern interaction between the colliding atoms in the ground and in different excited states. The results that will be discussed mostly depend on the interaction between two ground state  $^1S_0$  atoms giving the molecular state  $X^1\Sigma_g^+$  that determines the scattering state of the

colliding atoms. The two potentials that involve one atom in the ground state and the other in the excited triplet state  $^3P_1$  are labeled  $a\ ^3\Sigma_u^+$  and  $c\ ^3\Pi_u$  (see Fig. 2.1 for details) in Hund's notation [Her50] case (a). Both dissociate to the asymptote with angular momentum  $J = 1$ . For the most weakly bound states that have been studied in this work they are more accurately described as a mixture of the two case (a) potentials. They are best described by Hund's case (c) potentials  $(a, c)1_u$  and  $c0_u^+$ . This notation will be used throughout this work referring to the projection of the coupled spin and orbit angular momentum on the molecular axis  $\Omega = 0, 1$ .

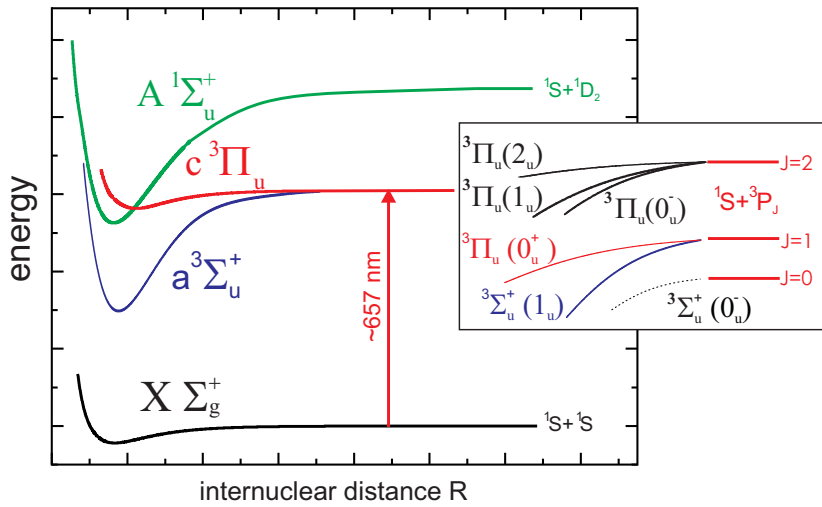


Figure 2.1: Excerpt of the molecular potential scheme of  $^{40}\text{Ca}$  showing the relevant potentials dissociating to the  $^1S_0 + ^1S_0$  and  $^3P_1 + ^1S_0$  atomic asymptotes.

The excited potentials have been modeled by measuring the binding energy of the most weakly bound molecular states using photoassociation spectroscopy [Kah14b] and combining them with spectroscopic measurements of deeply bound states [All05]. Similar measurements using two color photoassociation spectroscopy have been used to probe the ground state potential  $X\ ^1\Sigma_g^+$  and from the measurement of the four most-weakly bound states both the long range interaction parameters and the scattering length of calcium have been determined [Pac17]. The detailed description of the molecular potentials enabled the comparison of the experimentally measured spectra to theoretical predictions that will be the topic of this thesis.

## 2.3 Cold atomic collisions

A theory that describes the interaction of cold atoms in the presence of a radiation field has been developed by Bohn and Julienne [Boh96, Boh99, Nic15a]. This theoretical

formalism is the foundation of the presented work and shall be introduced in this section. When two ground state  $^{40}\text{Ca}$  atoms with relative kinetic energy  $\epsilon_{\text{col}}$  approach each other their collision properties will be governed by their ground state interaction potential  $X^1\Sigma_g^+$ . In the presence of a light field with angular frequency  $\omega$  tuned closely to a bound state in an excited molecular potential the atom pair can be photoassociated to a weakly bound excited molecule with binding energy  $E_b$  relative to the atomic asymptote. In the case of the investigated  $^{40}\text{Ca}$  the measurements were focused on transitions to potentials dissociating to atoms in the  $^3P_1+^1S_0$  states introduced in the last section.

This process is referred to as photoassociation and in general it is not limited to the interaction with a single laser but instead multiple laser frequencies  $\omega_1, \omega_2 \dots$  can result in a coupling between multiple molecular states. In this work, I will focus on the description of the process with only a single photon per atom collision referred to as one color photoassociation.

The frequency of the light field coupling the bound and scattering state is detuned by  $\Delta = E_b - \hbar\omega$  with respect to the binding energy of the molecular state that is studied. The coupling can be described by a time-dependent interaction  $-\mathbf{d}(R) \cdot \mathbf{E}(t) = V_{\text{opt}}^{(i)} \cos(\omega_i t)$  where the constant optical potential  $V_{\text{opt}}^{(i)}$  is the amplitude of the harmonic perturbation,  $\mathbf{d}(R)$  is the molecular transition dipole operator and  $\mathbf{E}(t) = \mathbf{E} \cos(\omega t)$  is the electric field vector of the coupling field with amplitude  $|\mathbf{E}| = \sqrt{2I/\epsilon_0 c}$  derived from the intensity of the light  $I$ . According to Fermi's golden rule the transition rate between an energy normalized continuum state  $|\phi_{\text{scat}}\rangle$  and the molecular bound state  $|\Phi\rangle$  is given by the stimulated rate [Pac17]

$$\Gamma_{\text{stim}} = \frac{\pi}{2\hbar} \left| \langle \Phi | V_{\text{opt}}^{(1)} | \phi_{\text{scat}} \rangle \right|^2. \quad (2.2)$$

Generally it is assumed that  $\mathbf{d}(R)$  is only weakly depending on the distance between the nuclei at long range, which is the case for the weakly bound states studied in this thesis. For these molecules one assumes that the decay rate of the molecular state becomes twice the atomic decay rate  $\gamma_{\text{atom}}$  and the stimulated rate can be expressed as [Ciu06]

$$\Gamma_{\text{stim}} = \gamma_{\text{atom}} \frac{3I\lambda^3}{2^3 c \pi} f_{\text{ROT}} f_{\text{FCD}}. \quad (2.3)$$

In this equation  $f_{\text{ROT}}$  contains this factor of two between molecular and atomic decay rate as well as the polarization dependence and the Hönl-London factor for the



respective transition. The overlap integral  $f_{\text{FCD}} = |\langle \Phi | \phi_{\text{scat}} \rangle_{\text{rad}}|^2$  is usually referred to as the Franck-Condon density or the free-bound Franck-Condon factor [Boh99] where the subscript indicates that only the radial component of the wavefunction is taken into account. Furthermore  $\lambda = 657$  nm is the wavelength of the intercombination transition. Bohn and Julienne [Boh96, Boh99] apply a scattering formalism with the incident channel is the ground state potential  $V_0 = X^1\Sigma_g^+$  and a single excited state  $\phi$  that depends on the excited molecular potential in question. In the case studied here the involved channels are  $0_u^+$  ( $c^3\Pi_u$ ) and  $1_u$  ( $a^3\Sigma_u^+ c^3\Pi_u$ ). Additionally they introduce an artificial channel that addresses the natural decay of the excited molecular state by a single parameter  $\gamma_1$  that as described before is initially assumed to be  $2\gamma_{\text{atom}}$ . The probability that a collision of single atom pair leads to the creation of a molecule is proportional to the scattering matrix element:

$$|S_{\text{inel}}|^2 = \frac{\gamma_1 \Gamma_{\text{stim}}}{\frac{1}{\hbar^2} [\epsilon_{\text{col}} - (\Delta + E_{\text{ls}})]^2 + \left(\frac{\gamma_1 + \Gamma_{\text{stim}}}{2}\right)^2}. \quad (2.4)$$

Here  $E_{\text{ls}}$  is the light shift induced by the photoassociation laser that can in general be calculated by evaluating a *second order Franck-Condon factor* that again involves the scattering and bound state wave functions

$$E_{\text{ls}} = -\frac{\pi}{2} (V_{\text{opt}}^{(1)})^2 \int_0^\infty dR \phi_b(R) g_0(R) \int_0^R dR' f_0(R') \phi_b(R') \quad (2.5)$$

where the incident-channel wavefunction and its irregular counterpart are represented by  $f_0, g_0$ , respectively [Boh99].

The rate at which two atoms are associated to a bound molecule is given by

$$K = \frac{\hbar\pi}{\mu k_r} |S_{\text{inel}}|^2, \quad (2.6)$$

where  $k_r = \sqrt{2\mu\epsilon_{\text{col}}}/\hbar$  is the relative wave vector of the colliding atom pair and  $\mu$  is their reduced mass.

A photoassociation line belonging to an individual pair of atoms is Lorentzian as a function of the detuning  $\Delta$  as can be seen from Eq. 2.4. Since the measurements were performed on ensembles of cold atoms that follow a thermal velocity distribution the initial collision energy  $\epsilon_{\text{col}}$  will generally vary which leads to a different stimulated rate  $\Gamma_{\text{stim}}$  and a shift of the resonance condition. Also the center of mass of a colliding atom pair will have a velocity component in the direction of the photoassociation laser

introducing a Doppler shift to the measurement. The influence of these effects on the final measurement will be described separately later in this chapter due to their importance during the analysis of the measured spectra.

### 2.3.1 Franck-Condon densities

The Franck-Condon densities denoted as  $|\langle \Phi | \phi_{\text{scat}} \rangle_{\text{rad}}|^2$  that have been used to evaluate the stimulated rate in Eq. 2.2 were calculated using a coupled channel formalism based on the experimentally determined excited  $(a, c)1_u$ ,  $c0_u^+$  and ground state potentials  $X^1\Sigma_g^+$ . The Franck-Condon densities for transitions to the six most-weakly bound states in the two excited potentials are shown in Fig.2.2 as a function of the collision energy of the atom pair. These values also include the rotational factor that depends on the angular momentum of the respective transition and assumes a linear polarization of the spectroscopy light.

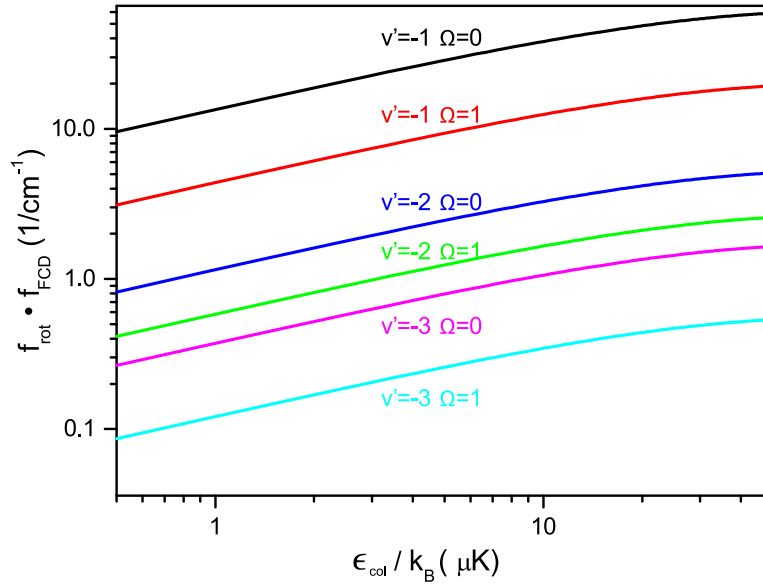


Figure 2.2:  $f_{\text{ROT}} \cdot f_{\text{FCD}}(\epsilon_{\text{col}})$  for s-wave scattering ( $l = 0$ ) calculated for a transition from a scattering state with  $J = 0$  to an excited state with  $J = 1$  in the potential  $^1S_0$ - $^3P_1$  using a coupled channel model. The values belonging to the six most-weakly bound excited states labeled by their vibrational quantum number  $v'$  are presented here. Courtesy of E. Tiemann.

The respective bound states are represented by a multicomponent wave function that is represented by a combination of basis vectors  $|^1S_0 + ^3P_j, l, J\rangle$  in the Hund's case (e) basis. In this description the first part in the basis vector describes the atomic asymptote the molecule with atomic angular momentum  $j$  dissociates to, while  $l$  stands

for the angular momentum of rotation of the atom pair and  $J$  denotes the total angular momentum of the molecule. For the excited states only  $J = 1$  and negative parity are relevant leaving us with a total of three basis states:

$$|{}^1S_0 + {}^3P_1, 0, 1\rangle, \quad (2.7)$$

$$|{}^1S_0 + {}^3P_1, 2, 1\rangle, \quad (2.8)$$

$$\text{and } |{}^1S_0 + {}^3P_2, 2, 1\rangle. \quad (2.9)$$

Due to the electric dipole selection rule  $\Delta l = 0$  only the component  $|{}^1S_0 + {}^3P_1, 0, 1\rangle$  contributes to the overlap with the continuum represented by  $|{}^1S_0 + {}^1S_0, 0, 0\rangle$ . At the low temperatures used in the experiment it is sufficient to only consider s-wave scattering states for the calculation of the Franck-Condon densities corresponding to an angular momentum of  $J = 0$  and positive parity. Both components given in Eq. 2.7 and 2.8 are relevant when evaluating the bound-bound transition probability that is given by Franck-Condon factors [Pac17].

## 2.4 Photoassociation lineshape

In order to calculate the lineshape that is measured in an experiment I have to average Eq. 2.4 over an ensemble of  ${}^{40}\text{Ca}$  atoms that follow a thermal velocity distribution at temperatures in the low microkelvin regime. This introduces several effects that lead to a broadening of the initially Lorentzian shape:

- The Franck-Condon density for a transition from a two-atom scattering state to a bound molecular state strongly depends on the collision energy  $\epsilon_{\text{col}}$  leading to different stimulated rates  $\Gamma_{\text{stim}}(\epsilon_{\text{col}})$ .
- The initial collision energy  $\epsilon_{\text{col}}$  directly influences the resonance condition in the denominator of Eq. 2.4 and has to be considered by averaging over the thermal distribution of the atomic ensemble.
- The resonance condition is further altered by the center-of-mass motion of each individual colliding atom pair introducing a Doppler shift that has to be addressed when evaluating the lineshape.

To account for the dependence of the Franck-Condon density on the energy of the scattering states the stimulated rate was evaluated assuming the validity of the Wigner threshold law [Wig48]. It states that at sufficiently low energy, i.e. at microkelvin temperatures like in the experiment, for s-wave scattering the overlap between the bound and scattering wavefunction and thus the Franck-Condon density is proportional to  $k_r$ . A common approach when introducing this behavior is to define an energy-independent optical length  $l_{\text{opt}}$  as a function of the photoassociation intensity:

$$l_{\text{opt}}(I) = \frac{\Gamma_{\text{stim}}}{2k_r\gamma_1} = \frac{3\lambda^3}{16\pi c} \frac{|\langle \Phi | \phi_{\text{scat}} \rangle|^2}{k_r} I. \quad (2.10)$$

The introduction of this optical length considers the dependency of the stimulated rate of the Franck-Condon density in Eq. 2.3 and substantially simplifies the generation of simulated spectra that can be compared to experimental results.

The momenta of the atoms in the dipole trap were modeled by two Boltzmann-distributions for the center-of-mass and relative motion  $f_M(\mathbf{p}_c)$  and  $f_\mu(\mathbf{p}_r)$ , respectively

$$f_M(\mathbf{p}_c) = (\sqrt{\pi}p_M)^{-3} \exp\left(-\frac{\mathbf{p}_c^2}{p_M^2}\right) \text{ and} \quad (2.11)$$

$$f_\mu(\mathbf{p}_r) = (\sqrt{\pi}p_\mu)^{-3} \exp\left(-\frac{\mathbf{p}_r^2}{p_\mu^2}\right), \quad (2.12)$$

that depend on the temperature of the sample  $T$ , the most probable momenta  $p_M = \sqrt{2k_B T 2m_{Ca}}$ ,  $p_\mu = \sqrt{k_B T m_{Ca}}$  and impulses  $\mathbf{p}_c$ ,  $\mathbf{p}_r$  of the center-of-mass and the relative motion of the atomic pair, respectively. To obtain the thermally broadened lineshape the inelastic loss coefficient given in Eq. 2.6 has to be thermally averaged [Ciu04]

$$\langle K(\Delta) \rangle = \int d^3p_c f_M(\mathbf{p}_c) \int d^3p_r f_\mu(\mathbf{p}_r) K\left(\Delta - \frac{\mathbf{p}_c \cdot \mathbf{k}_{\text{las}}}{2m_{Ca}}, \mathbf{p}_r\right). \quad (2.13)$$

This expression was simplified by the introduction of two dimensionless quantities  $y = -\mathbf{k}_{\text{las}} \cdot \mathbf{p}_c / (k_{\text{las}} p_M)$  and  $x = |\mathbf{p}_r| / p_\mu$  that reduces the six dimensional integral to a two dimensional one instead

$$\langle K(\Delta) \rangle = \frac{2k_B T}{hQ_T \sqrt{\pi}} \times \int_{-\infty}^{\infty} dy \exp(-y^2) \int_0^{\infty} dx x \exp(-x^2) |S(\Delta, y, x^2)|^2, \quad (2.14)$$

where  $Q_T = \left(\frac{2\pi\mu k_B T}{h^2}\right)^{3/2}$  denotes the partition function for free particles.

The experimental signature measured in photoassociation experiments is the loss of atoms from the sample. The loss of atoms depends on the coefficient  $\langle K(\Delta) \rangle$  and the local atomic density inside the dipole trap  $\rho$  according to

$$\dot{\rho} = -2 \langle K(\Delta) \rangle \rho^2. \quad (2.15)$$

I assumed that every photoassociation event leads to the loss of two atoms and that one-body losses due to the limited lifetime of the atoms in the dipole trap are negligible compared to the losses induced by the laser radiation since the lifetime of the trap ( $\approx 56$ s) is long compared to the photoassociation duration ( $\tau_{\text{PA}} < 100$ ms) [Kah14b]. The parameter that is accessible in the experiment is the total number of atoms remaining after a set photoassociation time  $\tau_{\text{PA}}$ . Thus, to calculate the theoretical lineshapes I integrated Eq. 2.15 assuming that the thermal nature of the distribution of atoms in the trap is not altered by the increased losses in the center of the trap relative to the edges i.e. the density distribution remains Gaussian over the course of a measurement. The corresponding differential equation regarding the number of atoms rather than the local density is then given by

$$\dot{N} = -\beta N^2 \quad (2.16)$$

where the atomic loss factor  $\beta$  is

$$\beta = \frac{1}{\sqrt{2}V_{\text{DT}}} \langle K(\Delta) \rangle. \quad (2.17)$$

In this equation

$$V_{\text{DT}} = \frac{1}{\omega_1\omega_2\omega_3} \left(\frac{2\pi k_B T}{m_{\text{Ca}}}\right)^{3/2} \quad (2.18)$$

is the effective volume of the dipole trap with the harmonic trapping frequencies  $\omega_i$  that will be derived from the atom trap parameters in the next chapter.

The solution to this differential equation is given by

$$N(\tau_{\text{PA}}, \Delta) = \frac{N_0}{1 + \beta\tau_{\text{PA}}N_0}, \quad (2.19)$$

which allows the calculation of photoassociation spectra from experimental parameters that are to be compared to the experimental measurements in the following sections.

A more detailed description of the conversion from local density to total number of trapped atoms is given in Appendix A after Section 8.1.

## 2.5 Molecular saturation at high intensities

An important part of this work focuses on the saturation of the photoassociation transition and as such it is important to know at which intensity the transition is considered saturated. The regions of *high* and *low* intensity will be used throughout the description of the experimental results. An atomic transition is starting to show signs of saturation when the natural linewidth of the transition  $\gamma_{\text{atom}}$  is equal to the linewidth induced by the coupling to a resonant light field. The intensity at which saturation occurs for the atomic triplet  $^1S_0\text{-}^3P_1$  transition can be calculated by [Met99],

$$I_{\text{sat}} = \frac{\pi \hbar c \gamma_{\text{atom}}}{3\lambda^3} = 1.724 \cdot 10^{-7} \text{ Wcm}^{-2}. \quad (2.20)$$

I have used a similar approach to determine the molecular saturation intensity relevant for the photoassociation process. From Eq. 2.3 one can determine when the stimulated starts to become a substantial influence on the width of the resonance i.e. when  $\Gamma_{\text{stim}} = \gamma_{\text{mol}} = 2\gamma_{\text{atom}}$ . Consequently signs of saturation should start to become visible in the measured spectra at intensities greater than

$$I_{\text{sat,PA}} = \frac{16\pi c}{3\lambda^3 |\langle \Phi | \phi_{\text{scat}} \rangle|^2}. \quad (2.21)$$

The same approach has been used in the description of photoassociation spectra of group I atoms [Sim02].

# Chapter 3

## Experimental apparatus

In order to suppress a wide range of effects detrimental to high precision spectroscopy the atoms investigated in this thesis have been cooled to low micro-Kelvin temperatures. The experimental scheme is generally the same as during earlier measurements of the binding energy of the molecular states [Kah14b, Pac17] and can be separated into three stages. Firstly, calcium is evaporated inside an electrically heated oven and decelerated in a Zeeman slower. Subsequently a part of the slowed atoms is further cooled by means of a two-stage magneto optical trap (MOT) [Met99]. In the last step, the atoms are transferred to a crossed optical dipole trap where the atoms with the highest kinetic energy are removed by evaporative cooling. After the atomic sample is prepared the atoms are probed with a spectroscopy laser that can be adjusted in a wide frequency and intensity range. In the last step the number of atoms in the optical dipole trap is determined from the optical density of the atomic sample measured by absorption imaging of the atomic cloud. The individual stages of preparation of low energy  $^{40}\text{Ca}$  atoms, interaction with spectroscopy light and subsequent measurement of the atom number will be described in detail in the following sections.

### 3.1 Preparation of cold atomic samples

The experiment is performed inside an ultra-high vacuum chamber (see Fig. 3.1) at a pressure of  $2 \cdot 10^{-10}$  mbar. Metallic calcium is evaporated in an electrically heated oven at temperatures between 570 and 600 °C. The beam of hot atoms is decelerated in a 38 cm long Zeeman slower connecting the oven to the main vacuum chamber [Naz07] using light at a wavelength of 423 nm corresponding to the broad singlet transition  $^1S_0 - ^1P_1$ . After exiting the slowing region the atoms are deflected from their original beam path by an optical molasses to allow continuous loading of the MOT without perturbation by the high velocity particles in the hot atom beam. Subsequently, they are further

cooled by two consecutive MOT stages operating on the broad singlet transition  $^1S_0$ - $^1P_1$  and the narrow intercombination transition  $^1S_0$ - $^3P_1$  of calcium at wavelengths of 423 nm and 657 nm, respectively. In the final step of the cooling cycle part of the pre-cooled the atomic sample is transferred to an optical dipole trap operating at a frequency of 1030 nm and its temperature is further reduced by means of evaporative cooling where the trap depth is lowered adiabatically. Inside the vacuum chamber a pair of coils in Helmholtz configuration generate the magnetic field gradient required for the individual MOT phases. The same coils are used during the measurement to impose a bias field of  $B = 0.285(7)$  mT that defines a quantization axis for e.g. the polarization of the spectroscopy laser [Naz07]. A schematic drawing of the vacuum chamber and the involved laser beams is shown in Fig. 3.1.

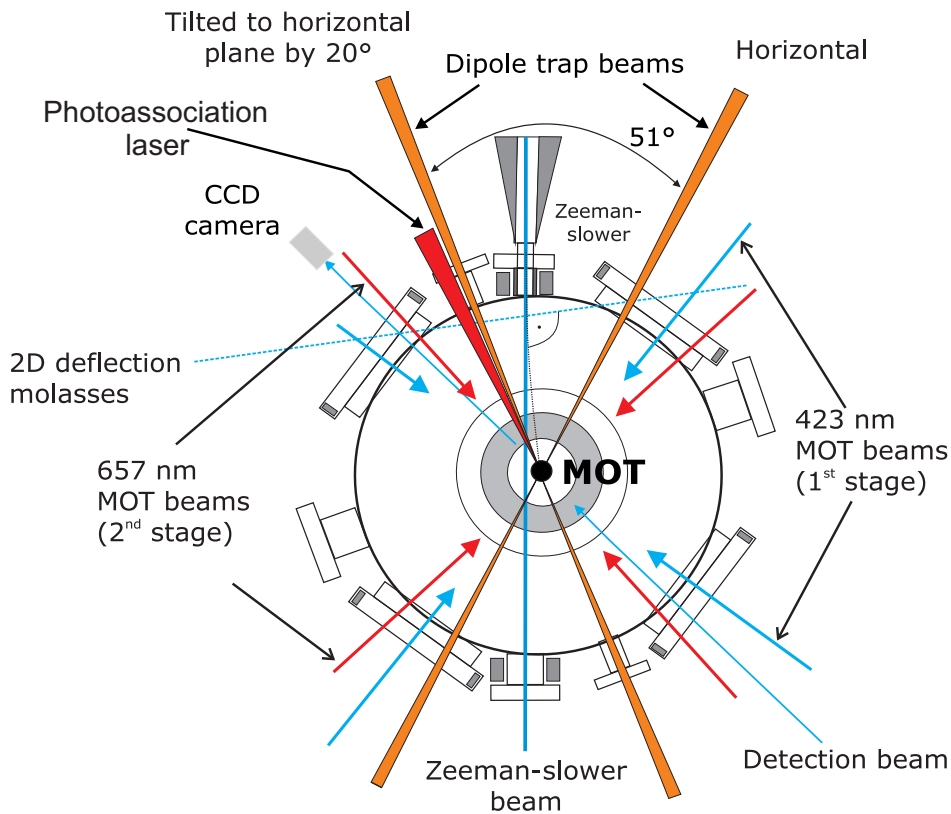


Figure 3.1: Schematic drawing of the experimental chamber and the beam path of the involved cooling and spectroscopy beams. The blue arrows indicate laser beams close to the singlet transition frequency of 423 nm, the red arrows represent beams tuned closely to the triplet transition frequency of 657 nm while dipole trap beams operating at 1030 nm are shown in orange.



### 3.1.1 Singlet transition MOT

After the initial cooling the calcium atoms exit the Zeeman slower with an average velocity of  $\approx 40 \text{ ms}^{-1}$  and accumulate inside a MOT that uses light resonant to the atomic singlet transition  $^1S_0 - ^1P_1$  i.e. at a wavelength of 423 nm (see Fig. 3.2 for a detailed energy level diagram). The MOT is formed by three pairs of counter-propagating beams where each beam can be adjusted individually regarding its direction, intensity and polarization. From the excited state  $4s4p \ ^1P_1$  the atoms only partially decay directly back to the ground state. With a probability of  $\approx 10^{-5}$  atoms instead decay to the metastable  $4s3d \ ^1D_2$  state [Bev89, Lel87]. By application of a second light source, the so-called repumper, operating at a wavelength of 672 nm, atoms in the metastable state are pumped to the  $4s5p \ ^1P_1$  state instead from where they almost immediately decay back to the ground state due to the short lifetime of the state. In the ground state the atoms can then again interact with the cooling light to further reduce the sample temperature. This repumping scheme considerably reduces the time it takes to create cold samples in the experiment. The atoms are typically cooled for 1 second in this stage which results in a final number of atoms of  $\approx 3 \cdot 10^8$  at a temperature of  $\approx 4 \text{ mK}$  inside the MOT.

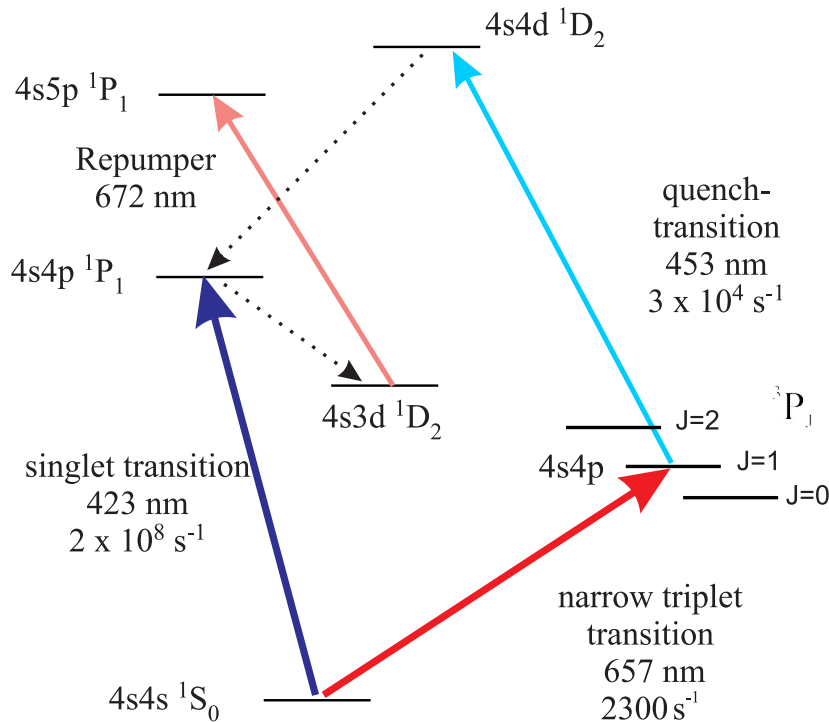


Figure 3.2: Reduced energy level diagram of calcium showing the transition frequencies and decay rates relevant to cooling and spectroscopy.

The cooling light is generated by a commercial Titanium-Sapphire laser *Coherent - MBR 110* that is pumped by a *Verdi V10* producing 1.6 W of light at  $\approx 845$  nm. This light is fed into a buildup cavity where its frequency is doubled by second harmonic generation in a lithiumtriborat ( $\text{LiB}_3\text{O}_5$ ) crystal resulting in a total power of 300 mW near the atomic resonance frequency of the singlet transition in calcium. The exact configuration has been described elsewhere [Deg04a]. The frequency of the laser light is stabilized to an external reference cavity made from ultra low expansion (ULE) glass spacer and two highly reflecting mirrors with a finesse  $\mathcal{F} \approx 1000$  [Kah14a]. This reduces fluctuations in the atom number between different experimental cycles. The stabilization is realized by an AOM that shifts the frequency of the laser light to be resonant to the TEM00-mode of the cavity and using a lock-in technique to transfer the length stability of the spacer to the wavelength of the laser by controlling the frequency setpoint of the Titanium-Sapphire laser. This locking scheme holds the advantage that long term drifts of the cavity can be corrected by a single AOM before the light is split into different beams that detuned relative to the atomic singlet transition. The main beam is split into multiple parts for the initial deceleration in the Zeeman slower, the deflection molasses, the MOT beams and the absorption imaging. The frequencies of all beams relative to the atomic transition can be individually manipulated by different AOMs. The detuning with respect to the atomic transition of each beam is chosen in a suitable way to maximize the number of atoms caught in the trap while at the same time minimizing the temperature of the sample [Naz07].

The 672 nm light used for the repumping during this phase is generated by an extended cavity diode laser (ECDL) (*Toptica DT100 + HL6714G*-diode) with its frequency stabilized to an external reference cavity made from ULE glass similar to the one the singlet MOT light is stabilized to. Powers of up to  $130 \mu\text{W}$  were used to repump the atoms back to the ground state enhancing the cooling rate and thus the number of atoms and temperature of the sample by a factor of three [App13]. The frequency of the beam can again be adjusted by tuning its frequency relative to the TEM00-mode of the cavity using an AOM. This frequency offset is also used to compensate the long term drift of the ULE spacer itself.

### 3.1.2 Intercombination transition MOT

During this initial phase of cooling on the singlet transition the temperature that can be reached is limited by a balance between heating from spontaneous emission and

velocity damping due to the velocity dependent absorption from the Doppler effect. This limit is called the Doppler limit and is about 0.8 mK for the singlet MOT. To further reduce the sample temperature a second MOT operating at a wavelength of 657 nm corresponding to the strongly forbidden intercombination transition  $^1S_0 - ^3P_1$  was used. This is generated by a ECDL laser that is stabilized to a high-finesse ULE cavity that is temperature stabilized inside a vacuum chamber and specifically mounted to suppress mechanical vibrations from the surrounding lab [Naz06]. The Pound-Drever-Hall technique [Dre83] is used to transfer the length stability of the ULE spacer to the frequency of the laser which results in a line width of 1 Hz corresponding to an instability of  $3 \cdot 10^{-15}$  (after 100 s averaging time) [Naz08]. The light that is transmitted through the cavity is amplified by a series of injection-locked slave lasers that provide a power of 20 mW for the operation of the MOT. Due to the small linewidth, i.e. long lifetime of the excited  $^3P_1$  state, the effective force on the atoms by absorption of resonant photons is less than the pull by earth's gravitation which would result in the atoms eventually leaving the trapping region of the MOT.

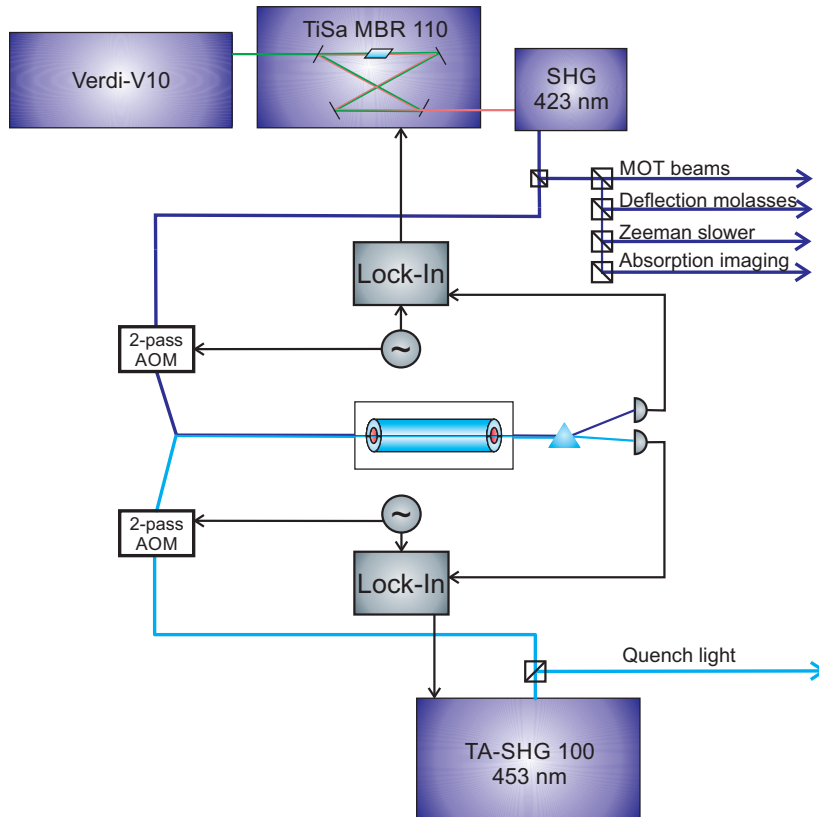


Figure 3.3: Schematic of the generation and stabilization setup of the singlet MOT and quench cooling light at 423 nm and 453 nm.

To increase the scattering rate we employ a so-called quench laser resonant to the transition  ${}^3P_1 - {}^1D_2$  [Bin01, Ste03]. Coupling these two levels helps depopulating the long lived  ${}^3P_1$  by transferring them to the fast decaying higher lying state. The light at 453 nm is generated by a *Toptica TA-SHG* system that consists of an ECDL laser amplified by a tapered amplifier at 906 nm. Subsequently the frequency of the light is doubled by second harmonic generation providing a power of 210 mW of light at the desired wavelength. To ensure that the frequency of the laser does not drift during the course of a measurement it is stabilized using the same technique and also the same cavity that was used for the singlet cooling light. The light of at the two different frequencies transmitted through the cavity is spatially separated by a prism to record the individual modulated intensity for the stabilization on separate photodiodes. A schematic of the lock-in setup is shown in Fig. 3.3.

In order to reduce the sample temperature as well as to increase the density in the atomic sample, the light of the second stage MOT also illuminates the atoms during the singlet MOT phase. By doing so the coldest atoms directly at the center of the atomic cloud absorb photons at 657 nm rendering them opaque to the first stage MOT light suppressing absorption by atoms and light induced losses [Ket93]. By application of this technique the number of atoms after the initial cooling increases by about 40 % which translates to an increase of 30 % after completion of the second MOT stage [Kah14b].

After the two initial MOT cooling phases the temperature of the sample is reduced to about 10  $\mu$ K and approximately  $4 \cdot 10^7$  atoms remain in the trap.

### 3.1.3 Evaporative cooling in an optical dipole trap

Following the two MOT phases the kinetic energy of the atomic sample is further reduced by evaporative cooling inside a crossed optical dipole trap [Kra09], which uses the natural polarizability of the atoms in the strong electromagnetic field of intense laser beams. The trapping light is generated by an Yb:YAG disc laser that is pumped by high power laser diodes reaching a pump power of 100 W. The system generates up to 15 W of laser light that is split into the tilted and horizontal trap beams. The light has a wavelength of 1030 nm which is close to a magic wavelength where the ac-Stark shift for the two levels involved in the intercombination transition  ${}^1S_0 - {}^3P_1$  are equal and cancel [Deg04a] each other. As the dipole trap is already beginning to accumulate atoms during the MOT phase the cooling would be disrupted by the

differential shift introduced by a non magical trap. Furthermore the photoassociation spectra would also suffer from broadening due to the shift of the resonance depending on the local trapping potential. The power in both beams is gradually reduced by individually designed ramps [Vog09] to reach the desired temperature while maximizing the number of atoms remaining in the dipole trap. Using this technique after about 0.6 seconds, depending on the evaporation parameters,  $\approx 1.5 \cdot 10^5$  atoms in the trap could be achieved at a temperature of  $1 \mu\text{K}$ .

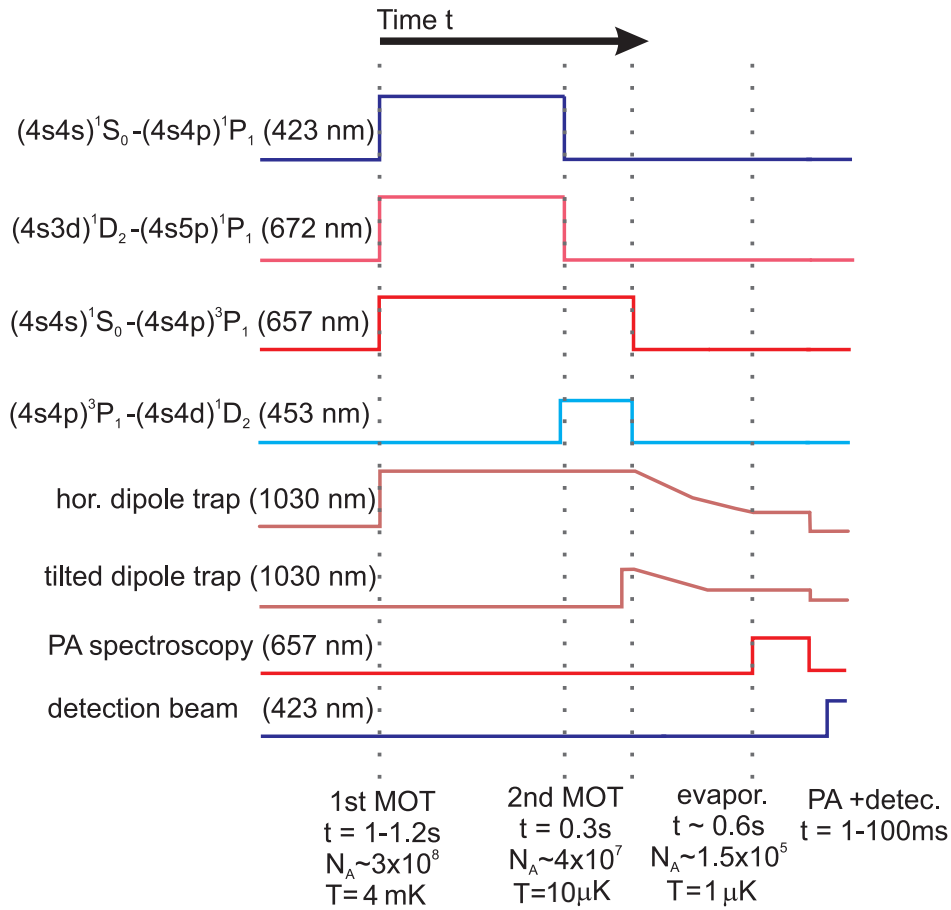


Figure 3.4: Time chart of an experimental cycle together with typical sample properties after the corresponding stages.

A full experimental sequence together with typical experimental values for atom number and sample temperature at the corresponding stages during the experiment is illustrated in Fig. 3.4.

### 3.1.3.1 Dipole trap geometry

For the evaluation of the measured photoassociation resonances in the next chapter it is of utmost importance to have precise knowledge of the trap parameters and the exact geometry of the two intersecting beams that determine the size and in turn the density of the atomic sample. The dipole trap volume  $V_{DT}$  strongly depends on the power in both dipole trap beams, the beam collimation and focusing as well as the exact angle and position of the two overlapping beams. The power of both the tilted and horizontal beam has been measured with a powermeter using a thermal sensor head calibrated to an uncertainty of 5 %. The beamwaists of the two beams have both been calculated from the characteristics of the fiber setup that guides the light from the laser to the experiment chamber. The horizontal trapping beam is formed by collimation of a beam coming from a fiber with a mode-field diameter (MFD) of  $15 \pm 2 \mu\text{m}$ <sup>1</sup> with a  $f = 100 \text{ mm}$  lens followed by a focusing lens with focal length  $f = 300 \text{ mm}$ . The optics have initially been set up to achieve a beam waist radius of  $w_0 = 33 \pm 4 \mu\text{m}$  [Vog09]. The experimental setup does not allow for a direct measurement of the beam at the crossing point of the two trapping beams without losing the ultrahigh vacuum in the experimental chamber. Further, the focusing lens is too close to the viewport through which it enters the chamber to deflect it and measure the waist in this way. Instead I have determined the width of the collimated beam in front of the focusing lens by a knife edge measurement to be 3.7 mm to verify the validity of the assumed waist. The radius of the collimated beam translates to a final waist at the focal point of  $30 \pm 3 \mu\text{m}$  also taking into account the remaining curvature of the beam, since the output facet of the fiber is by design not perfectly in the focal point of the collimation lens.

The tilted trap beam is generated in a similar way as the horizontal beam. It is formed using identical optical components except for a different optical fiber guiding the light to the vacuum chamber. The polarization maintaining fiber has a smaller MFD of  $12.6 \pm 1.5 \mu\text{m}$ . With the different fiber guiding the light towards the vacuum chamber the expected beam waist radius was calculated to be  $w_0 = 19.0 \pm 2.5 \mu\text{m}$  assuming the facet of the fiber is directly in the focal point of the collimation lens. In the case of the tilted trap the beam can be deflected right in front of its entry point into the vacuum chamber. This allows a direct measurement of the beam waist by means of

---

<sup>1</sup>For the MFD of the optical fibers I assumed the production tolerances given in the data-sheet as  $1\sigma$ -uncertainty

moving a ccd camera along the beam path while measuring the radii at each position and finally fitting a Gaussian beam evolution to the data. The measured result of  $w_0 = 19,5 \pm 1,3 \mu\text{m}$  is in good agreement with the calculation.

When calculating the trap frequencies and effective volume one has to keep in mind that the focusing lens of the tilted beam was shifted by 4.5 mm with respect to the position where both dipole trap beams intersect at their respective waists. This results in a beam radius of  $77 \mu\text{m}$  at the intersection of the two trapping beams. This modification was introduced to increase the size of the optical dipole potential which allows longer evaporation cycles leading to a more effective cooling due to a suppressed three body collision rate [Kra09].

### 3.1.3.2 Measurement of the trap frequency

Since the horizontal beam waist radius could not be directly measured by deflection of the beam it has been verified by means of a release-recapture method [Deg04a] from which the harmonic trapping frequencies could be determined. The harmonic frequency inside the dipole trap beam is directly related to the beam parameters i.e. the waist radius and power of the trapping beam. The technique relies on capturing atoms in the dipole potential of a single trapping beam. The atoms accumulate at the position of the highest light intensity in around the beam waist and the cloud takes on the shape of a cigar. Afterwards the dipole trap is switched off for a short amount of time  $t_{\text{release}} = 100 \mu\text{s}$  and the atoms expand freely in space. After the free evolution of the ensemble the trapping beam is switched on again and most of the atoms are recaptured in the dipole potential. The atoms now perform a damped oscillation in the trapping potential depending on the trap geometry and their velocity at the moment of their recapture. The oscillation evolves for a time  $t_{\text{osc}}$  after which the atoms are again released from the trap by switching off the trapping beam. Depending on the current phase of the oscillation the atoms will again expand and after another recapture cycle the fluorescence signal that is proportional to the number of recaptured atoms is measured. To reduce the uncertainty of the measurement the fluorescence was normalized by the signal without a second switch-off and corrected for the dark count rate of the photomultiplier used for the measurement. From a series of measurements at different times  $t_{\text{osc}}$  the frequency  $\omega_{\text{rad}}$  at which the atoms oscillate in radial direction in the horizontal dipole trap can be extracted from a fit of a damped oscillation to the data. From the fluorescence shown in Fig. 3.5 at a beam power of  $P_{\text{hor}} = 7 \text{ W}$  and an initial

release time  $t_{\text{release}} = 100 \mu\text{s}$  the radial trapping frequency  $\omega_{\text{rad}} = 2\pi \cdot 1550(57) \text{ s}^{-1}$  was determined. From the trapping frequency I calculated the beam waist radius according to

$$w_0 = \sqrt{\frac{4U_0}{m_{\text{Ca}}\omega_{\text{rad}}^2}}$$

with the trap depth  $U_0 = \alpha \frac{1}{2\epsilon_0 c} I_0$ . Here the polarizability of the calcium ground state for  $\sigma$  polarized light at 1030 nm is  $\alpha = h \cdot 47.25 \cdot 10^{-7} \text{ Hz}/(\text{V}^2/\text{m}^2)$  [Deg04a] and  $I_0 = \frac{2P_{\text{hor}}}{\pi w_0^2}$  denotes the peak intensity of the studied horizontal dipole trap beam. This translates to a beamwaist of  $w_0 = 36 \pm 3 \mu\text{m}$  which is in good agreement with the value of  $w_0 = 33 \pm 4 \mu\text{m}$  cited before.

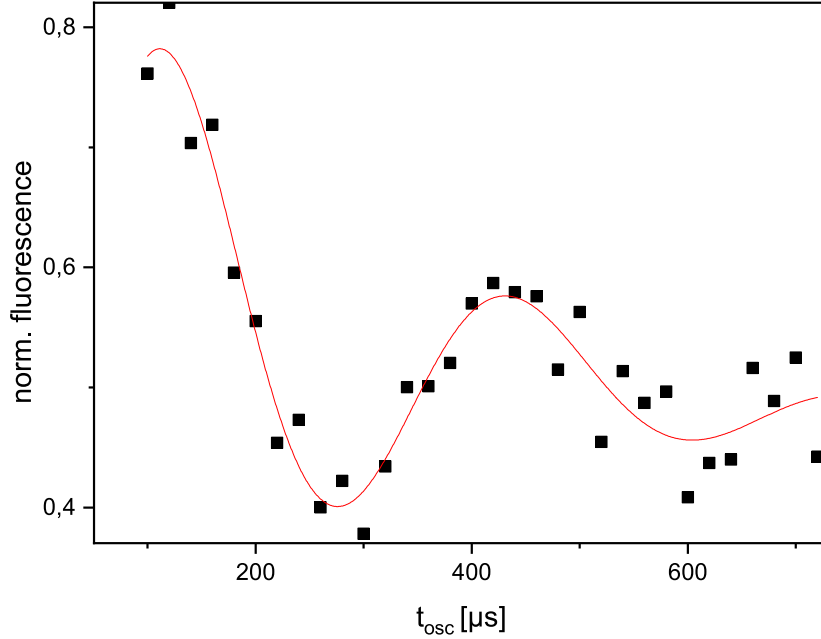


Figure 3.5: Number of recaptured atoms after different oscillation durations  $t_{\text{osc}}$  after an initial release time of  $t_{\text{release}} = 100 \mu\text{s}$  in the horizontal dipole trap. The measurements were taken at a power of  $P_{\text{hor}} = 7 \text{ W}$ .

Due to the lower power and the additional gravitational pull along the trap it was not possible to directly measure the trapping frequency of the tilted beam via the release-recapture method.

### 3.1.3.3 Calculated trap frequencies in a tilted trap

The trap frequencies inside the crossed trap have consequently been calculated for beam parameters of the individual beams during the measurements in order to estimate the



density of the atomic sample. In general the induced dipole potential acting on an atom with polarizability  $\alpha$  is given by

$$U_{\text{DF}} = \alpha \frac{1}{2\epsilon_0 c} I,$$

where  $I$  is the local intensity of the respective laser beam. After a suitable parameterization in the plane spanned by  $y$  and  $z$  that contains both trapping beams their respective potential can be expressed as:

$$U_{\text{tilt}}(y, z) = \frac{\alpha}{2\epsilon_0 c} I_{\text{tilt},0} \left( \frac{w_{\text{tilt},0}}{w_{\text{tilt}}(z)} \right)^2 \exp \left[ -2 \left( \frac{y}{w_{\text{tilt}}(z)} \right)^2 \right] \quad \text{and}$$

$$U_{\text{hor}}(y, z) = \frac{\alpha}{2\epsilon_0 c} I_{\text{hor},0} \exp \left[ -2 \left( \frac{(y \cos \beta + z \sin \beta)}{w_{\text{hor},0}} \right)^2 \right]$$

where  $z$  denotes the propagation direction of the tilted beam and  $y$  is perpendicular to the  $z$ -direction. The inclination  $\beta$  between both beams is  $54^\circ$  and the peak intensity of the individual beams is denoted by  $I_{\text{tilt},0}$  and  $I_{\text{hor},0}$ . The waist radius of the two beams is given by  $w_{\text{tilt},0}$  and  $w_{\text{hor},0}$  and since the two beams do not intersect at their respective focus points the position dependent beam radius of the tilted beam is given by  $w_{\text{tilt}}(z) = w_{\text{tilt},0} \sqrt{1 + \left( \frac{z}{z_r} \right)^2}$  with the Rayleigh length  $z_r = n\pi w_0 \lambda^{-1}$  [Met99]. For the calculation I assumed the horizontal beam crosses the tilted beam in its focal point. The complete potential  $U_{\text{tot}}$  the atoms experience is given as the sum of both beams. Assuming that the potential is harmonic around its minimum it can be written as:

$$U_{\text{tot}} = U_{\text{tilt}} + U_{\text{hor}} = \frac{\alpha}{2\epsilon_0 c} \begin{pmatrix} y \\ z \end{pmatrix} \begin{pmatrix} a + b \cos^2 \beta & b \sin \beta \cos \beta \\ b \sin \beta \cos \beta & b \sin^2 \beta \end{pmatrix} \begin{pmatrix} y \\ z \end{pmatrix}$$

with  $a = 2 \cdot I_{\text{tilt},0} \left[ w_{\text{tilt},0}^2 \left( 1 + \left( \frac{z}{z_r} \right)^2 \right)^2 \right]^{-1}$  and  $b = \frac{2 \cdot I_{\text{hor},0}}{w_{\text{hor},0}^2}$ .

By calculating the eigenvalues of the matrix in the above equation:

$$\lambda_{1/2} = \frac{a+b}{2} \pm \sqrt{\left( \frac{1}{2}(a+b) \right)^2 - ab \sin^2 \beta}$$

and relating these values to the motional eigenstates of an atom in the potential

$$U = \frac{\alpha}{2\epsilon_0 c} (\lambda_y \nu_y^2 + \lambda_z \nu_z^2) = \frac{1}{2} m_{\text{Ca}} (\omega_1^2 \nu_y^2 + \omega_2^2 \nu_z^2)$$

the trap frequencies  $\omega_1, \omega_2$  along and perpendicular to the tilted beam can be calculated for the respective trap depth during the individual measurements. To give a general impression of the magnitude I have calculated the trap frequencies for a typical configuration of the dipole trap with  $P_{\text{tilt}} = 1.2$  W and  $P_{\text{hor}} = 0.6$  W. They are given by  $\omega_1 = 715 \text{ s}^{-1}$  and  $\omega_2 = 3428 \text{ s}^{-1}$ . The squared sum of these values gives the harmonic frequency in the second radial direction that is  $\omega_3 = \sqrt{\omega_1^2 + \omega_2^2} = 3502 \text{ s}^{-1}$ .

### 3.1.4 Temperature of the atomic sample

The temperature of the sample has been determined from time-of-flight measurements using absorption images of the atomic sample. For this, a cold sample was prepared using a full experimental cycle without application of spectroscopy light and absorption images after variable times  $t$  of free-expansion were recorded. The atomic cloud expands freely after release from the dipole trap and the RMS radius  $\sigma(t)$  evolves according to

$$\sigma(t)^2 = \sigma_0^2 + \frac{k_B T}{m_{\text{Ca}}} \cdot t^2,$$

where the initial rms radius of the atomic sample at  $t = 0$  i.e. directly after the release from the trap is  $\sigma_0$ . From a series of absorption images shortly after release from the dipole trap and after an extra amount of free expansion (we routinely used four milliseconds expansion time and compared the measured rms radius to an image directly after release, i.e.  $t = 0$ ) the temperature was determined for each individual evaporation ramp used to generate the cold samples. The temperature depends on both the evaporation time sequence and the final power in both dipole trap beams.

## 3.2 Spectroscopy laser setup

The light used for the spectroscopy has to meet various characteristics in order to produce spectra that can later be evaluated. The natural linewidth of the triplet transition in calcium is smaller than 1 kHz but the line is thermally broadened depending on the temperature. The narrowest spectra we recorded are  $\approx 30$  kHz wide. Consequently the linewidth of the spectroscopy laser has to be narrow enough that the details in

the recorded loss spectra are not hidden underneath the convolution of the laser shape with the strongly wavelength dependent loss coefficient.

In the experiment this is achieved by locking an extended cavity diode laser (ECDL) to a stable reference resonator made from ultra low expansion glass transferring the high mechanical stability of the cavity to the frequency of the laser light. The cavity is housed inside a low pressure vacuum chamber and its temperature is stabilized close to a zero crossing of its thermal expansion coefficient in order to suppress thermally induced length instabilities of the reference resonator. The light is stabilized to this resonator by means of the Pound-Drever-Hall technique achieving a final line width of  $\approx 1$  Hz [Naz06, Naz07]. The reference cavity shows a small linear drift of  $\dot{f}_{\text{cavity}} = 4.75\text{kHz/day}$  which is compensated by an AOM in double pass configuration continuously changing its driving frequency to counteract the slow drift and keeping the frequency fixed near the atomic transition  $^1S_0\text{-}^3P_1$ . The stability of this so-called master laser is transferred to another ECDL that serves as the spectroscopy laser via a phase locking technique.

### 3.2.1 Phase locking technique

As a result of the Pound-Drever-Hall locking technique the light from the master ECDL has a characteristic spectral power distribution around the frequency the laser is stabilized to. This is due to the finite bandwidth of the servo loop in combination with the frequency noise of the free-running laser [Naz08]. To reduce this noise we do not use the light directly emitted by the laser but instead the light that has passed through the optical cavity which has a high spectral purity [Hal05]. This light only has a power of  $40 \mu\text{W}$  and has to be amplified via an injection locked slave laser for further applications. The amplified light is overlapped with light from a second ECDL in Littman configuration [Rie04] and the beat note between the two lasers is monitored using a photodiode that is able to measure frequencies up to 1.6 GHz. This range allows to perform spectroscopy on the two most-weakly bound states in the excited molecular potentials  $c0_u^+$  and  $(a, c)1_u$ . The setup can also be used with a different fiber coupled photodiode assembly that allows detection of the beat note from 4 to 40 GHz instead in order to probe more deeply bound rovibrational states. The signal of this photodiode is mixed with the output of a signal generator *Marconi 2024* such that the difference between the two radio frequencies is around 100 MHz. The signal is filtered by a band pass filter centered at 100 MHz rejecting the sum frequency and fed to a

phase frequency comparator that compares this signal to a stable 100 MHz reference. The output of the phase-frequency comparator is divided into a part that is used to correct fast frequency fluctuations that is applied directly to the current of the laser diode while a second servo signal controls a piezo actuator that shifts the mirror inside the laser adjusting slow frequency drifts of the laser up to typically a few kHz. Through this *phase locking* technique the frequency of the spectroscopy laser can be tuned relative to the stable reference by slowly adjusting the output frequency of the signal generator while keeping the narrow linewidth of the spectrally filtered light from the stable resonance. The beat between the narrow light from the cavity-locked reference

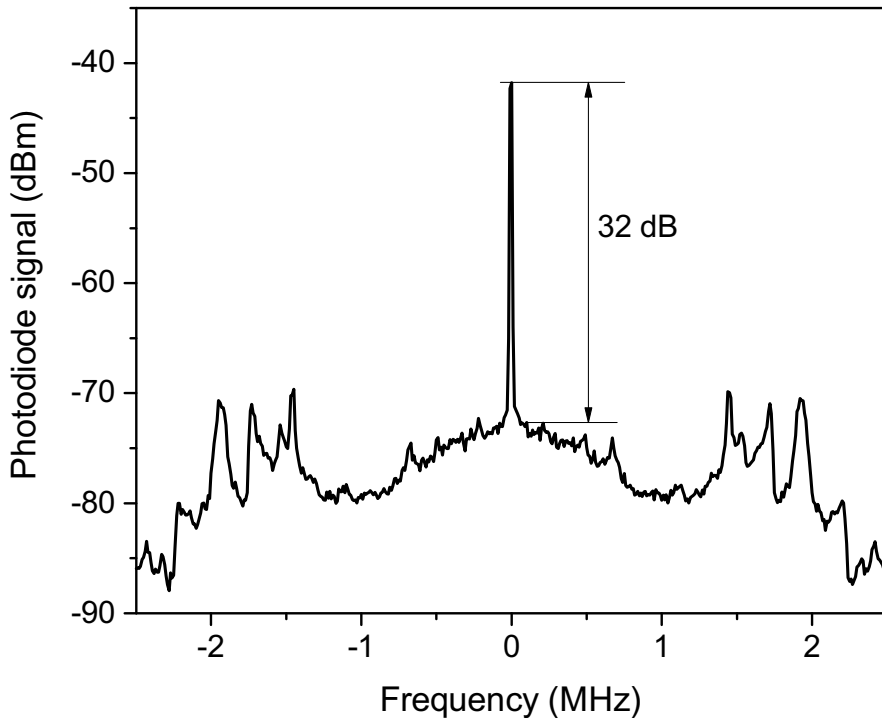


Figure 3.6: Beat between the reference cavity locked ECDL and the offset phase-locked ECDL. Most of the spectral power is located in the central carrier peak 32 dB above the background. The spectrum was measured using a fast photodiode on a spectrum analyser *Rigol DSA 815* with a RBW of 1 kHz averaging over 100 measurements.

and the phase-locked spectroscopy beam is shown in Fig. 3.6. One can immediately see most of the power is concentrated at the distinct peak that is at least 32 dB above the suppressed background in its direct vicinity ( $\pm 100$  kHz). At approximately  $\pm 1.4$  MHz there are undesired peaks in the spectrum that are related to the electronic servo of the unfiltered light of the reference laser and are not present in the spectroscopy light. The integrated power in the carrier peak amounts to 92 % of the total power

of the spectroscopy beam measured by a power-meter. This fraction has been taken into account when determining the incident photoassociation intensity that is crucial for the evaluation of the measured atom losses in the next chapter.

### 3.2.2 Effective photoassociation intensity

There are other systematic uncertainties that have to be taken into account to properly estimate the light intensity the atoms experience during the spectroscopy. First of all, part of the light of the spectroscopy beam illuminating the atoms is reflected and absorbed by the viewports of the vacuum chamber. This effect has been estimated by measuring the power of the spectroscopy beam before it enters the experiment chamber and comparing it to the power after passing through the empty chamber. In total the power of the beam passing through two identical viewports is reduced by 8%. Consequently I assumed that the spectroscopic intensity is reduced by  $\approx 4\%$  at the location of the studied atomic samples. This effect has to be combined with the transfer efficiency determined in the last section leading to a combined reduction of the incident power by 12% in total.

I have further considered that potentially the local intensity is reduced by an imperfect overlap of the spectroscopy beam with the atoms inside the trapping region. The initial size of the dipole trap strongly depends on the final power in the trapping beams after evaporation but generally it is smaller than  $\sigma_{\text{rad}} = 30 \mu\text{m}$  in the direction of its biggest extension. This beam has to be overlapped with the spectroscopy beam whose beam waist radius has been measured with a CCD camera to be  $w_0 = 50(3) \mu\text{m}$ . It is very difficult to estimate the exact overlap of the beam with the cold atoms since it is not possible to access the region of the atom cloud in the vacuum chamber and directly measure the power and radius of the beam in situ. Instead the overlap could only be determined indirectly. I have used an iterative procedure to optimally align the atom cloud and photoassociation beam. First, the spectroscopy beam is tuned to the atomic resonance frequency and roughly overlapped with the cold sample. The number of atoms in the ground state measured by absorption imaging is reduced as soon as atoms are excited to the triplet state and due to the low saturation intensity of the intercombination transition very low laser power already excites every atom in the sample. As the number of atoms is monitored the power in the spectroscopy beam is gradually reduced. At sufficiently low power in the beam a fraction of atoms is no longer excited which is when the spectroscopy beam is realigned in order to minimize

the remaining atoms again. The alignment of the center of the Gaussian spectroscopy beam with the center of atomic cloud is achieved by moving the focusing lens right in front of the vacuum chamber perpendicular to the collimated spectroscopy beam. This process is continuously repeated until an optimal configuration is found for which a minimal incident power removes most atoms from the trap. In a second step the focusing lens is shifted along the propagation direction of the beam resulting in a shift of the waist relative to the atomic cloud until the measured number of atoms in this direction is also minimized. Since it is not possible to directly measure the intensity at the position of each individual colliding atom pair I assumed an uncertainty of 20 % for the intensity calculated from the power measured in front of the window and the beam waist.

### 3.3 Experiment control

The individual components of the experiment are remotely controlled by a personal computer. A control program communicating with a *Becker & Hickl PPG-100* bit pattern generator serves as the basis of the experiment where the time schedule for experimental cycle is stored at the beginning of each measurement. The PPG generates digital control signals for the different components of the experiment:

- the mechanical shutters blocking the path of beams that are not utilized during the different experimental stages,
- the voltage controlled oscillators that for example power the AOM regulating the intensity of the spectroscopy beam,
- the trigger of the avalanche photo-diode recording the fluorescence during the blue and red mot stages,
- the power supplies of the magnetic coils during the MOT phases and for the offset magnetic fields,
- and the PID controllers steering the dipole trap ramping process.

The setup of the magnetic coils as well as ramps of the dipole traps are also configured in the same software and stored in a *National Instruments 6733 PXI* digital-analog converter as voltage ramps. Via a *National Instruments BNC-2110* breakout-box the

ramps are fed into PID controllers that are stabilizing the readout of photodiodes recording the incident dipole trapping beam powers allowing individually designed gradients leading to different final trap temperatures. The photoassociation laser fre-

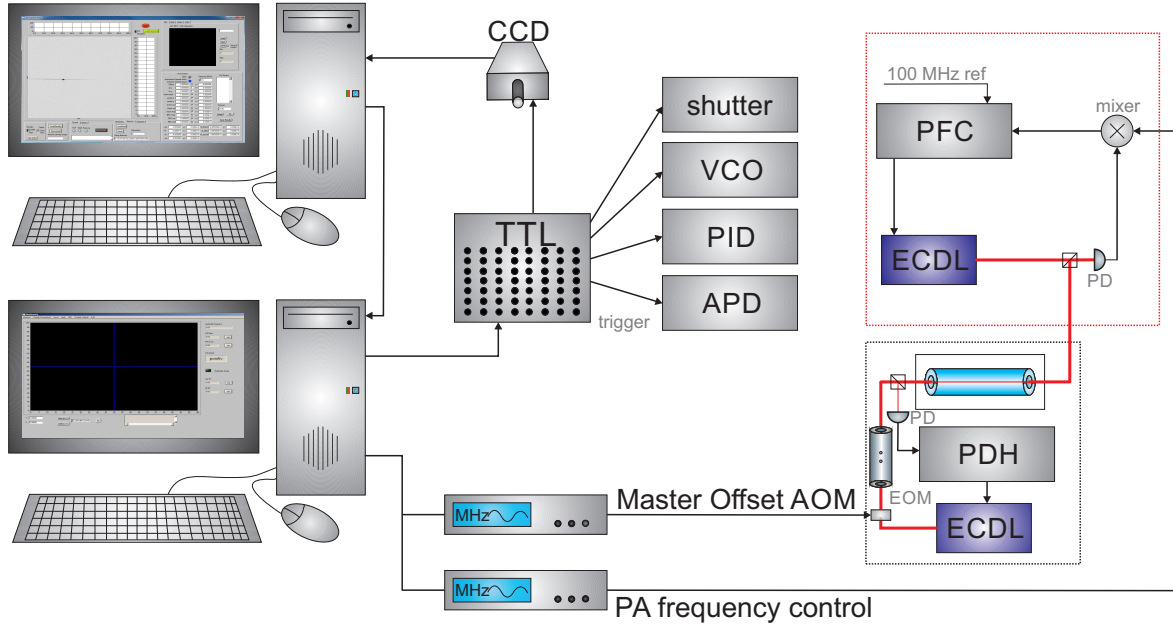


Figure 3.7: Overview over the experimental components that are centrally controlled by the measurement software. Both the master laser frequency used for cooling during the red MOT phase as well as the frequency of the offset-locked spectroscopy laser can be controlled individually. The explanation for the different abbreviations can be found in the text.

quency can be adjusted by changing the frequency output of the signal generator *Marconi 2024* that is connected to the computer via a GPIB-LAN interface enabling custom frequency stepping. If the individual step size does not exceed 20 kHz the spectroscopy laser stays locked relative to the reference. Bigger steps would lead to a failure of the offset-lock stabilizing the spectroscopy laser to the stable master laser. A second computer evaluates the absorption images taken by a *Photometrics ColdSnap ES* CCD camera and transmits the result of each individual measurement to the computer controlling the experiment. This solution has been chosen to reduce load due to saving three high resolution camera pictures and calculating the optical density and potentially negatively impacting the experimental cycles.





## Chapter 4

### Photoassociation: From low to high power

In this chapter I examine the photoassociation spectra of molecular states of the bosonic isotope of calcium  $^{40}\text{Ca}$  in a wide range of intensities. Transitions to two different bound states have been investigated and compared to theoretical expectations relying on the description of the photoassociation process described in Chapter 2 and the experimental parameters given in Chapter 3. The two rovibrational states of  $^{40}\text{Ca}_2$  in the potentials  $0_u^+$  and  $1_u$  that have been experimentally probed are in the following denoted by  $v' = -1; \Omega = 0$  and  $v' = -1; \Omega = 1$ , respectively. The states are bound at energies of  $E_{\Omega=0} = -0.308700(8) \text{ GHz} \cdot h$  and  $E_{\Omega=1} = -0.982977(7) \text{ GHz} \cdot h$  making them the two most-weakly bound states below the molecular asymptote [Kah14b] dissociating to atomic states  $^3P_1 + ^1S_0$ . They have been chosen due to the comparatively strong overlap with the ground state scattering wave function which implies a good coupling to the ground state continuum and the highest photoassociation event rate for states belonging to the asymptote  $^3P_1 + ^1S_0$ . The high rates are beneficial for the experimental implementation since they allow for photoassociation times much shorter than the lifetime of the dipole trap, leading to higher number of atoms and an improved signal to noise ratio in the resulting data. The analysis of the data presented is affected by a variety of uncertainty contributions, e.g. intensity fluctuations in the photoassociation beam, that will be treated in detail in the next chapter.

Due to the comparatively small electric dipole coupling to the excited triplet state applications relying on this interaction often use high intensities to produce an appreciable effect. For example, a change of the scattering length by means of an optical Feshbach resonance would benefit from high laser intensities [Nic15a]. On the other hand we know from atomic physics that at high spectroscopic intensities saturation effects are expected and part of this work is to investigate the saturation behavior of photoassociation resonances.

The presented measurements are evaluated with a special interest in the rate of pho-

toassociation events as well as the resonance shape as the spectroscopic intensity is varied. As explained before saturation effects are expected at the highest intensities. The saturation intensity of the investigated molecular transitions has been introduced before (see Eq. 2.21) which translates to values of

$$I_{\text{sat,PA},\Omega=0} = 2.65 \text{ Wcm}^{-2} \quad \text{and} \quad (4.1)$$

$$I_{\text{sat,PA},\Omega=1} = 8.09 \text{ Wcm}^{-2} \quad (4.2)$$

for the two investigated molecular resonances. The Franck-Condon density for this calculation of the molecular saturation intensity has been evaluated at the respective sample temperature i.e. for a transition to the state  $v' = -1; \Omega = 0$  at  $T = 1.08 \mu\text{K}$  and for the transition to  $v' = -1; \Omega = 1$  at  $T = 0.8 \mu\text{K}$ . One has to keep in mind that this definition is somewhat arbitrary since the atomic saturation is defined for a closed two level atomic transition while the photoassociation has a defined excited state but a continuum of initial scattering states that are populated by a thermal distribution. At intensities higher than  $I_{\text{sat,PA},\Omega=0,1}$  the shape of the photoassociation line is expected to start to broaden due to the increasing stimulated width  $\Gamma_{\text{stim}}$  defined in Eq. 2.2. A series of photoassociation spectra showing the loss of atoms from an optical trap was taken at different peak intensities of the spectroscopy beam. The used spectroscopic intensities ranged from below  $1 \text{ Wcm}^{-2}$  up to almost  $600 \text{ Wcm}^{-2}$ . From the previously estimated values for the saturation intensity it should be possible to clearly witness saturation and broadening effects from the measurements.

In order to quantify the effect of light-assisted molecule formation in an experiment samples of atoms at very low temperatures were produced in quick succession. These samples of atoms at temperatures around one micro-kelvin are then illuminated by a focused spectroscopy beam resonantly tuned closely to the excitation energy of a weakly bound molecular state in the interaction potential close to the  ${}^3P_1 - {}^1S_0$  asymptote. The frequency of the spectroscopy laser is subsequently scanned across the molecular resonance in equidistant steps to record a single photoassociation spectrum. As the laser photon energy is tuned closer to the difference between the initial collision energy of the atom pair and the energy of the molecular state more atoms are weakly bound into a molecule thus reducing the number of atoms in the sample as they either decay back to free atoms that are lost from the trap due to their kinetic energy or to other bound molecular states that can no longer be detected. The optical density of the atomic sample is then measured by absorption imaging from which the atom

number as a function of frequency can be estimated. Finally, from the trap losses the photoassociation loss coefficient  $\langle K(\nu) \rangle$  was calculated by application of the theoretical formalism described in chapter 2 and the precise description of the experimental parameters.

The resonance position provides insight into the binding energy of the molecular state while the shape of the resonance and the magnitude of the trap loss are directly connected to the optical coupling between the scattering continuum and the molecular state. Comparing the measurements to simulations can provide understanding of possible limitations of the theoretical description and further our knowledge of the photoassociation process.

The relevant parameters for the measurement are the photoassociation light intensity  $I_{\text{PA}} = \frac{2P_{\text{PA}}}{\pi w_{\text{PA}}^2}$ , the power in both dipole trap arms after the evaporative cooling  $P_{\text{hor}} = 1.2$  (1.0)<sup>1</sup> W and  $P_{\text{tilt}} = 0.6$  (0.25) W resulting in the respective radial and axial trapping frequencies  $\omega_{\text{rad1}} = 2\pi \cdot 545$  (356) s<sup>-1</sup>,  $\omega_{\text{rad2}} = 2\pi \cdot 557$  (371) s<sup>-1</sup> and  $\omega_{\text{ax}} = 2\pi \cdot 114$  (102) s<sup>-1</sup>, and the duration  $\tau_{\text{PA}}$  the trapped atoms are illuminated. All of these parameters are integral for the quantitative analysis of the spectra later. For the evaporation ramp used during these measurements the temperature of the atomic sample was determined to  $T = 1.08$  (0.8)  $\mu\text{K}$ . In addition to the measured atom number simulations based on the theoretical formalism according to Eq. 2.14 were added to every trap loss spectrum to allow a comparison of the expected shape and rate of the resonance. In the case that the simulation shows a deviation in the absolute loss of atoms from the trap this is corrected by a scaling factor that facilitates the analysis regarding the width of the curve.

An example of photoassociation spectra measured at different intensities is shown in Fig. 4.1. The effect of increasing the photoassociation intensity can be seen from the graphs. At higher intensity the center of the line i.e. the resonance position is shifted by an increasing AC Stark shift. In the given example the peak loss position is shifted by  $\approx 70\text{kHz}$ . Comparing the first and second graphs in Fig. 4.1 the photoassociation duration  $\tau_{\text{PA}}$  is kept constant while the intensity in the lower Graph was increased by more than a factor of two. At medium intensities the peak loss rate increases with the spectroscopic intensity while the overall shape is unaltered. The last graph shows the highest spectroscopic intensity that was used to probe the  $v' = -1; \Omega = 0$  level and serves as an example of the power broadening of the line discussed before.

---

<sup>1</sup>The values given in brackets are the parameters corresponding to the measurements of the  $v' = -1; \Omega = 1$  state.

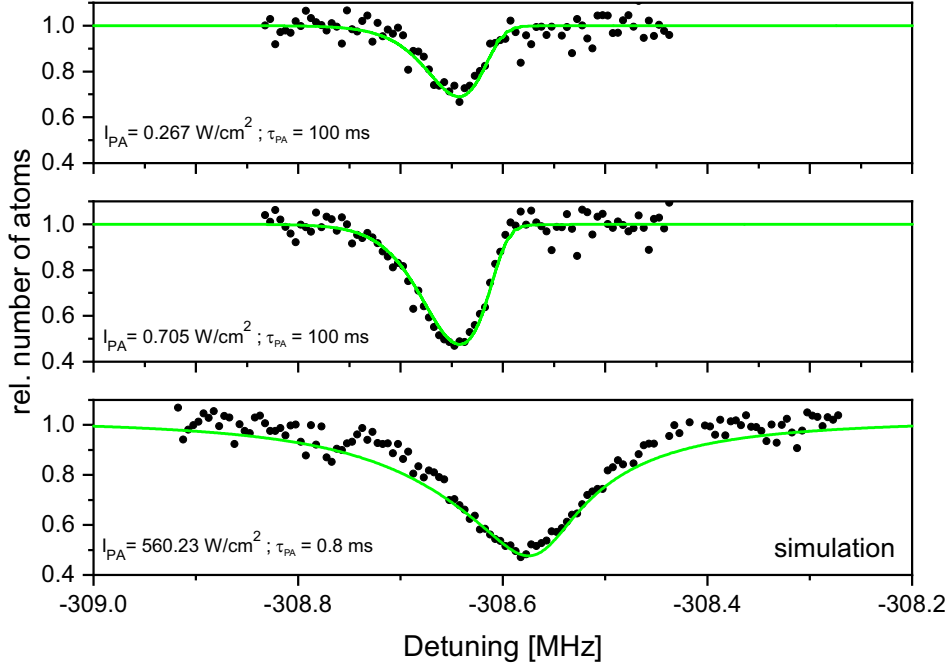


Figure 4.1: Atom loss depending on the detuning on the photoassociation laser frequency scanning across the molecular level  $v' = -1$ ;  $\Omega = 0$  at intensities of  $I_{\text{PA}} = \{0.267; 0.705; 560.23\} \frac{\text{W}}{\text{cm}^2}$  (top to bottom). The red solid line shows a simulated spectrum adjusted to the peak losses of the experiment.

## 4.1 Low intensity spectra

First I will focus on the description of individual photoassociation spectra at low intensities compared to the molecular saturation intensity. In this intensity range the measured spectra are dominated by thermal effects in the atomic sample. The atomic motion can be divided into two parts: the relative motion of the two colliding atoms in their center of mass frame and the movement of the center of mass itself with respect to the direction of the incoming spectroscopy photons. The former induces a thermal shift that causes an asymmetric broadening of the line following a Boltzmann distribution, while the latter induces a Doppler shift that inhomogeneously broadens the recorded spectrum. Both shifts are depending on the temperature of the atomic sample which is one of the reasons the experiments are performed at low  $\mu\text{K}$  temperatures.

In Figure 4.2 the spectra of both examined molecular states at their respective lowest recorded photoassociation power  $P = 0.11 \text{ mW}$  and  $P = 0.57 \text{ mW}$  are presented. These powers correspond to intensities of  $I_{\text{PA}} = 0.27 \text{ Wcm}^{-2}$  and  $I_{\text{PA}} = 1.28 \text{ Wcm}^{-2}$  irradiating the cloud of cold atoms, respectively. The intensity already considers the transfer efficiency of the offset lock and the attenuation by the viewport which reduces

the calculated peak intensity by 12 %. For both molecular states the number of atoms as a function of the detuning relative to the atomic asymptote  ${}^3P_1+{}^1S_0$  show a distinct resonance feature close to the binding energy of the respective molecular state. At the center of the resonance up to 30 % of the initial atoms are lost at the chosen illumination time  $\tau$  which is given in the description of the graphs. The linewidth of the resonance features was determined by fitting of a Gaussian to the atom loss coefficient  $\beta$ . I found that the atom loss spectrum is well fit by a Gaussian which can be explained by the fact that the thermal broadening is much larger than the width of the photoassociation line for a fixed collision energy. The width at the lowest intensity were determined to 55 kHz and 38 kHz for the resonance in  $\nu' = -1; \Omega = 0$  and  $\nu' = -1; \Omega = 1$ , respectively. In order to calculate the loss rate  $\beta$  from the atom number Eq. 2.19 was evaluated with the respective irradiation time  $\tau_{\text{PA}}$ . Also shown are simulated atom losses from numerical calculation of the thermally-averaged density related loss coefficient  $\langle K(\Delta) \rangle$  from Eq. 2.14 that was subsequently converted to the atom loss rate  $\beta$ .

The measured remaining number of atoms in the optical trap is substantially higher than one would expect from the simulated photoassociation spectra. To exclude that this is a singular effect I have also studied spectra recorded at various intensities below saturation. I have compared the peak loss coefficient  $\langle K(\Delta) \rangle$  to calculated values and found that for the  $\nu' = -1; \Omega = 0$  state the simulated loss coefficient needs to be reduced by a factor of 19 in order to agree with the experimental data. This factor is the same for the three lowest intensities ( $I_{\text{PA}} = \{0.27; 0.40; 0.71 \text{ Wcm}^{-2}\}$ ) used during the measurements. The same has been done for the  $\nu' = -1; \Omega = 1$  state where the factor was determined to be 16 instead. Possible explanations for this deviation will be discussed in detail in section 4.3. For an easier comparison of the shape of the resonances the simulated loss coefficients have been scaled to match the experimentally measured peak loss rates. Except for the absolute rate the simulations at low intensities show a good agreement with the measured data in terms of shape and width of the resonance feature. The width is also in good agreement with the value expected from the thermal movement of the atoms. The width introduced through the center-of-mass motion of the atoms with respect to the direction of the spectroscopy beam can be calculated by

$$\Gamma_{\text{D}} = \frac{1}{2\pi} k_{\text{las}} \sqrt{\frac{k_{\text{B}} T}{2m_{\text{Ca}}}} = 22.8 \text{ kHz.} \quad (4.3)$$

The width originating from the relative motion of the atom pair corresponding to the shift of the resonance condition by the initial collision energy of the scattering state on

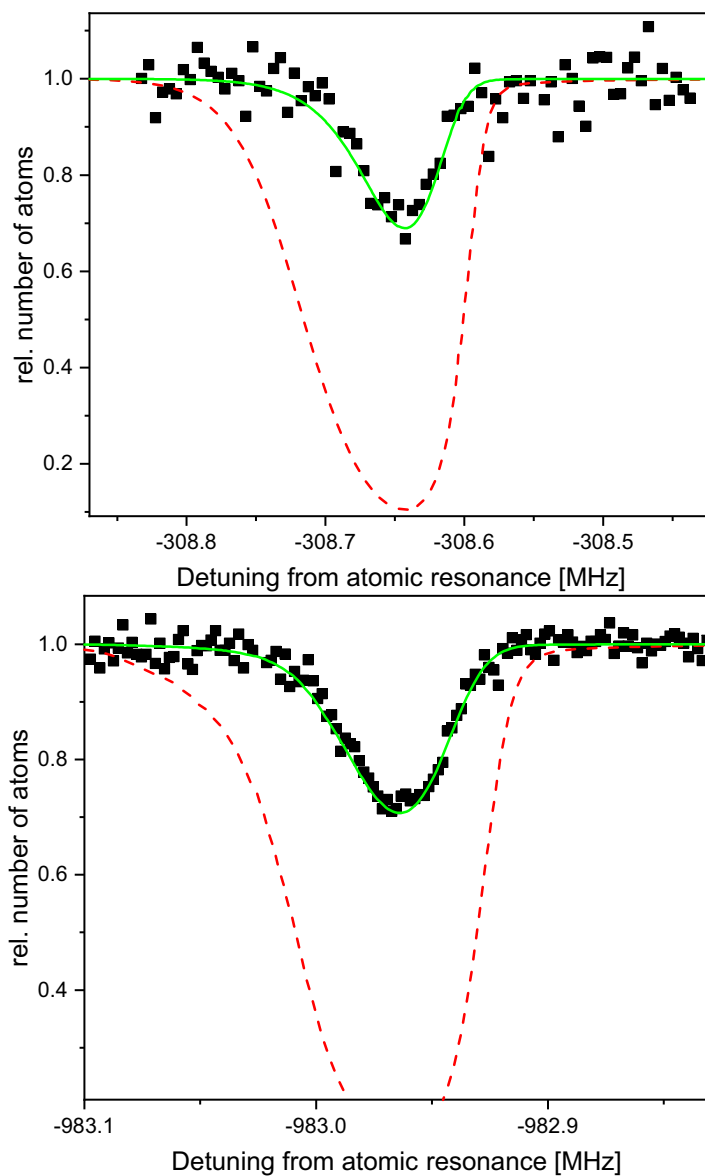


Figure 4.2: Atom loss at low intensity depending on the detuning on the photoassociation laser frequency for the molecular level (a)  $v' = -1; \Omega = 0$  and (b)  $v' = -1; \Omega = 1$  at an intensity of  $I_{\text{PA}} = 0.27 \frac{\text{W}}{\text{cm}^2}$  ( $\tau = 100\text{ms}$ ) and  $I_{\text{PA}} = 1.28 \frac{\text{W}}{\text{cm}^2}$  ( $\tau = 50\text{ms}$ ), respectively. Also shown are the corresponding spectra (red dashed curve) simulated using the same experimental parameters according to Eq. 2.14 together with a simulation (green curve) scaled to match the experimentally measured losses in the center of the resonance.

the other hand is

$$\Gamma_T = \frac{3}{2}k_B T = 33.7 \text{ kHz.} \quad (4.4)$$

These calculations assumed a sample temperature of  $1.08 \mu\text{K}$ . The total thermal width is  $\Gamma_{\text{therm}} = 56.6\text{kHz}$  and  $\Gamma_{\text{therm}} = 44.7\text{kHz}$  which is in agreement with the measured values considering the uncertainty of 20 % for the time-of-flight temperatures  $1.08 \mu\text{K}$  and  $0.8 \mu\text{K}$  during the measurement of the respective states. The good agreement between calculated and experimentally measured width at low spectroscopic powers is reasonable since the width of a photoassociation resonance at a fixed collision energy is below 1 kHz in this intensity range i.e.  $\Gamma_{\text{PA}} = \gamma_{\text{mol}} + \Gamma_{\text{stim}} \ll \Gamma_D + \Gamma_T$  and thus the measured curve is dominated by thermal effects.

## 4.2 High intensity spectra

Until now the focus was on the measurements that were taken at comparatively low intensities whereas this chapter concentrates on experimental data using photoassociation intensities up to 100 times larger than the molecular saturation intensity calculated at the beginning of the chapter. At high enough power of the spectroscopy beam the molecular resonance linewidth broadens until it becomes comparable to the combined thermal and Doppler width. At that point there should be a visible effect in the spectra.

Fig. 4.3 shows the measured spectra for both molecular states at the highest values of photoassociation intensities, i.e.  $I_{\text{PA}} = 560.2 \text{ Wcm}^{-2}$  and  $I_{\text{PA}} = 569.2 \text{ Wcm}^{-2}$  for the transition to  $v' = -1; \Omega = 0$  and  $v' = -1; \Omega = 1$  respectively. As in the case of the low intensity spectra the simulation was adjusted to equalize the loss rate at the center of the resonance with the measured values to simplify the comparison of the photoassociation lineshape. Contrary to the low intensity spectra shown in the last section the measured rates are now much closer to the simulated value. For the molecular state in  $v' = -1; \Omega = 0$  the experimental value is now higher than predicted by the simulation by a factor of 3.5 contrary to the behavior at low intensity. The measurement of the  $v' = -1; \Omega = 1$  requires almost no scaling at the highest recorded intensity where the simulation result was reduced by a factor of 1.5 to match the experimental loss rate. The width of the respective lines is again determined from  $\beta$  and gives values of 100 kHz and 55 kHz, which is bigger than in the low intensity case. The broadening

of the spectral lines is in agreement with calculations of the stimulated rate  $\Gamma_{\text{stim}}$ . It is evident from the spectra at the highest intensities that the broadening is more pronounced for the  $v' = -1; \Omega = 0$  line compared to the  $v' = -1; \Omega = 1$  line. This is due to the bigger overlap between the scattering and molecular wavefunction i.e. the Franck-Condon density of the more weakly bound state  $v' = -1; \Omega = 0$  is bigger by a factor of three compared to the state  $v' = -1; \Omega = 1$ .

The dependency of the photoassociation rate and resonance width from the used photoassociation intensity will be analyzed in the next sections.

### 4.3 Comparison of photoassociation rates: Experiment vs simulation

The theoretical description of the photoassociation process presented in chapter 2 is formally limited to the intensity region far from saturation. For many applications e.g. optical Feshbach resonances one is more interested in the behavior at high power since at higher intensities a more significant modification of the scattering length is expected which is often desired to enable more efficient evaporative cooling for example. Measurements of the photoassociation rate taken over a large range of spectroscopic intensities will be presented in the following section. In order to effectively compare the absolute molecule formation rate at different photoassociation intensities I have incorporated the complete photoassociation resonance in the analysis rather than a single point e.g. the rate at peak position. Thus the integrated loss rate was calculated as:

$$\langle K \rangle_{\text{area}} = \int_{-\infty}^{\infty} \langle K(\Delta) \rangle d\Delta, \quad (4.5)$$

where  $\langle K(\Delta) \rangle$  is the photoassociation loss rate depending on the detuning  $\Delta$  from the molecular resonance as defined in Eq. 2.13. Integrating the photoassociation rate holds the advantage that it is independent of inhomogeneous Doppler and thermal broadening. Furthermore it is more robust against fluctuations during a single measurement by averaging over multiple data points instead of only looking at the peak losses in the center of the resonance.

To calculate the loss factor it is important to remember that the integrated rate  $\langle K \rangle_{\text{area}}$



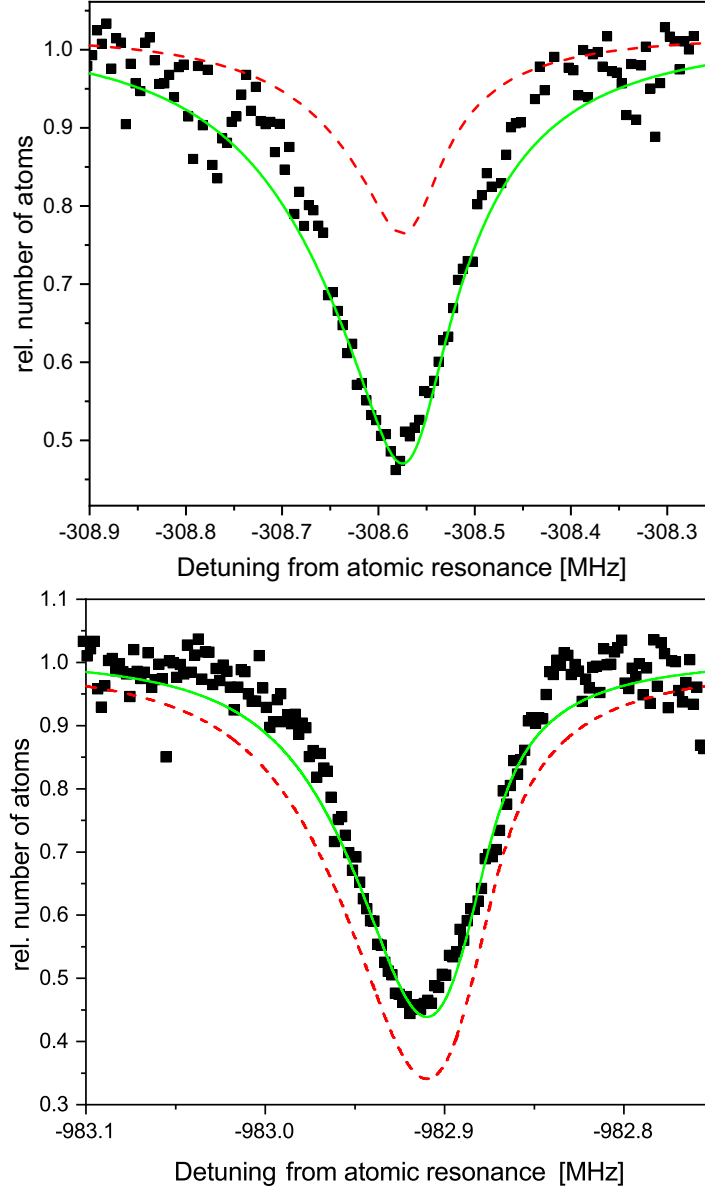


Figure 4.3: Atom loss at high intensity depending on the detuning of the photoassociation laser frequency from the atomic transition for transitions to molecular levels (a)  $v' = -1; \Omega = 0$  and (b)  $v' = -1; \Omega = 1$  at an intensity of  $I_{\text{PA}} = 560.2 \frac{\text{W}}{\text{cm}^2}$  ( $\tau = 0.8\text{ms}$ ) and  $I_{\text{PA}} = 569.2 \frac{\text{W}}{\text{cm}^2}$  ( $\tau = 2\text{ms}$ ), respectively. Also shown are the corresponding spectra (red dashed curve) simulated using the same experimental parameters according to Eq. 2.14 together with a simulation (green curve) scaled to match the experimentally measured losses in the center of the resonance.

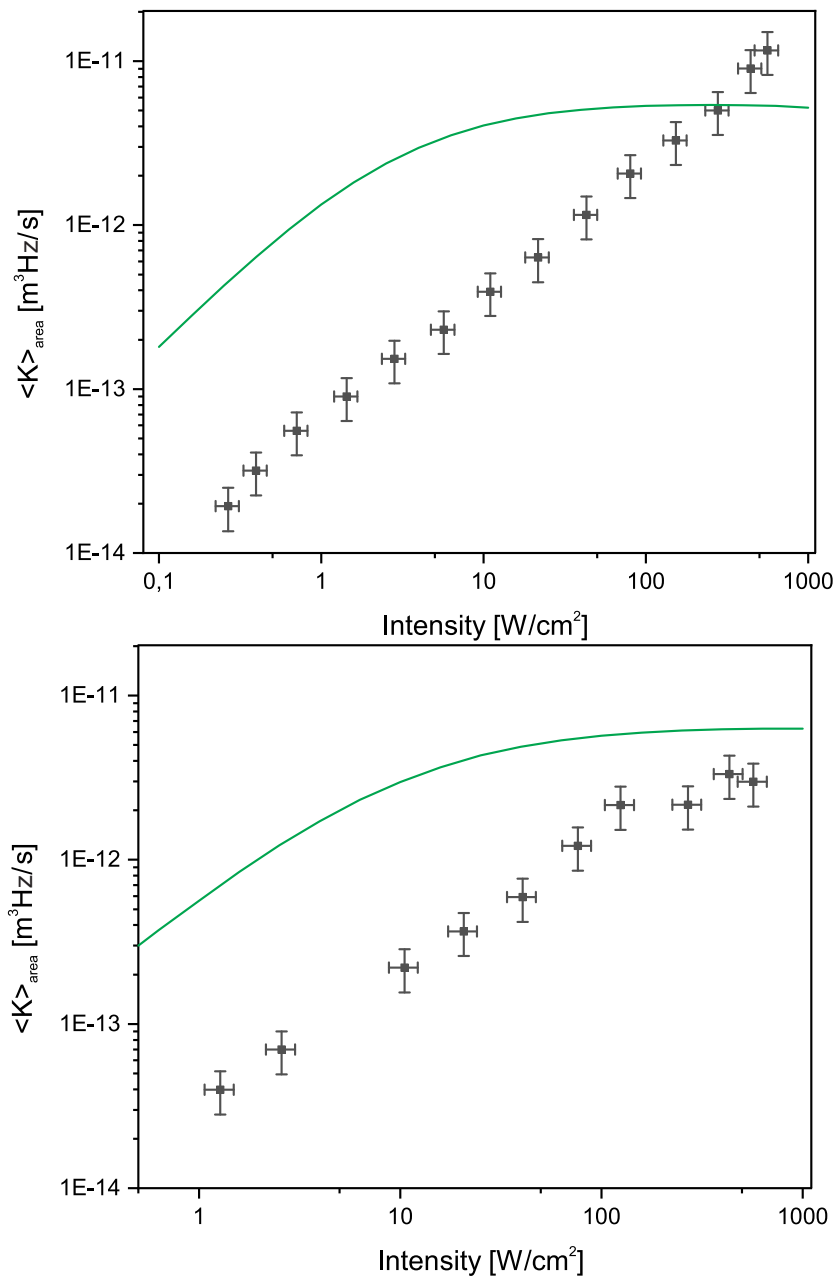


Figure 4.4: Photoassociation loss factor  $\langle K \rangle_{\text{area}}$  deduced from the measured atomic losses for different photoassociation intensities. The top graph shows the values for the  $\nu' = -1; \Omega = 0$  state and the bottom graph shows the  $\nu' = -1; \Omega = 1$  state result. The line indicates the integrated rate from simulated spectra according to Eq. 4.5.

acts on the local atom density inside the trap while in the experiment one only has access to the total number of atoms in the trap estimated from the optical density of the sample. The atom loss factor  $\beta(\Delta)$  can be directly extracted from the measured loss spectrum  $N_{\text{Atom}}(T, \Delta)$  by Eq. 2.19 and then converted into the density related loss rate  $\langle K(\Delta) \rangle$  using Eq. 2.17 that can be compared to numerical calculations of  $\langle K \rangle_{\text{area}}$ . It is obvious that in order to accurately evaluate the experiment precise knowledge of the dipole trap parameters in the trapping region is crucial since it enters directly in the conversion of  $\beta$  to  $\langle K(\Delta) \rangle$  in the form of  $V_{\text{DT}}$ .

The result of this analysis is shown in Fig. 4.4 together with a simulation according to the theoretical formalism that was introduced earlier. The error bars of the experimental values have been constructed from different uncertainty contributions and an overview is given in Tab. 4.1. The conversion of the atomic loss factor  $\beta$  to the density related loss  $\langle K \rangle$  that enters through the effective dipole trap volume  $V_{\text{DT}}$  contributes the most to the uncertainty as the exact geometry of the trapping beams could not be determined as the experiment was performed. Additionally to the exact geometry other experimental parameters further contribute to the uncertainty of the trapping volume. The sample temperature determined by time-of-flight measurements is the biggest contribution to the final value while the trapping frequencies calculated from the power in the tilted and horizontal trapping beam give a smaller contribution to the uncertainty. As detailed in chapter 3 the harmonic frequencies were calculated from the trap beam parameters and the focusing optics.

The intensity of the photoassociation light at the position of the atomic sample is a second source adding to the total uncertainty independent of the optical trap. Both the radius as well as the power of the spectroscopy beam and most importantly the deviation from a perfect overlap of the beam with the trapping region had to be considered to determine the intensity the atoms experience.

Another source of uncertainty arises from the determination of the area under the loss coefficient curve  $\langle K(\Delta) \rangle$ . Depending on the spectroscopic intensity the shape of the resonance is best described by either a Gaussian or Lorentzian. At low intensity the resonance shape is dominated by thermal broadening effects while at higher intensity the increasing stimulated width of the photoassociation line is better described by an Lorentzian. To account for this, I have fitted a Gaussian and a Lorentzian to  $\beta$  as a function of the detuning from the atomic asymptote and compared the results to the area determined from numerical integration. I have then used the uncertainty of the fit that best agrees with the numerical result to further calculate the combined

experimental uncertainty.

dipole trap volume $V_{DT}$			
variable $X$	uncertainty $u_X$	$u_{V_{DT}}(X)$	$(\sum u_{V_{DT}}(X)^2)^{\frac{1}{2}}$
temperature $T$	$0.15 \cdot T$	$0.23 \cdot V_{DT}$	$0.3 \cdot V_{DT}$
hor. waist $w_h$	$0.05 \cdot w_h$	$0.1 \cdot V_{DT}$	
tilt waist $w_t$	$0.05 \cdot w_t$	$0.15 \cdot V_{DT}$	
hor. power $P_h$	$0.05 \cdot P_h$	$0.05 \cdot V_{DT}$	
tilt power $P_t$	$0.05 \cdot P_t$	$0.03 \cdot V_{DT}$	
fit and integration of $\beta$			
variable $X$	uncertainty $u_X$	$u_{\beta}(X)$	$(\sum u_{\beta}(X)^2)^{\frac{1}{2}}$
fit uncertainty		$(0.1 - 0.2) \cdot \beta$	
photoassociation intensity $I_{PA}$			
variable $X$	uncertainty $u_X$	$u_{I_{PA}}(X)$	$(\sum u_{I_{PA}}(X)^2)^{\frac{1}{2}}$
PA power $P_{PA}$	$0.05 \cdot P_{PA}$	$0.05 \cdot I_{PA}$	$0.16 \cdot I_{PA}$
PA waist $w_{PA}$	$3 \mu\text{m}$	$0.12 \cdot I_{PA}$	
overlap w. DT		$0.1 \cdot I_{PA}$	

Table 4.1: Contributions to the uncertainty of the integrated photoassociation rate. The individual items in the table are discussed in detail in the text.

I have found that at the lowest intensity the integrated loss is

$$\langle K \rangle_{\text{area}} (0.27 \text{ Wcm}^{-2}) = (1.93 \pm 0.57) \cdot 10^{-14} \text{ m}^3 \text{ Hz/s},$$

compared to the value from numerical simulation

$$\langle K \rangle_{\text{area}} (0.27 \text{ Wcm}^{-2}) = 4.54 \cdot 10^{-13} \text{ m}^3 \text{ Hz/s}$$

for the most-weakly bound state. There is a strong disagreement between the measured and simulated rates. For the transition to the state in  $\nu' = -1; \Omega = 1$  the experimental data shows an overall lower value for the photoassociation rate where interestingly the factor between the measured und calculated loss rates is different to the state in  $\nu' = -1; \Omega = 0$ . At intensities close or lower than the calculated saturation intensity the numerical calculation overestimates the photoassociation losses by roughly the same

factor for each respective transition.

Towards low intensities the stimulated rate is small compared to the natural decay rate of the excited state i.e.  $\Gamma_{\text{stim}} \ll \gamma_1$ , the scattering matrix element in Eq. 2.4 can be simplified to

$$|S_{\text{inel}}|^2 \approx \frac{\gamma_1^2 l_{\text{opt}}(I) 2k_r}{[\epsilon_{\text{col}} - (\Delta + E_{\text{ls}})]^2 + \left(\frac{\gamma_1}{2}\right)^2}. \quad (4.6)$$

In this equation the optical length and consequently the scattering rate is proportional to the intensity. This expected linear growth of the rate with increasing intensity can be observed in the experimental spectra. Towards photoassociation intensities higher than the respective saturation value the theoretical calculations predict a decline in the increase of the integrated rate with an eventual saturation that cannot be seen in the data. There is no apparent reason for the strong discrepancy at low intensities but possible explanations e.g. that the intensity of the spectroscopy beam was misjudged will be treated in the next chapter in greater detail.

## 4.4 Investigation of intensity-induced line broadening

From the last section it became clear that there is strong disparity between measured and calculated absolute photoassociation rates. To get a more complete understanding of the process I have investigated the shape of the resonance i.e. the width of the atom loss spectra. This measurement is complementary to the previous results as the width does not depend on the volume of the atomic trap but only on the spectroscopic intensity, which makes it insensitive to uncertainties related to the modeling of the optical trap.

At low intensities one expects that the lineshape is mostly dominated by thermal effects of the cloud i.e. Doppler broadening induced by the center-of-mass motion of the atomic pair with respect to the incident laser beam driving the photoassociation transition and thermal broadening resulting from different collisional energies  $\epsilon_{\text{col}}$  of the atom pair. This collisional energy and the Doppler shift enter in the resonance denominator in Eq. 2.4 and change the frequency of the light required to resonantly excite a transition to a rovibrational state (see Sec. 2.4). Towards higher intensities the Lorentzian width of the photoassociation line  $\Gamma_{\text{stim}} + \gamma_1$  becomes more relevant to the final shape measured by the experiment. As the stimulated rate increases with higher

intensity the width of the photoassociation line at a fixed collision energy becomes comparable to the broadening effects induced by the thermal effects of the sample. In order to see an appreciable effect of power broadening the atom loss spectra  $N_{\text{atom}}(\Delta)$  were converted to spectra of the atom loss coefficient  $\beta(\Delta)$  that were subsequently fitted by a Gaussian to determine the FWHM. The results of this analysis together with the values determined from simulated photoassociation spectra are shown in Fig. 4.5.

In the graph one can see that for the  $v' = -1; \Omega = 0$  level the width starts to increase with rising photoassociation intensity in good agreement with the theoretical calculation. At the lowest intensities the measured width is in agreement with the calculated thermal broadening at a sample temperature  $T = 1.08 \mu\text{K}$  considering the uncertainty of 15 % of the temperature measurement indicated by the dash-dotted horizontal lines. The same is true for the  $v' = -1; \Omega = 1$  level and the corresponding sample temperature  $T = 0.8 \mu\text{K}$ . The expected combined thermal width  $\Gamma_{\text{therm}} + \Gamma_{\text{Doppler}}$  and the measured FWHM of the experimental data are in good agreement confirming the assumption of mostly temperature dominated spectral width at low photoassociation intensities. At the highest intensities an increase of the spectral width can be seen in the data. The measured width at high intensities reproduces the results of simulated spectra and is in good agreement with an average stimulated width  $\langle \Gamma_{\text{stim}} \rangle$  calculated directly from the Franck-Condon density. The coupling between the scattering and bound state is much smaller for the state in  $v' = -1; \Omega = 1$  which could explain why the broadening can not be seen as clearly as for the other bound state. Intensities above  $1000 \text{ Wcm}^{-2}$  would be needed to witness broadening comparable to the effects seen in the  $v' = -1; \Omega = 0$  line spectra.

## 4.5 Light shift: Experiment vs theory

The measurement of photoassociation spectra over a wide range of intensities also allows me to estimate the absolute shift of the lines by the AC-Stark effect. This also serves as a cross-check since the theoretical photoassociation lineshift is closely related to the Franck-Condon densities but is insensitive to the dipole trap geometry making the evaluation of this data less sensitive to experimental uncertainties compared to the analysis of the absolute rates. I used the center of a Gaussian fit to the loss spectra as the resonance position of the lines, neglecting that the actual resonance is slightly shifted from the center of the spectrum. This method is sufficient to determine the

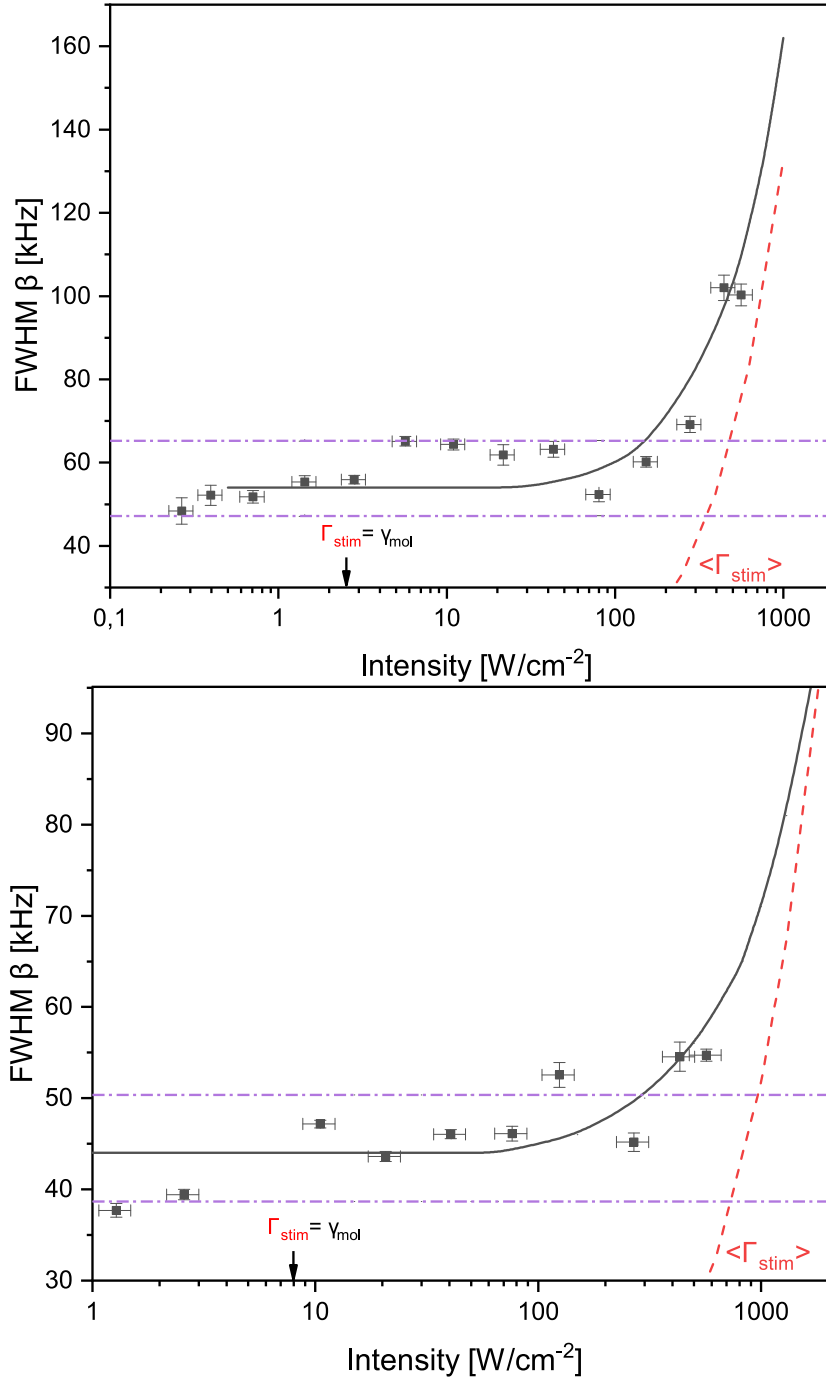


Figure 4.5: Comparison of the simulated and measured FWHM of the two photoassociation resonances (top)  $v' = -1; \Omega = 0$  and (bottom)  $v' = -1; \Omega = 1$ . For orientation the expected combined thermal and Doppler width  $\Gamma_{therm} + \Gamma_{Doppler}$  considering the temperature uncertainty (purple dashed-dotted lines) and the calculated stimulated rate  $\langle \Gamma_{stim} \rangle$  (red dashed line) are shown.

light shift as long as the neglected shift, which is on the order of a few kHz, remains constant during the course of the measurement. The results are shown in Fig. 4.6 for both measured molecular resonances. From a linear fit to the resonance position a shift of  $\frac{f_{\text{shift}}}{I_{\text{PA}}} = (-1.37 \pm 0.15) \cdot 10^{-4} \frac{\text{MHz}}{\text{W/cm}^2}$  and  $\frac{f_{\text{shift}}}{I_{\text{PA}}} = (-1.00 \pm 0.05) \cdot 10^{-4} \frac{\text{MHz}}{\text{W/cm}^2}$  for the  $v' = -1; \Omega = 0$  and  $v' = -1; \Omega = 1$  line was extracted.

I have compared these results to theoretical light shifts calculated from the same coupled-channel formalism that was employed to determine the Franck-Condon densities and the optical length that have been the basis of the simulations presented in this chapter. The theoretical light shift analogous to the Franck-Condon density is a function of the collision energy of the scattering atom pair and has been evaluated at the respective sample temperature as described in Eq. 2.5. The value of  $\frac{f_{\text{shift,CC}}}{I_{\text{PA}}} = -1.24 \cdot 10^{-3} \frac{\text{MHz}}{\text{W/cm}^2}$  was evaluated at a sample temperature of  $T = 1.08 \mu\text{K}$  and  $\frac{f_{\text{shift,CC}}}{I_{\text{PA}}} = -0.43 \cdot 10^{-3} \frac{\text{MHz}}{\text{W/cm}^2}$  at a temperature of  $T = 0.8 \mu\text{K}$  that correspond to the parameters during the respective measurement. Compared to the experimental measurement the calculated shift based on the coupled-channel wavefunctions is substantially bigger. The factors of  $\approx 9$  and  $\approx 4.3$  between calculation and experiment are not the same as the deviation in the case of the photoassociation rates though, which does not point towards a systematic misjudgement of the spectroscopic intensity considering that the power broadening was reproduced correctly.



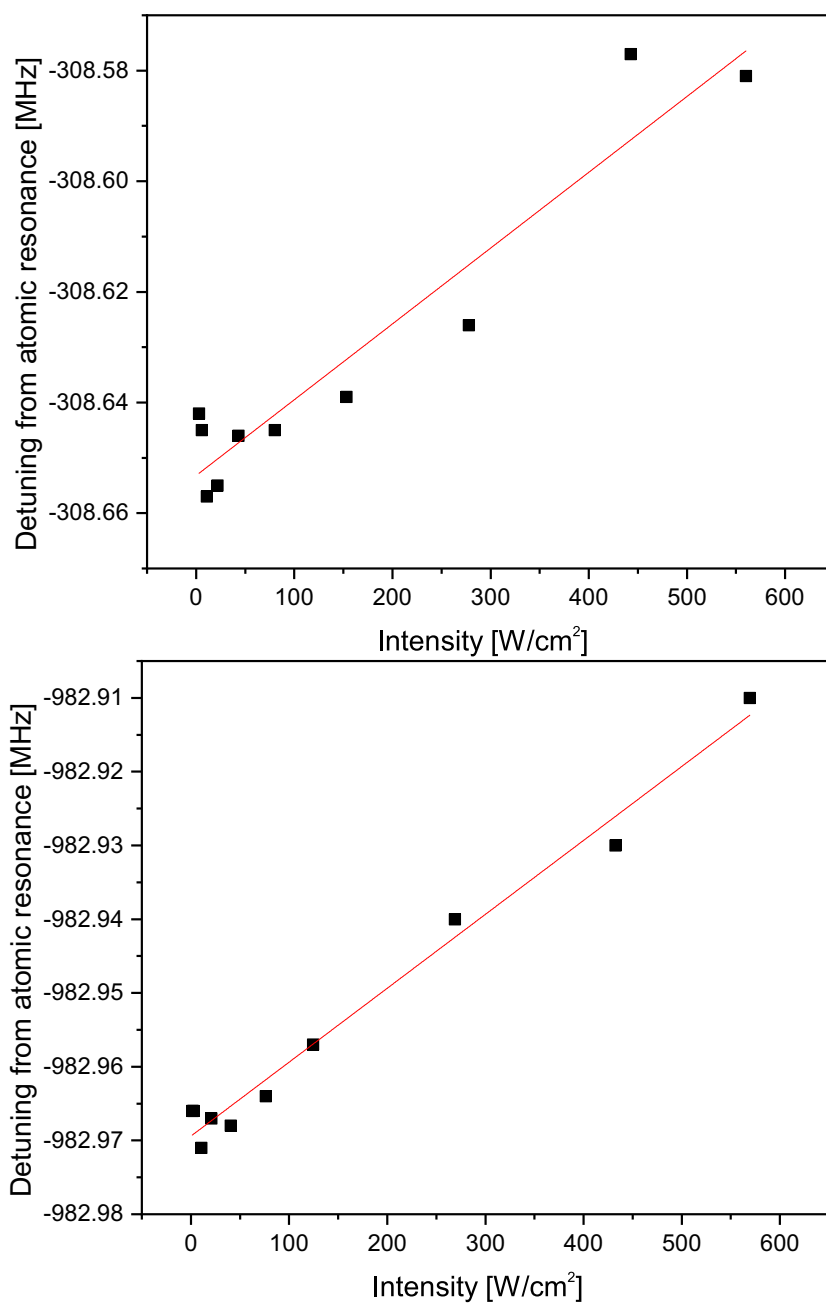


Figure 4.6: Measured shift of the center of a Gaussian fit with respect to the atomic asymptote to the measured atom loss spectra for the molecular resonance  $v' = -1; \Omega = 0$  ( $v' = -1; \Omega = 1$ ) depending on the used photoassociation intensity in the top (bottom).



# Chapter 5

## Discussion of previously unconsidered effects

The experimental results presented in the previous chapter rely on the validity theoretical approximations and on the experimental conditions as described in chapter 3 which are partly based on the description given in previous works. Not all parameters of the experimental setup can be validated directly which is why the influence of some of the approximations made and of limits to the experimental parameters from auxiliary measurements will be discussed here. The chapter can be viewed as a systematic analysis by the variation of key experimental parameters and their influence on the predicted photoassociation resonances.

### 5.1 Collision-energy dependent Franck-Condon density

At low temperatures of a few  $\mu\text{K}$  of the atomic samples studied in the experiment usually the Wigner threshold law, i.e. that the Franck-Condon density is proportional to the square root of the collision energy  $\epsilon_{\text{col}}$  is assumed when calculating theoretical lineshapes. The precise molecular potentials obtained from previous measurements of the exact binding energies of the most-weakly bound molecular states allowed us to include the real energy dependence in the simulation. The collision energy dependence of  $\Gamma_{\text{stim}}$  can potentially influence both the width and peak of the atom loss spectra which is why I have compared the results from simulations assuming the Wigner threshold law to spectra that have been calculated using the real energy dependence of the Franck-Condon density. This has been implemented into the simulation by substituting the calculation of the stimulated rate that is originally assumed to be proportional to the optical length as described in Eq. 2.10 by the exact Franck-Condon density derived from the scattering and molecular wavefunctions. Fig 5.1 shows the stimulated rate  $\Gamma_{\text{stim}}$  calculated from the optical length by application of the Wigner threshold law and based on the Franck-Condon density for a transition to the  $v' = -1; \Omega = 0$  state

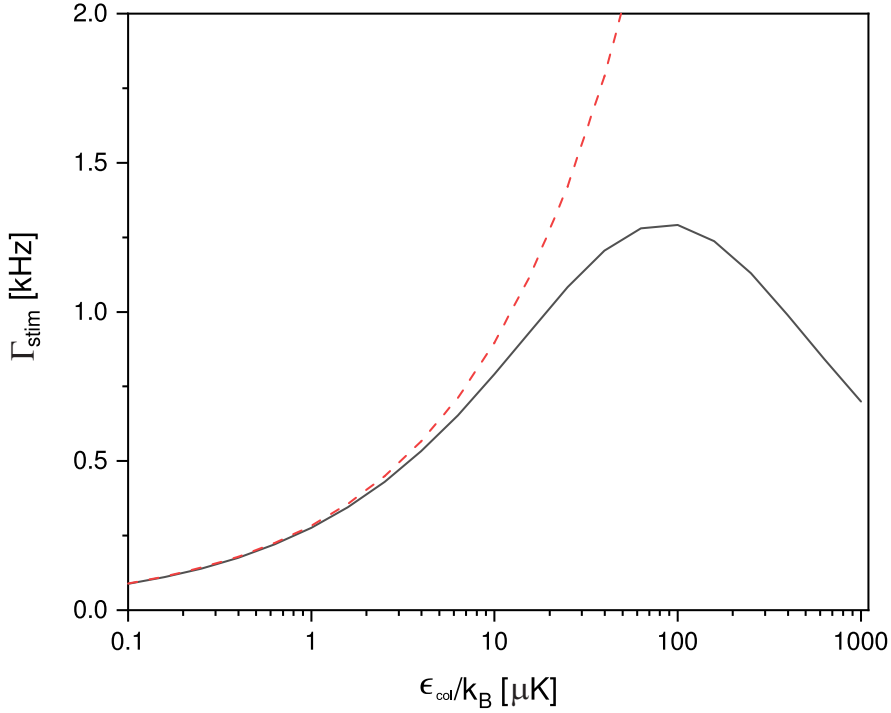


Figure 5.1: Stimulated rate  $\Gamma_{\text{stim}}$  as a function of the collision energy calculated from an optical length (dashed red line) and the Franck-Condon density from coupled-channel calculation (black solid line) at an intensity of  $1 \text{ Wcm}^{-2}$ .

assuming an intensity of  $1 \text{ Wcm}^{-2}$ . While there is a good agreement at the lowest collision energies the approximation tends to overestimate the coupling of the scattering and bound states at higher energies.

A comparison of the simulated integrated rate between the Franck-Condon density relying on the wavefunctions and Wigner threshold law approach is shown in Fig. 5.2. As can be seen from the graph the rates towards low intensity are reduced by  $\approx 10\%$  probably related to the fact that the Franck-Condon density peaks around collision energies corresponding to a temperature of  $100 \mu\text{K}$  while the approximation by the Wigner threshold law is monotonously growing for increasing collision energy.

Thus the exact Franck-Condon density has only minor influence on the results for the integrated rate and is not sufficient to explain the discrepancies seen between the simulated and measured data. This shows that the assumed Wigner threshold law is applicable in the investigated case.

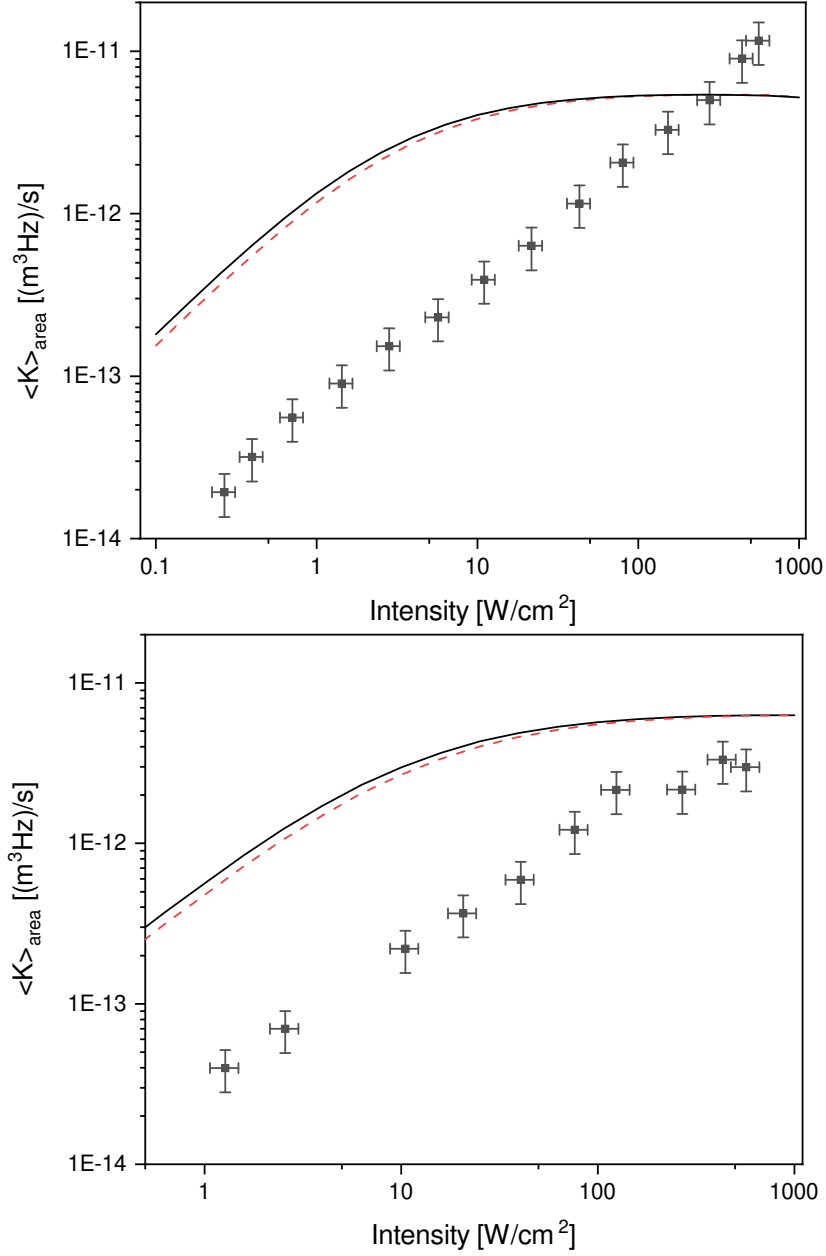


Figure 5.2: Integrated photoassociation loss factor  $\langle K_{\text{area}} \rangle$  deduced from the measured atomic losses for different photoassociation intensities. The top graph shows the values for the  $\nu' = -1; \Omega = 0$  state and the bottom graph shows the values for the  $\nu' = -1; \Omega = 1$  state. The solid grey line indicates the integrated rate from simulated spectra using the formalism of Bohn and Julienne assuming a fixed optical length and the Wigner-threshold law while the red dashed line shows a calculation using the exact dependency of the Franck-Condon density from the collision energy  $\epsilon$ .

## 5.2 Influence of atom recapture by the dipole trap

During the evaluation of the experimental rates I assumed that all photoassociated molecules either decay back to ground state atoms that are subsequently lost from the optical dipole trap or to ground state molecules that can no longer be detected by absorption imaging due to the molecules being transparent to the absorption imaging at 423 nm. Since the measured rates are substantially lower than predicted from numerical calculations I considered the possibility that a relevant fraction of dissociated atoms had sufficiently low kinetic energy that they were recaptured by the dipole trap. To exclude unconsidered recapture by the trap I studied the photoassociation rates at different trap depths. If substantial recapture was the cause of the reduced photoassociation rates seen in the measurement, performing the experiment with a deeper optical trap one would expect a higher fraction of recaptured atoms that should further reduce the measured rates. In the experimental setup the trap depth is strongly correlated to different sample temperatures which complicates the comparison of the experimental  $\langle K_{\text{area}} \rangle$  with the theory since it predicts a variation of the photoassociation rate with the sample temperature. During the calculation of the predicted rate there are two separate effects that have to be considered. Firstly, the distribution of collision energies  $\epsilon_{\text{col}}$  is directly correlated to the sample temperature which leads to an increased median shift in the denominator of Eq. 2.4 and also introduces a bigger Doppler broadening due to the broader velocity distribution of the atom pairs with respect to the direction of the spectroscopy laser. Furthermore, the temperature enters into the normalization of  $\langle K \rangle$  in the form of the translational partition function  $Q_t$  when thermally averaging over the sample leading to decreasing rates at higher temperatures.

Secondly, different sample temperatures are achieved by different evaporation ramps of the optical dipole trap and with that varying final power in the dipole trap beams. As a result a change of the trap depth changes not only the sample temperature but also the dipole trap volume which has to be considered when evaluating the photoassociation lines.

For both molecular states under investigation a series of measurements at different sample temperatures, i.e. trap depths, at the highest spectroscopic intensity were recorded to determine whether an appreciable fraction of atom is recaptured. Additionally, another set of measurements at much lower intensities was studied to separate effects introduced by the increased power broadening of the lines.

The atomic loss factor  $\beta$  depending on the detuning from the threshold are shown

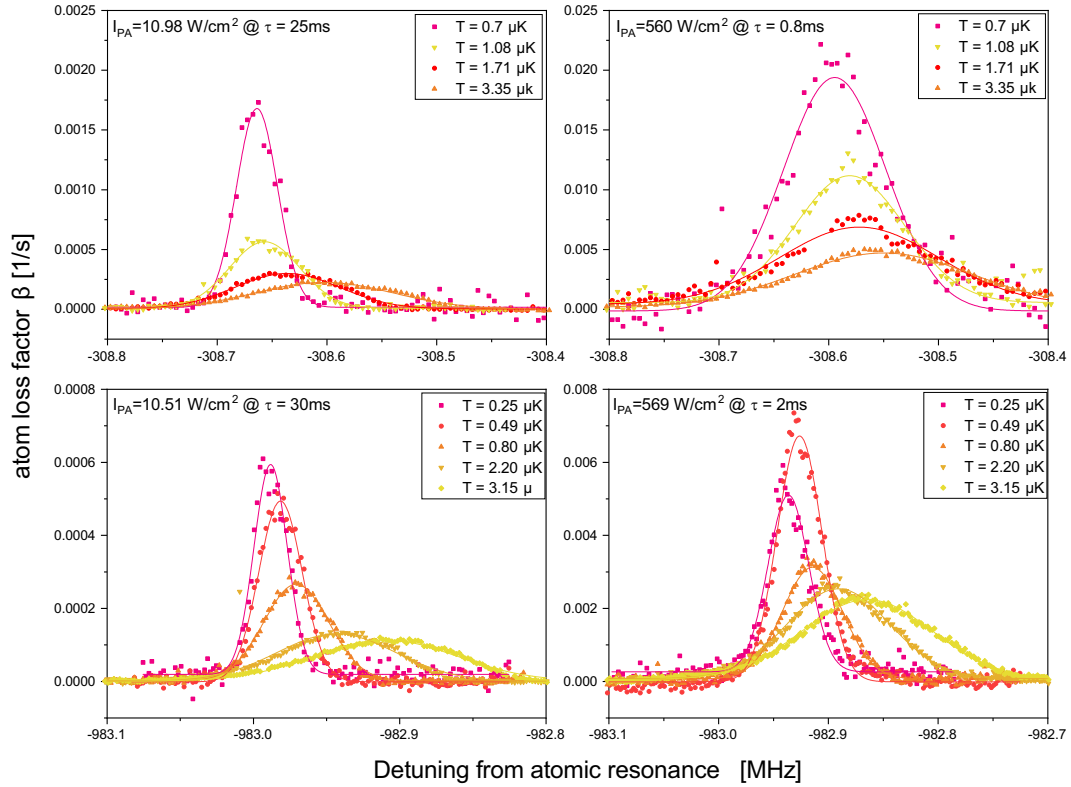


Figure 5.3: The atomic loss factor  $\beta$  as a function of the detuning from the threshold for the  $v' = -1; \Omega = 0$  resonance at photoassociation intensities of  $I_{PA} = 10.98$  and  $560 \text{ W/cm}^2$  and the  $v' = -1; \Omega = 1$  resonance at photoassociation intensities of  $I_{PA} = 10.51$  and  $569 \text{ W/cm}^2$  for different sample temperatures.

$I_{\text{hor}}$ [mW]	$I_{\text{tilt}}$ [mW]	$T_{\text{sample}}$ [ $\mu\text{K}$ ]	$U_0/k_B$ [ $\mu\text{K}$ ]	$V_{\text{DT}}$ [ $10^{-14}\text{m}^3$ ]
$\nu' = -1; \Omega = 0$				
0.4	0.9	0.7	26.1	0.56
0.6	1.2	1.08	36.4	0.62
0.9	1.8	1.71	54.6	0.67
1.2	2.0	3.35	65.7	1.31
$\nu' = -1; \Omega = 1$				
0.1	0.2	0.25	6.1	1.01
0.15	0.5	0.45	13.9	1.15
0.25	1.0	0.8	24.1	1.00
0.5	2.0	2.2	48.2	1.62
0.8	2.5	3.15	64.6	1.57

Table 5.1: Dipole trap beam power  $I_{\text{hor}}$  and  $I_{\text{tilt}}$ , the corresponding time-of-flight temperature  $T_{\text{sample}}$ , trap depth  $U_0/k_B$  and the volume of the trapping region  $V_{\text{DT}}$ .

in Fig. 5.3 for the  $\nu' = -1; \Omega = 0$  resonance at photoassociation intensities of  $I_{\text{PA}} = 10.98$  and  $560 \text{ W/cm}^2$  and the  $\nu' = -1; \Omega = 1$  resonance at photoassociation intensities of  $I_{\text{PA}} = 10.51$  and  $569 \text{ W/cm}^2$  to give an indication of the influence of different sample temperatures (the corresponding dipole trap power and trap depth are given in Tab. 5.1) during the measurement. The center of the line is shifted to lower frequencies at higher temperatures as a consequence of averaging over a different energy distribution and the AC-Stark effect of the varying dipole trap intensity. The width of the resonance also increases mainly related to thermal broadening of the line. This is also a good illustration for why it is useful to look at the integrated loss rate rather than the maximum value since in theory it should be insensitive to thermal broadening.

The dipole trap power, the time-of-flight temperature of the sample, the maximum trap depth and the calculated dipole trap volume used to evaluate the spectra are shown in Tab. 5.1. If the temperature is a fixed fraction of the trap depth, then the dipole trap volume would be independent of trap depth. Towards deeper traps and higher temperatures however the otherwise almost constant trap volume shows an increase which might be related to insufficient thermalization of the sample. The photoassociation rates depending on the temperature are visualized in Fig. 5.4 together with theoretically calculated values for comparison. As seen in the earlier evaluation



there is a substantial disparity between the absolute value of the measured and calculated rates which is the reason I have chosen a logarithmic scale for this comparison. Nevertheless, towards lower temperatures the measured rates seem to reproduce the increase predicted by the simulation although the spread of the experimental values makes it difficult to make a clear distinction. For the highest investigated temperature the results are inconclusive which might be related to the irregularities seen in the dipole trap volumes discussed before. Overall the results do not point towards a

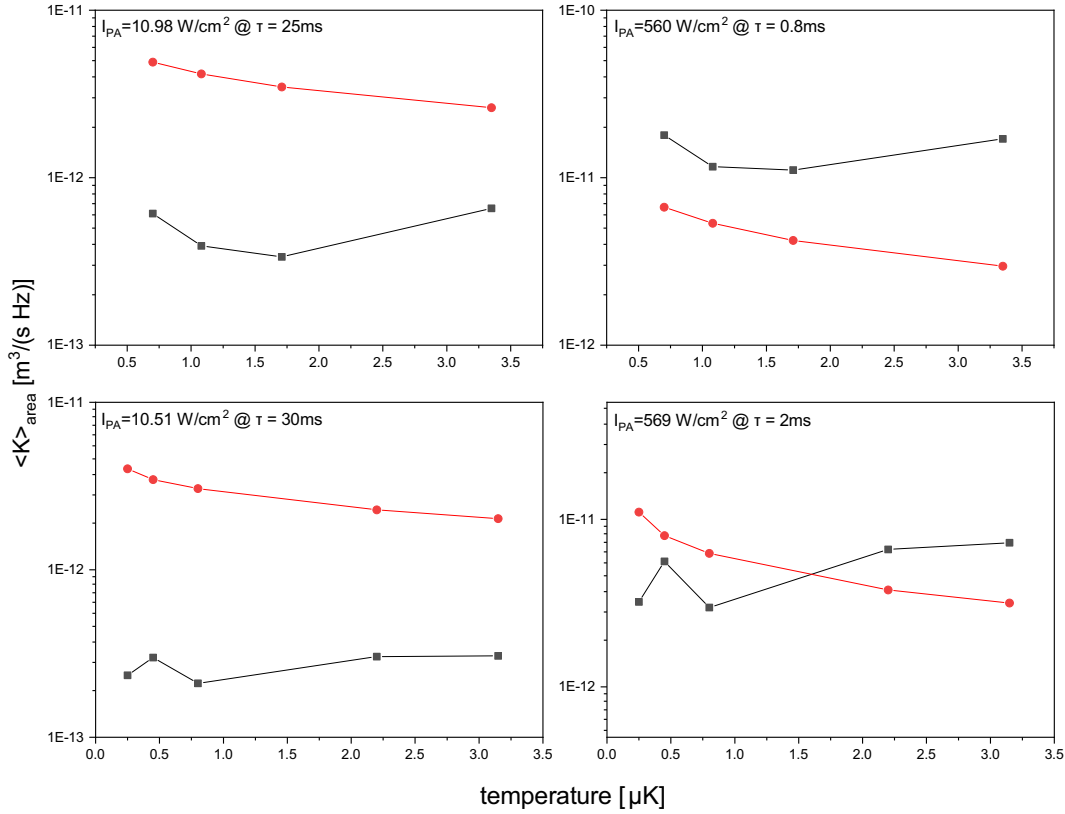


Figure 5.4: Integrated photoassociation loss factor  $\langle K_{\text{area}} \rangle$  as a function of the sample temperature for the  $v' = -1; \Omega = 0$  resonance at photoassociation intensities of  $I_{\text{PA}} = 10.98$  and  $560 \text{ W/cm}^2$  and the  $v' = -1; \Omega = 1$  resonance at photoassociation intensities of  $I_{\text{PA}} = 10.51$  and  $569 \text{ W/cm}^2$ . The black squares and red dots symbolize the experimental data and the simulation, respectively.

substantially increased recapture of dissociated atoms for deeper optical dipole traps. This is also in agreement with the theoretical prediction, that the energy distribution of the molecular decay products corresponds to the Franck-Condon density and can be viewed as a reversed photoassociation process. As already shown in chapter 2, the Franck-Condon density (Fig. 2.2) peaks around energies corresponding to  $100 \mu\text{K}$

which is higher than the trap depth  $U_0 = \frac{\alpha I_{\text{DT}}}{k_{\text{B}} w^2 \epsilon_0 c} \approx 30 \mu\text{K}$  at which the measurements were performed. More importantly only a fraction of the excited molecules actually decays back to the atomic continuum while most of them decay to bound states in the ground state potential [Pac17].

### 5.3 Alignment of spectroscopy beam

A second possible modification of the simulation I have studied is the effect of a misalignment between the spectroscopy beam and the atomic cloud resulting in a reduced photoassociation intensity  $I_{\text{PA}}$ . Should the center of the Gaussian intensity distribution of the spectroscopy beam and the center of the optical trap not be aligned as well as described in section 3.2.2 the effective intensity illuminating the ultra-cold ensemble can be significantly lower than assumed. This could for example be the case if we accidentally align a reflected part of the photoassociation beam with the atomic cloud. This is not very likely but is still a possibility worth to investigate. In order to bring the measured and simulated integrated rates far from saturation shown in Sec. 4.1 into agreement the effective intensity needs to be reduced by a factor of 19 for the  $v' = -1; \Omega = 0$  state and by a factor of 16 for the  $v' = -1; \Omega = 1$  state. One would expect that for a simple misalignment of the beam the factor needed would be the same for both measured lines.

Measurements of the Autler-Townes splitting [Aut55, Pac17] of the bound-bound molecular transitions can be used to further investigate a possible misalignment of the spectroscopy beam since the alignment procedure of the beams was the same as described in Sec. 3.2.2. The experiment utilized the same optical setup as described before with the addition of a second photoassociation beam that was coupled into the same fiber the original beam used. The second spectroscopy beam uses a similar offset locking scheme as described for the one color photoassociation setup (Sec. 3.2.1. In order to observe an Autler-Townes doublet the second beam with intensity  $I_{\text{AT}}$  operates at a frequency  $\omega_{\text{AT}}$  that is resonant to a transition between an excited molecular state and a molecular state in the ground state potential  $X^1\Sigma_g^+$ . The setup of the laser frequencies is schematically shown in Fig. 5.5. For this measurement the excited state  $v = 39, J = 0$  with a binding energy  $\Delta_{\text{bind}}/(2\pi) = 1387.442(9)\text{MHz}$  [Pac17] was chosen. The resonance splits into an Autler-Townes doublet due to an avoided crossing in the dressed state system of the two molecular states coupled by the resonant light field. Scanning the original photoassociation laser across this excited molecular state

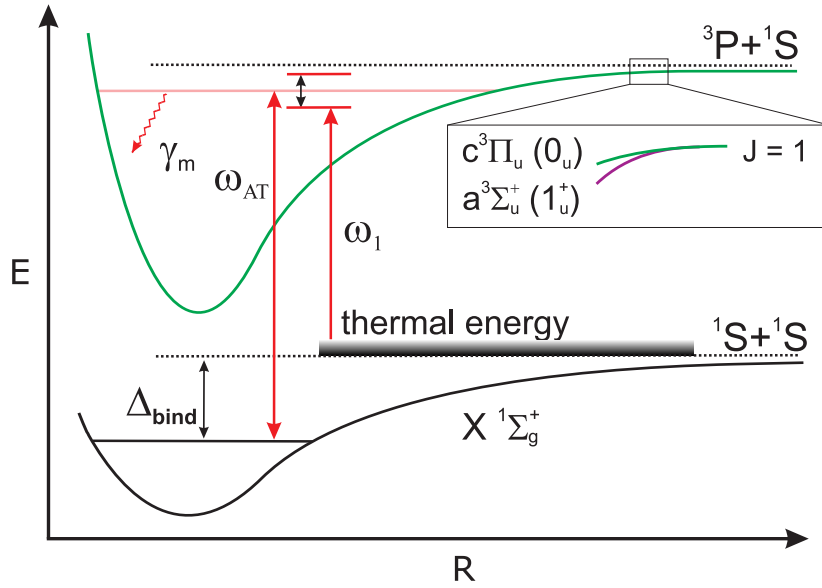


Figure 5.5: Schematic drawing of the laser setup for measuring the Autler-Townes splitting. The laser with frequency  $\omega_{AT}$  is resonant between a molecular state in the ground state potential  $X^1\Sigma_g^+$  and an excited state in the potentials dissociating to the  ${}^3P_1+{}^1S_0$  asymptote while the laser with frequency  $\omega_1$  is scanned in the vicinity of the bound state in the excited potential.

while keeping the second laser resonant to the transition between the bound states there are not one but two resonance features that are separated by the Rabi frequency  $\Omega_{12}$  that depends on the intensity  $I_{AT}$  as [Esc08, Pac17]:

$$\begin{aligned}\Omega_{12} &= \frac{1}{\hbar} \langle 1 | V_{opt}^{AT} | 2 \rangle \\ &= \sqrt{f_{ROT}} \sqrt{f_{FCF}} \sqrt{\gamma_{atom}} \sqrt{I_{AT} \frac{6c^2\pi}{\omega^3\hbar}}.\end{aligned}\quad (5.1)$$

The experimental signature scanning across the least bound state in the excited potential ( $a, c$ ) $1_u$ <sup>1</sup> is shown in Fig. 5.6 for different intensities of the Autler-Townes laser that couples the two bound molecular states. The individual peaks have been fitted by Gaussian functions and the distance in optical frequency between their respective center, i.e. the Rabi splitting, has been determined from the graph. The result of this analysis is shown in Fig. 5.6.

Also shown in the graph is the theoretically expected Rabi splitting derived from theoretical calculations. For the transition between the two states I assumed the Franck-Condon factor  $f_{FCF} = 0.531$  calculated from the overlap between the two molecular

<sup>1</sup>which is identical to one of the states investigated in the the earlier sections of this work

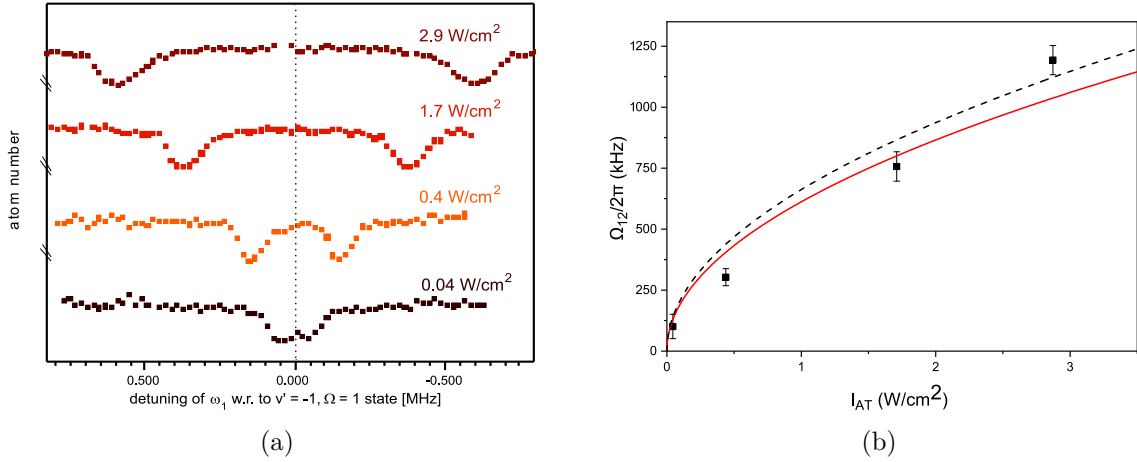


Figure 5.6: Graph (a) shows the atom loss as a function of the detuning from the bound state  $v' = -1; \Omega = 1$  for different intensities  $I_{AT}$  of the Autler-Townes laser. In graph (b) the Rabi-splitting of the Autler-Townes doublet (black squares) over  $I_{AT}$  is fitted to Eq. 5.1 (solid red line) and compared to a calculation using Franck-Condon factors (dashed black line).

wave functions in the coupled-channel model. This is similar to the determination of the Franck-Condon density but instead of calculating the overlap with the scattering wavefunction at different collision energies  $\epsilon_{col}$  this time the squared integral with a bound state ground state wavefunction determines a single Franck-Condon factor. The rotational factor was determined from angular momentum algebra and it is  $f_{ROT} = 2$  for a transition between  $J = 1 \rightarrow J = 0$  in the case described here [Edm57]. From a fit of Eq. 5.1 to the data points an experimental value for the Franck-Condon factor was determined to  $f_{FCF} = 0.45(9)$  which is in agreement with the coupled-channel calculation indicating that the beams are aligned correctly and the intensity is indeed what I initially assumed.

## 5.4 Energy dependence of the PA light shift

Until now I have neglected the light shift that is induced by the photoassociation laser itself during the numerical calculations of the line shapes and rates. Since it is possible to directly calculate the theoretical lightshift from the scattering and bound state wavefunctions I have studied the effect of the shift on the simulated line and whether including the shift improves the agreement with the measurement. The shift  $E_{ls}$  in Eq. 2.5 has been calculated from solutions of the Schroedinger equation incorporating the precise molecular potentials that have been determined in earlier studies [Kah14b]

of the binding energies of the rovibrational states [Boh99]. The shift depends on the energy of the colliding atom pair similar to the Franck-Condon density. As such it also has to be considered when averaging over the thermal energy distribution of the atoms in the dipole trap which could potentially lead to a modification of the resonance shape. The simulation has been modified in order to account for this effect by inclusion of an additional term that alters the resonance condition in Eq. 2.4 in dependence of both the intensity of the photoassociation light and the collision energy of the involved atom pair.

The intensity-normalized shift as a function of the collision energy is shown in Fig. 5.7<sup>2</sup>. According to the calculations the shift only weakly depends on the collision energies below 10  $\mu\text{K}$ . This behavior changes towards higher collision energies which could lead to an appreciable effect on the shape of the resonance. Nevertheless as it is an inhomogeneous broadening effect it should have no effect on the integrated rate. The effect on the shape of the simulated line-profile at high intensities is shown in Fig. 5.8.

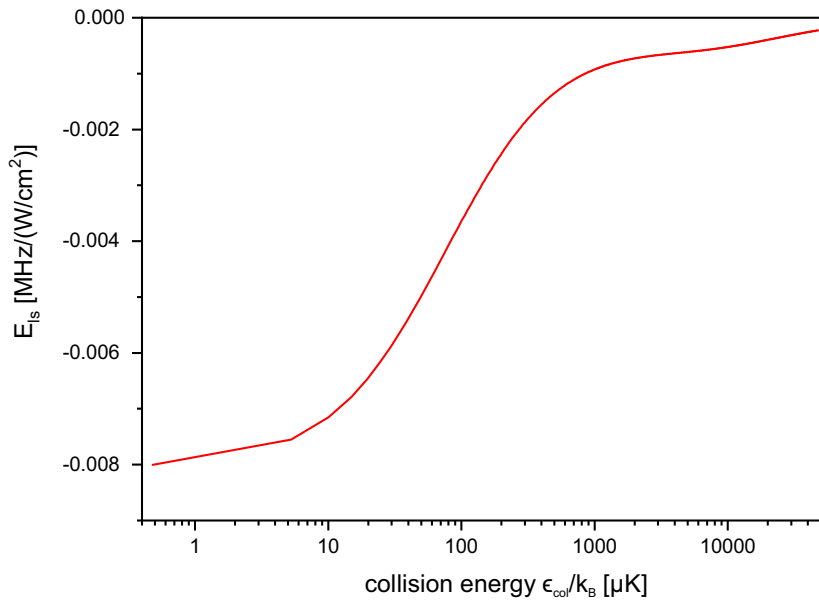


Figure 5.7: Theoretical calculation of the light shift induced by the photoassociation laser according to Eq. 2.5. Courtesy of E. Tiemann.

The line is basically unaltered except for an absolute shift of the center of the resonance that was compensated in the graph i.e. the center of the simulated resonances with and without considering the light shift are both centered at the measured resonance frequency. The peak rate is reduced by less than 10% while the width increases by

<sup>2</sup>the calculation of the wavefunctions has been performed by Prof. Dr. E. Tiemann

about 4 kHz (see Fig. 5.8) for the highest intensity of  $I_{\text{PA}} = 560 \text{ Wcm}^{-2}$  measured in the experiment. At lower intensity the broadening becomes less pronounced and at the lowest intensity the spectra are basically unaltered compared to the simulation not considering the light shift induced by the photoassociation laser. Furthermore the integrated rates show no deviation to the simulation without this light shift as is expected. Obviously this can also not explain the disagreement I have seen but it is

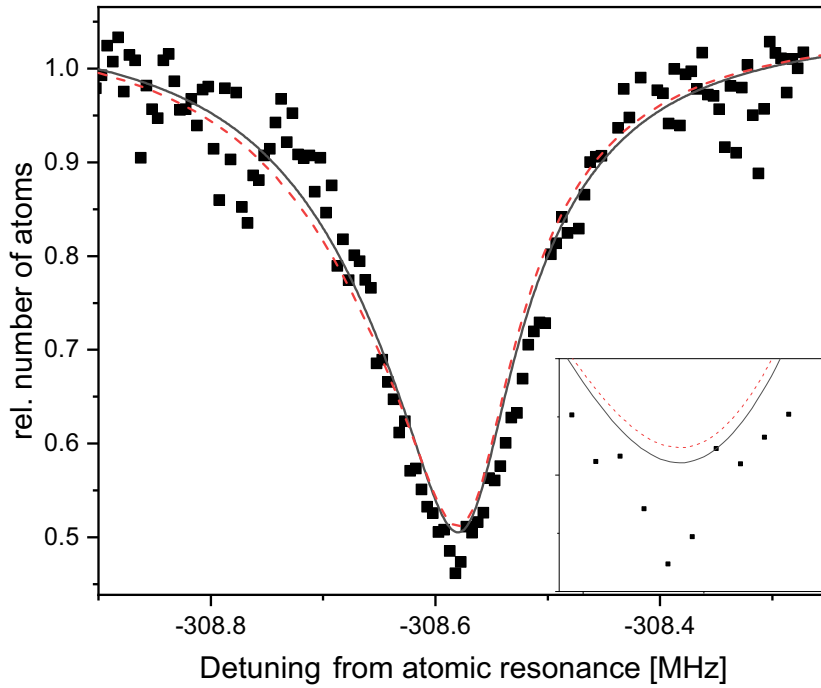


Figure 5.8: The measured data (black squares) together with a comparison between the simulated atom loss including the light shift in the calculation (dashed red line) and not considering the light shift (solid grey line) at a photoassociation intensity of  $560.23 \text{ Wcm}^{-2}$  for the  $v' = -1; \Omega = 0$  state. Also shown are the measured data.

still an interesting broadening mechanism that especially at higher intensity has to be considered when photoassociation lines are modeled.

## 5.5 Influence of the duration photoassociation illumination

During the measurements I have generally tried to limit the maximal losses from the dipole trap to less than half of the initial atoms by adjusting the duration the atoms are illuminated by the spectroscopy light at each intensity. As a result a wide variety of

illumination durations from below 1 ms up to 100 ms were used at different intensities. To exclude a dependency of the derived photoassociation rate from the varying photoassociation time  $\tau_{\text{PA}}$  I have recorded photoassociation spectra at the same spectroscopic intensity but with different photoassociation times. The graph in Fig. 5.9 shows the atomic loss factor  $\beta$  scanning the photoassociation laser across the molecular state in  $v' = -1; \Omega = 1$  at an intensity of  $I_{\text{PA}} = 10.51 \text{ Wcm}^{-2}$  for multiple different times  $\tau_{\text{PA}}$ . The spectra for the different photoassociation times are almost identical even for the shortest time of 12 ms where roughly 40 % of the atoms were lost due to photoassociation at the peak of the resonance compared to the almost 70 % at 75 ms. The atomic loss spectrum is even visibly flattened at its center due to the high losses. Evidently the derived loss factor does not depend on the variation of this experimental parameter in the low intensity regime. At several other intensities and also using the other molecular state in the  $v' = -1; \Omega = 0$  potential the experimental measurements indicate a similar behavior at high intensities. From all parameter combinations that have been investigated the photoassociation rate deviated by at most 15 % for a variation of  $\tau_{\text{PA}}$ . This small variation might be explained by the low number of atoms remaining in the trap at high intensity and longer spectroscopy times making the measurement more susceptible to perturbations at the center of the resonance. Overall the assumption that the Gaussian density distribution in the optical trap is not significantly changed by the induced losses is justified based on these observations. Furthermore the applied transformation from density related to atom number related loss factor is valid and the choice of photoassociation time  $\tau_{\text{PA}}$  has no impact on the inferred rates.

## 5.6 Extension of the atomic cloud

In the presented simulations I have assumed that the photoassociation intensity experienced by the atoms is uniform across the trap and furthermore corresponds to the peak intensity of the Gaussian spectroscopy beam. This is of course only a reasonable approximation if the size of the atomic sample is substantially smaller than the profile of the photoassociation beam. In this section I will investigate how considering the extension of the trap during the numerical calculations changes the expected spectra. Depending on the axial direction the atomic cloud has an extension of up to a few 10  $\mu\text{m}$ . It is overlapped with the photoassociation beam with a waist radius of  $w_0 = 50(3) \mu\text{m}$ . The analysis of the experimental data focuses only on the total number of atoms in the trap while the photoassociation rate actually effects the local

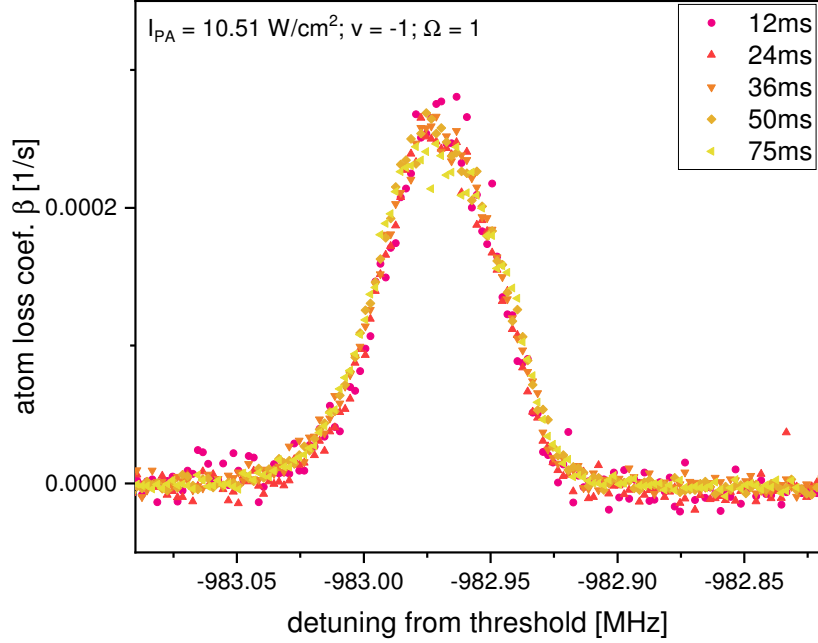


Figure 5.9: Derived atomic loss coefficient  $\beta$  as a function from the detuning from threshold for the molecular state in  $v' = -1; \Omega = 1$  for different photoassociation times  $\tau_{\text{PA}}$ . For the earlier evaluation the spectrum belonging to  $\tau_{\text{PA}} = 50$  ms has been used.

density instead. Considering a section of atomic cloud towards the edge of the trapping volume the local intensity of the dipole trap is naturally lower than in the center in addition to the reduced local density.

The model that was applied during the analysis of the data in Chapter 4 assumed that the entire atom sample that follows a Gaussian density distribution experiences the peak intensity of the Gaussian spectroscopy beam. This is of course only a reasonable approximation if the extension of the dipole trap is small compared to the waist of the spectroscopy beam. The experimental situation as described in chapter 3 is that the extension of the cloud at least in the direction along the horizontal trapping beam might not be negligible for the calculation of the photoassociation rates. The RMS radii  $\sigma_i$  of the trap can be calculated from the harmonic frequencies  $\omega_i$  by [Gri00]:

$$\sigma_i = \omega_i^{-1} \sqrt{\frac{k_B T}{m_{\text{Ca}}}}. \quad (5.2)$$

For the experimental parameters used during most of the measurements this results in a trap extension of  $\approx 5 \mu\text{m}$  in the radial direction and  $\approx 21 \mu\text{m}$  in the axial direction. To confirm whether the assumption made concerning the intensity is justified I have



considered the extension of the atomic cloud in three directions. First the absorption of the spectroscopy beam along its propagation direction through the trap parallel to one of the radial direction. This should have no significant influence since due to the small linewidth of the triplet transition only a negligible fraction of light is being absorbed by the atoms. Since the Rayleigh length of the photoassociation beam  $z_R = 3.3$  mm is orders of magnitudes larger than to the extension of the cloud it is reasonable to assume that the intensity of the Gaussian beam along its path remains approximately constant in the vicinity of the atoms.

The extension in the other radial direction (perpendicular to both the horizontal trap beam and the spectroscopy beam) can also be neglected since again the photoassociation beamwaist of  $50 \mu\text{m}$  is large compared to the extension in this direction. Lastly the axial extension of the trap has to be considered. The RMS radius of  $21 \mu\text{m}$  is about half the width of the spectroscopy beam which leads to reduction of  $\approx 30\%$  intensity at the edge of the trap which will lead to a reduction of the total rate.

I have estimated the impact of the reduced intensity acting on the local density inside the dipole trap by including the varying local intensity in the simulation. Two different approaches were used. First by calculating an average intensity across the distribution of atoms by simply integrating the intensity profile of the beam over the density distribution of the atomic sample in axial direction. This leads to a reduction of the effective intensity depending on the dimension, i.e. the volume, of the dipole trap. For an RMS radius of  $\sigma_{\text{axial}} = 21 \mu\text{m}$  the average intensity is reduced by 23% compared to the peak intensity at the center of the spectroscopy beam.

In a different approach both the local density and the Gaussian nature of the spectroscopy beam were considered by calculating an effective loss coefficient  $K_{\text{eff}}$  according to

$$K_{\text{eff}} = \frac{\int K(I(z))\rho(z)^2 dz}{\int \rho(z)^2 dz}, \quad (5.3)$$

taking into account that the loss factor acts upon the squared local density.

The result is shown in Fig. 5.10. The effect on the integrated rates is less than a few ten percent for either of the two methods and is as such not suitable to explain the massive disagreement between the measured and calculated rates assuming an axial extension of the cloud of  $21 \mu\text{m}$ .

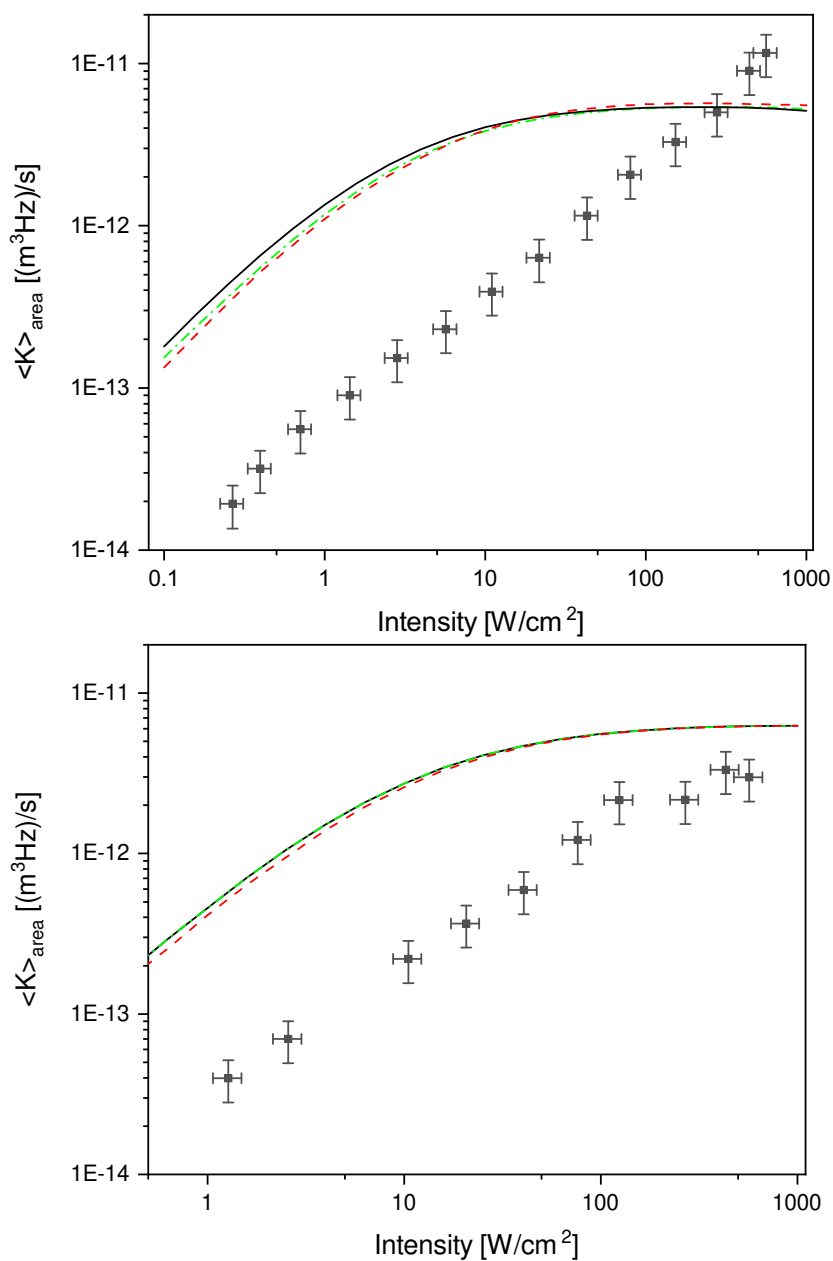


Figure 5.10: Integrated photoassociation rates considering the extension and thermal character of the atomic cloud and the Gaussian shaped extension of the spectroscopy beam. Shown are the results neglecting this effect (solid black line), considering it by integrating across the trapping volume (red dashed line) and by calculating an effective intensity the atoms see during the spectroscopy (green dash dotted line).

## 5.7 Effect of misaligned dipole trap beams

As stated before, the description of the experimental parameters of the dipole trap relies on the earlier documentation of the setup because some of the parameters can not be measured directly. Until now the data has been analyzed assuming that the two trapping beams perfectly overlap at the center of their respective Gaussian intensity distribution. Further the two beams do not intersect at their respective waist position but instead the tilted beam is deliberately shifted away from this position by 4.5 mm. That means that the tilted beam has widened to  $\approx 76 \mu\text{m}$  when it meets the horizontal beam. In this configuration a more efficient evaporation cooling can be achieved due to the otherwise substantial three-body losses being suppressed [App13, Kra09]. As described in the section before under these circumstances the trap has a axial extension of roughly  $\approx 21 \mu\text{m}$ . Should the beam have been shifted differently from the assumed 4.5 mm at some point during the adjustment of the dipole traps the trap geometry is altered which has direct implications on the trapping volume that is important when comparing the simulated and measured spectra. Additionally, an increasing trap size also decreases the effective intensity the atom pairs experience leading to further reduced rates as described in the last section. A direct measurement of the dipole trap size is not possible with the optical resolution in the current experimental setup.

Nevertheless, I have estimated the size of the atomic ensemble trapped in the crossed dipole trap from absorption images taken shortly after release. Assuming a thermal distribution of atoms in the cloud one can determine the initial dimensions of the trap by subtracting the expansion after release from the dipole trapping field. I have chosen parameters similar to the conditions used during the photoassociation measurements, i.e. a temperature of  $T = 1.08 \mu\text{K}$  and intensities of 0.6 W and 1.2 W in the horizontal and tilted trap beams, respectively. Such an absorption image of the trap after an expansion time of  $t_{\text{exp}} = 1.5 \text{ ms}$  together with a horizontal and vertical cut through the center of the density distribution of the cloud are shown in Fig. 5.11. From a fit to the density distribution along the horizontal cut an axial RMS radius of the cloud of  $\sigma_{\text{axial}} = 41.9 \mu\text{m}$  after expansion was determined. The cut in the vertical direction provides information about the extension in one of the radial directions i.e.  $\sigma_{\text{rad}} = 29.7 \mu\text{m}$ . These values take into account that the absorption imaging is not perpendicular to the axial direction of the cloud but rather views the cloud under an angle of  $20^\circ$ . Under this angle the axial dimension of the cloud appear slightly shorter than it really is. After being released from the trap the atoms freely evolve according

to their kinetic energy, i.e. the sample temperature  $T$ , and expand by

$$\sigma_{\text{exp}} = \sqrt{\frac{k_B T}{m} t_{\text{exp}}^2} \approx 22.5 \mu\text{m}. \quad (5.4)$$

Using this information one can estimate the initial size from the quadratic sum of the RMS radii as

$$\sigma_{\text{total}} = \sqrt{\sigma_{\text{ini}}^2 + \sigma_{\text{exp}}^2}. \quad (5.5)$$

From the atom cloud size after expansion the initial RMS radii in the direction along the horizontal dipole trap beam and the direction perpendicular to that beam were determined to be  $\sigma_{\text{axial,abs}} = (31 \pm 6) \mu\text{m}$  and  $\sigma_{\text{rad,abs}} = (15 \pm 7) \mu\text{m}$ , respectively. These values are bigger than the calculation from the beam waists of the dipole trap would suggest ( $\sigma_{\text{hor}} = 21 \mu\text{m}$ ,  $\sigma_{\text{rad}} = 4.4 \mu\text{m}$ ). This is most likely related to the limited resolution of the optical imaging.

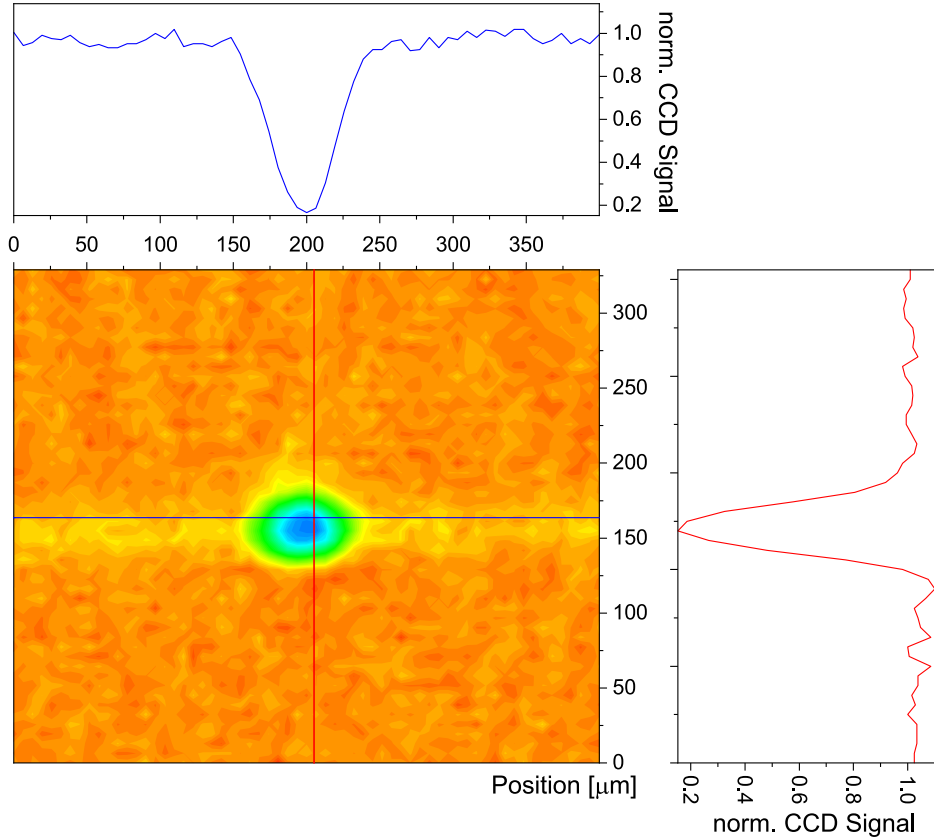


Figure 5.11: Absorption image of a typical atomic cloud after expansion time of  $t_{\text{exp}} = 1.5 \text{ ms}$ . Additionally the red and green (blue) line show vertical (horizontal) cuts through the intensity in arbitrary units.

Due to the relatively large uncertainty the findings can not completely confirm the assumptions made regarding the dipole trap geometry but instead have been used to determine boundaries for the dimension and density inside the atomic cloud. The waist measurements of the dipole trap beams combined with the limits given by the analysis of the absorption images and the radial trap frequency measurement have been used to impose upper limits on the beam radii at the crossing point of the trapping beams. For this the upper limit of the distance of the two beam waist positions I assumed a displacement of 6.5 mm which results in an axial extension of the cloud of 45  $\mu\text{m}$  and 50  $\mu\text{m}$  after the evaporation ramps with final power ( $P_{\text{hor}} = 1.2 \text{ W}$ ;  $P_{\text{tilt}} = 0.6 \text{ W}$ ) and ( $P_{\text{hor}} = 1 \text{ W}$ ;  $P_{\text{tilt}} = 0.25 \text{ W}$ ), respectively.

Fig. 5.12 shows the experimental results complemented by calculations that take the upper limits imposed by the absorption images into account as well as all other modifications presented earlier this chapter. It is important to remember that a changed trapping volume does not only alter the conversion of the atom number to the density dependent values but also effects the local intensity of the photoassociation beam since due to the increased trapping region the atoms inside the dipole beams do not necessarily experience the same spectroscopic intensity. The gray shaded area below the green curve and the bars on top the data points indicate the range that is compatible with the upper limit for the trap volume. Even this unlikely modification of the experimental parameters does not resolve the discrepancy and can only reduce the disagreement by a factor of four compared to the results that assumed the initial parameters of the dipole trap setup. Also even considering the reduced intensities the numerical calculation still suggest saturation of the rate coefficients that can not be seen in the data.

This chapter investigated possible explanations for the deviations between the experimental and theoretical photoassociation rates. Including various previously neglected effects to the simulation, a local intensity confirmed by measurement of the Autler-Townes splitting and an upper limit on the trap dimension that is still compatible to absorption images does not resolve the disagreement. Even a combination of all effects would does not resolve the disparity between the measured and calculated rates entirely.

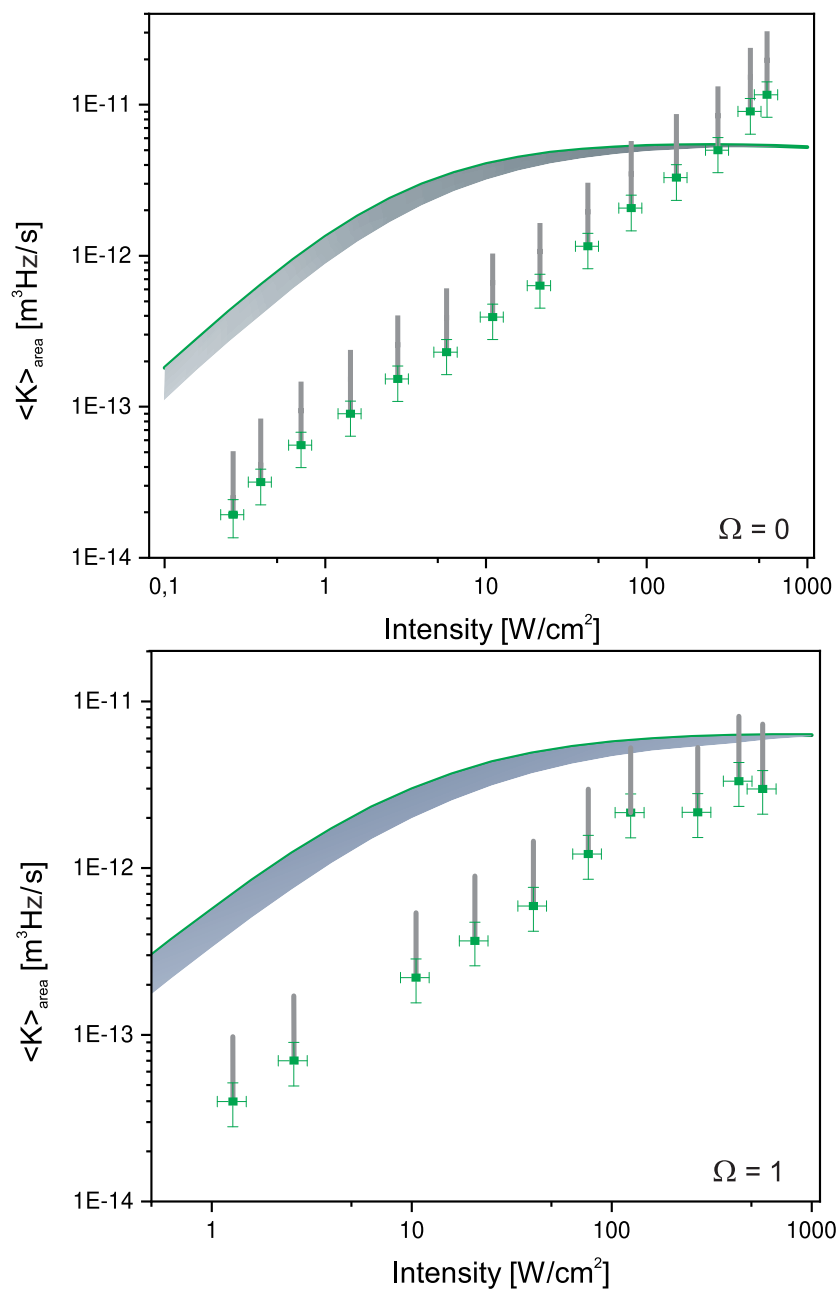


Figure 5.12: Integrated two body loss coefficient  $\langle K \rangle_{\text{area}}$  as function of photoassociation intensity  $I_{\text{PA}}$  for the two molecular lines with  $\Omega = 0; 1$ . The green squares show the experimental data together with their respective uncertainty as described in Tab. 4.1. The green line indicates the corresponding theoretical prediction. In the unlikely case of a misaligned focusing lens of the tilted dipole trap beam the gray regions indicate the influence on the experimental and theoretical values.

# Chapter 6

## Adjustment of the theoretical parameters

The reevaluation of the experimental modeling and introduction of extensions and the review of approximations could not resolve the disagreement between simulated and measured photoassociation rates. Even when imposing generous extended limits on the experimental parameters the measured rates differ by about a factor of 4 from the prediction at low intensity. Investigations of the photoassociation process in other elements with an electronic structure similar to  $^{40}\text{Ca}$ , such as strontium and ytterbium, in a thermal cloud [Kim16] as well as in an optical lattice [Zel06, Res18] show the same tendency of reduced photoassociation rates. In these references a common approach to resolve this discrepancy is an adjustment of the optical length, i.e. the Franck-Condon density combined with a modification of the natural linewidth  $\gamma_1$ . I have studied the effect of these modifications on the simulated spectra and whether they can also be applied in the case of calcium to resolve the discrepancies and more importantly at intensities past saturation that have not been studied previously.

### 6.1 Adjustment of the Franck-Condon density

The first and most obvious way to reduce the simulated rate is to decrease the coupling parameter  $f_{\text{FCD}}$  or equivalently  $l_{\text{opt}}$ . For this purpose, a scaling factor for the two-body loss rate was determined that brings the modified simulation and measurement in agreement in the area of low intensity where the rate increases linearly with the intensity. The scaling factor was then used in a subsequent step to simulate the photoassociation spectra at high intensities which should show clear signs of broadening and saturation. These modified calculated loss spectra were then again compared to the experimental data. Also the expected integrated rate was determined using these parameters to validate if a simple scaling factor is sufficient to reduce the discrepancy between the theoretical and measured values. Focusing on the line in the

$v' = -1; \Omega = 0$  state first, the graphs in Fig. 6.1 show the measurements together with a simulation including the modifications discussed in the last chapter. The simulated  $\langle K \rangle$  values have to be multiplied by a factor of  $f_{\text{scale}, \Omega=0} = \frac{1}{5.5}, \frac{1}{6}, \frac{1}{5.5}$  in order to give a good agreement with the measured values at the three lowest intensities that were used in the measurement ( $0.267 \text{ Wcm}^{-2}, 0.396 \text{ Wcm}^{-2}, 0.705 \text{ Wcm}^{-2}$ ). Not considering the modifications presented in the last chapter, using the design values yields a scaling factor of  $f_{\text{scale}} = \frac{1}{19}$  instead as was shown previously. A similar analysis has been done for the three smallest intensity values the  $v' = -1; \Omega = 1$  resonance has been measured at. In this case (Fig. 6.2) the average scaling factor was determined to  $f_{\text{scale}, \Omega=1} = \frac{1}{4.2}$ , with all modifications presented in chapter 5.

After I determined the scaling factors for the respective transitions I simulated spectra including this factor in the calculation of the stimulated rate by substituting  $\Gamma_{\text{stim}}^* = f_{\text{scale}} \cdot \Gamma_{\text{stim}}$  and again compared the result to the measured data in the limit of low intensities (see Figs. 6.1,6.2) and high intensities (see Fig. 6.3). In the case of low intensity the simulated atom loss spectra now agree well with the experimental data concerning both the absolute loss of atoms from the trap as well as the width of the resonance for both the  $v' = -1; \Omega = 0$  and  $v' = -1; \Omega = 1$  states investigated. At high intensities on the other hand the absolute rate as well as the width of the resonance now show a poorer agreement compared to the unmodified Franck-Condon density. Especially the simulated width shows no sign of the broadening effects visible in the experimental data. It becomes clear that introducing a simple scaling factor for the coupling parameter could only resolve the discrepancies at low intensity. At higher spectroscopic intensity beyond the saturation intensity the calculations do not show any increase of the width of the spectra that is a distinct feature of the experimental data. Unfortunately, experimental investigations of Group-II atoms besides calcium are in the low intensity regime.

## 6.2 Additional non radiative decay channels

A second molecular parameter that can be adjusted is the decay rate of the excited molecular state. Since the states that have been probed are only weakly bound less than a GHz away from the atomic asymptote, a collision with background gas or with another atom or molecule could lead to a decay of the state introducing a so far unconsidered non-radiative decay channel. Furthermore, the decay rate does not necessarily need to be constant for different intensities in the saturation regime as



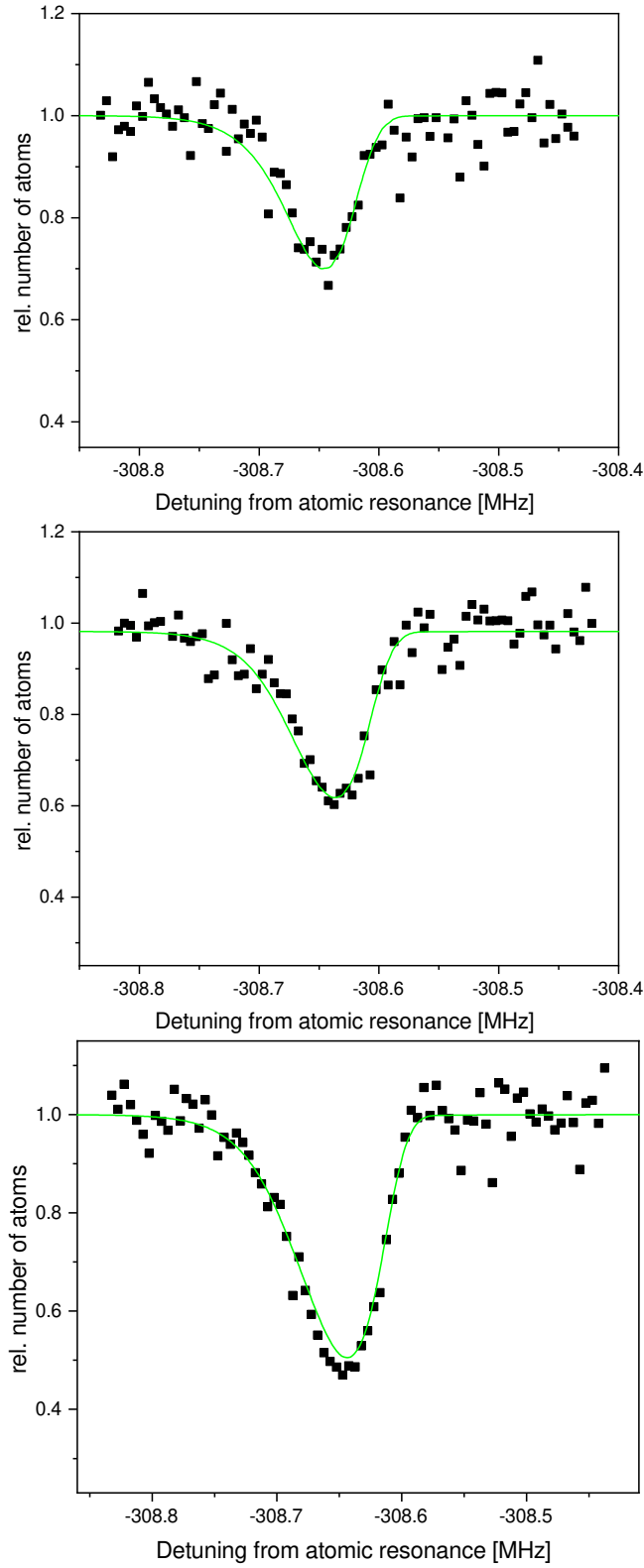


Figure 6.1: Simulated spectra (green line) with a reduced Franck-Condon density for the  $v' = -1; \Omega = 0$  state using a radial dipole trap extension of  $\sigma_{\text{axial}} = 45 \mu\text{m}$  at low intensities ( $I_{PA} = 0.267 \text{ Wcm}^{-2}$ ;  $0.396 \text{ Wcm}^{-2}$ ;  $0.705 \text{ Wcm}^{-2}$ ). Also shown are the experimental measurements (black squares).

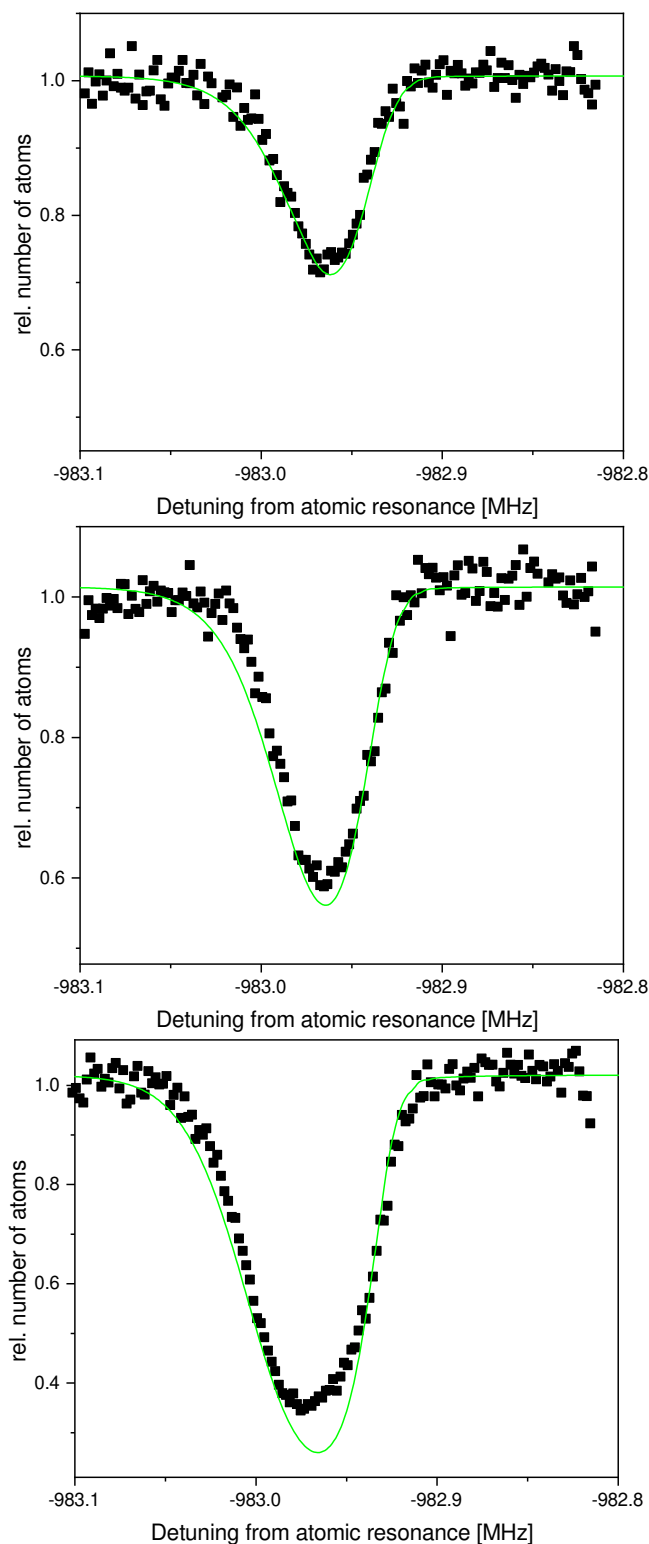


Figure 6.2: Simulated spectra (green line) with a reduced Franck-Condon density for the  $v' = -1; \Omega = 1$  state using a radial dipole trap extension of  $\sigma_{\text{axial}} = 50 \mu\text{m}$  at low intensities ( $I_{\text{PA}} = 1.277 \text{ Wcm}^{-2}; 2.577 \text{ Wcm}^{-2}; 10.51 \text{ Wcm}^{-2}$ ). Also shown are the experimental measurements (black squares).

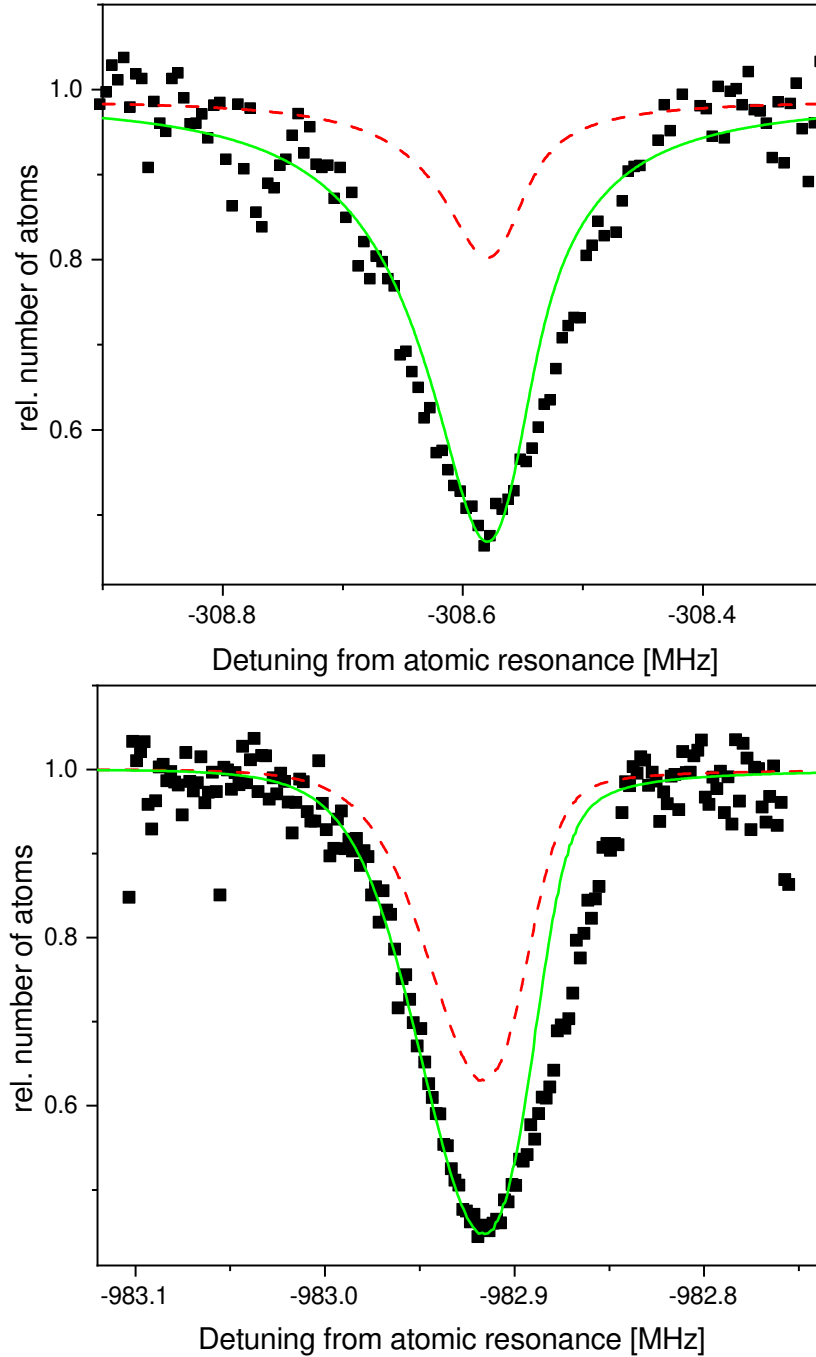


Figure 6.3: Simulated spectra (red dashed line) with a reduced Franck-Condon density for the  $v' = -1; \Omega = 0$  ( $v' = -1; \Omega = 1$ ) state using a radial dipole trap extension of  $\sigma_{\text{axial}} = 45(50) \mu\text{m}$  at high intensity  $I_{\text{PA}} = 560(569 \text{ Wcm}^{-2})$ . Also shown are the experimental measurements (black squares) and the simulation that has been scaled to match the peak loss (solid green line).

the molecular state can potentially couple to other bound states in addition to the coupling to the continuum states in the ground state. The additional coupling could lead to a modification of the natural decay rate that has also been proposed by other groups studying the absolute molecule formation rate in photoassociation experiments [Zel06, Kim16]. I have analyzed the influence of arbitrary additional decay channels by introducing a decay width  $\Gamma_{\text{extra}}$  into the simulation modifying the natural width when calculating the scattering matrix element in Eq. 2.4 by

$$\gamma_1 = \gamma_{\text{mol}} = 2\gamma_{\text{atom}} \rightarrow \gamma'_1 = \gamma_{\text{mol}} + \Gamma_{\text{extra}}. \quad (6.1)$$

The spectra simulated using this additional width show a growing saturation intensity with growing  $\Gamma_{\text{extra}}$  and also the integrated rate saturates only at a higher value as can be seen in Fig. 6.4. This is expected from the scattering matrix element given in Eq. 2.4. Using a combination of an adjusted Franck-Condon density and a suitable  $\Gamma_{\text{extra}}$  it is possible to achieve an agreement between the simulated integrated rate and the measured data. However, when comparing the spectra directly it becomes obvious that the width of the simulation is now in poor agreement and no broadening is visible (compare Fig. 6.5) at high intensities. This also means that the peak loss rate will be overestimated in return.

In conclusion even after taking multiple experimental uncertainties into consideration and including additional effects into the calculation of the theoretical rates they can still not be brought into agreement with the measured data. Even changing the Franck-Condon density and the natural width does only improve the overall agreement of the integrated photoassociation rate while it on the other hand introduces additional disagreements regarding the width of the spectral features. Considering these results it is safe to say that the presented theoretical description of the photoassociation process is not capable to accurately describe the experimental data in the case of  $^{40}\text{Ca}$  at intensities that are high compared to the intensity at which the molecular resonance saturates.

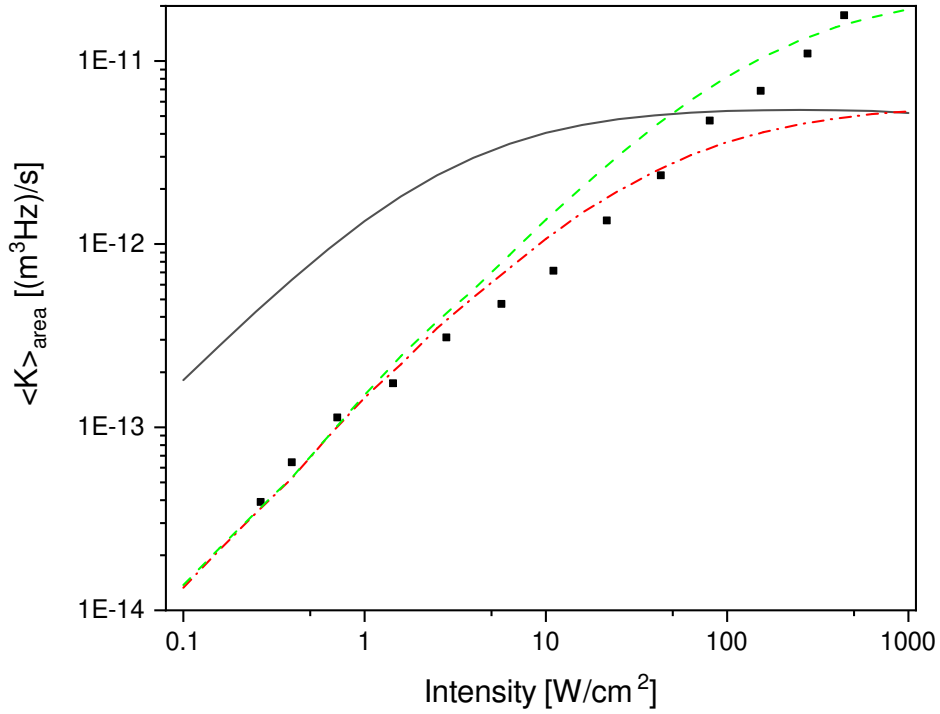


Figure 6.4: Integrated two body loss coefficient  $\langle K \rangle_{\text{area}}$  as function of photoassociation intensity  $I_{\text{PA}}$  for the molecular line with  $\Omega = 0$ . The solid black line indicates a simulation including an extended atomic cloud with a radial extension of  $45 \mu\text{m}$  and the original molecular parameters. The dashed-dotted red line shows the simulation with an adjusted Franck-Condon density (reduced by a factor of  $\frac{1}{7}$ ) in order to match the integrated rate at low intensities, while for the dashed green line an additional decay width  $\Gamma_{\text{extra}} = 2.5 \text{ kHz}$  has been assumed to improve the agreement at high intensity.

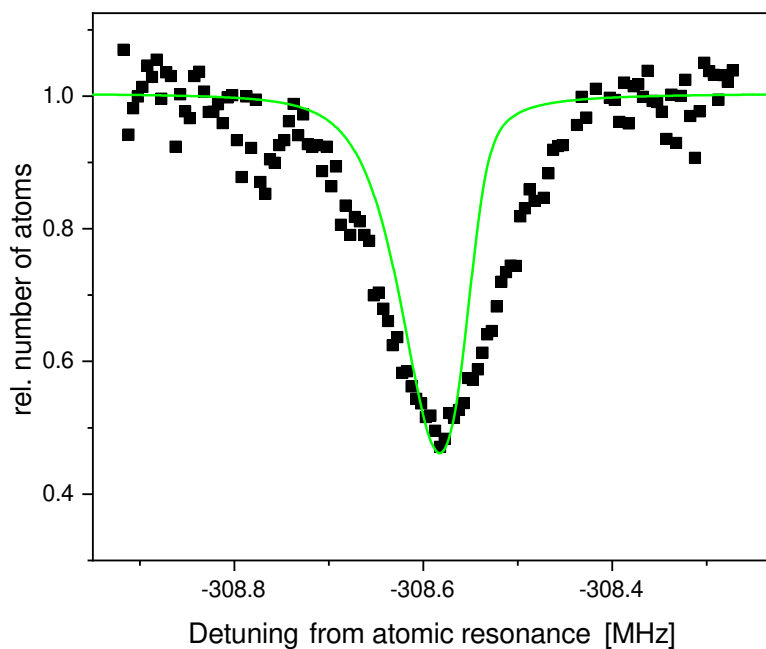


Figure 6.5: Simulated spectrum (green line) for the  $v' = -1; \Omega = 0$  state using a radial dipole trap extension of  $\sigma_{\text{axial}} = 45 \mu\text{m}$  combined with a Franck-Condon density reduced by a factor of 7 and an additional decay width of  $\Gamma_{\text{extra}} = 2.5 \text{ kHz}$ . The simulation was scaled to match the peak atom losses. Also shown are the experimental measurements (black squares).

# Chapter 7

## Summary

In this thesis the interaction of light with the ultracold bosonic calcium isotope  $^{40}\text{Ca}$  has been studied by means of photoassociation spectroscopy. I have measured the loss of atoms from an optical trap as a laser associated atom pairs to weakly bound excited molecular states. Over a spectroscopy intensity range of three magnitudes and up to  $600 \text{ Wcm}^{-2}$  the resonant features in the vicinity of two molecular bound states have been studied regarding the absolute molecule formation rate, the width of the resonance lines and the overall shape. This is the first systematic evaluation of photoassociation rates in group II atoms in this intensity range considering the small linewidth of the atomic transition. The experimental results have been compared to numerical calculation of the process that is based on a scattering formalism based on the works of Bohn and Julienne [Boh99].

For this ensembles of calcium atoms were prepared at low  $\mu\text{K}$  temperature by means of magneto optical cooling and evaporative cooling in a crossed dipole trap. To achieve the highest accuracy the spectroscopy laser was stabilized to a mechanical reference with a stability of  $3 \cdot 10^{-15}$  after one second which is substantially smaller than the linewidth of the molecular resonances that have been studied. I have found that the measured absolute photoassociation rates for the two most-weakly bound states in the excited potential dissociating to the  $^3P_1 + ^1S_0$  asymptote significantly deviate from numerical calculations across the entire intensity range. For the given experimental parameters the measured rates are lower by a factor of 19 and 16 for the two states that have been probed respectively. While the expected linear increase of the molecule formation rate is reproduced by the experiment at the lowest used spectroscopic intensities I have found that at higher intensities the experimental data does not show signs of saturation as suggested by the simulations. Further the experimental data show a reasonable agreement regarding the width of the molecular resonances also up to high spectroscopic intensities when compared to theoretical calculation which im-

plies that assumed optical coupling is treated correctly by the theoretical formalism. I have further studied the light shift induced by the spectroscopy laser and compared the measured average shift as a function of the intensity to calculated shifts based on molecular wave functions based on a coupled channel model of the two atom system with the results that the measured shift is substantially smaller than expected. To resolve the discrepancies, the theoretical model has been extended by including previously neglected effects and a more refined description of the experimental setup. The influence of the extension of the theoretical modeling of the spectroscopy process and the modeling of the experimental environment have been studied and compared to the measured results. The absolute intensity of the spectroscopy beam at the trap position has been verified by a comparison of the results of Autler-Townes spectroscopy measurements which reproduced the estimated overlap between the excited and ground state molecular wavefunctions determined from the molecular potentials. Since the measured rates are extremely sensitive to the parameters of the optical trap the atoms are stored in the dependency of the resonance shape and absolute rate from the trap volume was studied. For this upper limits to the trap size have been derived from absorption images. The influence of the changed trap dynamics have been investigated theoretically with the outcome that even a substantial increase of the dipole trap volume is not suited to explain the experimental results especially in regards to the saturation that could no be seen in the experimental data. I have further excluded the possibility of substantial recapture of products from the molecular decay by the optical dipole trap. From measurements for different depth of the optical trap I concluded that there is no meaningful reduction of the measured photoassociation rates by recapture of atoms from decaying excited molecules. Finally the theoretical parameters the simulated spectra are generated from are varied in order to produce consistency with the measured result. In earlier photoassociation measurements at intensities far from saturation a scaling of the optical coupling together with an enhanced linewidth were needed to achieve a good agreement between calculated and experimental spectra. I found that at high intensities this approach can indeed lead to agreement of the photoassociation rates while the shape of the spectra is no longer found to be in agreement. The previously correctly reproduced width of the molecular resonances is now underestimated by the simulations based on the theory with adjusted parameters. This means that while this simple modification of the molecular parameters is sufficient at low intensity the situation at higher intensities is more complicated and would benefit from additional experimental data from other alkaline earth elements as well



as a more specialized theoretical treatment.



# Chapter 8

## Outlook

### 8.1 Optical lattice

In order to dispel doubts about the results the biggest uncertainty contribution to the experiment by the size of the trapping region can be partly eliminated in the future by using an optical lattice trap instead of a crossed dipole trap. Such a setup has been planned and partly installed already and shall be described in the following. In addition to the reduced uncertainty such a setup also reduces the Doppler broadening of the measured photoassociation lines, the nature of the distribution of initial collision energies relevant for the Franck-Condon densities as well the resonance condition in Eq. 2.4 by enabling spectroscopy in the Lamb-Dicke regime [Dic53]. The optical lattice [Per98, Ido03] relies on the dipole force similar to the crossed optical dipole trap that is already in use. By means of a retroreflected strongly focused laser beam an electrical field according to

$$\begin{aligned}\vec{E} &= \vec{E}_0 \cos(kz - \omega t) + \vec{E}_0 \cos(-kz - \omega t) \\ |\vec{E}|^2 &= 2|E_0|^2 \cos^2(kz)\end{aligned}$$

is generated at the position of the atoms. In this spatially varying electric field the atoms experience an AC Stark shift that is proportional to the polarizability  $\alpha(\omega)$  of the atoms that can be expressed locally by

$$\Delta E = -\frac{1}{2}\alpha(\omega)|\vec{E}|^2.$$

Assuming that the lattice consists of a Gaussian beam with a local beam radius of  $w(z)$  along its propagation direction focused to a waist size  $w_0$  the periodic potential the atoms experience is given by

$$U_{\text{lattice}}(r, z) = U_0 \exp\left(-\frac{2r^2}{w(z)^2}\right) \cos^2\left(\frac{2\pi z}{\lambda_{\text{lat}}}\right).$$

In this equation the wavelength of the lattice laser is given by  $\lambda_{\text{lat}}$  and the maximum depth of the potential is  $U_0 = 4\frac{\alpha P}{\pi\epsilon_0 c w_0^2}$  where the polarizability  $\alpha$  is evaluated at the wavelength of the lattice laser with power  $P$ . For this equation to hold I have assumed that the polarization and power of the two counterpropagating beams do not change significantly crossing through viewports of the vacuum chamber which is sufficient for now but needs to be validated by measurements. In a harmonic approximation of the potential the axial and radial vibrational frequencies of a Calcium atom in such a potential is given by [Bla09]

$$\begin{aligned} \nu_{\text{axial}} &= 2\sqrt{\nu_{\text{rec}}}\sqrt{\frac{U_0}{h}} \\ \text{and } \nu_{\text{rad}} &= \sqrt{\frac{U_0}{m_{\text{Ca}}\pi^2 w_0^2}} \\ \text{with } \nu_{\text{rec}} &= \frac{h}{2m_{\text{Ca}}\lambda_{\text{lat}}^2}. \end{aligned}$$

The experiment has been extended by a commercial *Toptica - TA Pro* system that consists of an ECDL operating at around 800 nm that is amplified by a tapered amplifier. To suppress feedback from reflections at the retroreflecting mirror of the lattice the light is sent through a Faraday Isolator *QiOptics FI-500/820-5SV* with a transmission of >90 % and an optical isolation of 40 dB. The frequency and intensity of the laser can be finely adjusted by an AOM *Gooch & Housego 3080-122* operating at 80 MHz and the laser is feed to the experiment via polarization maintaining optical fiber with a mode field diameter of 12.4  $\mu\text{m}$  (*NKT - aeroGUIDE-15-PM*). In front of the vacuum chamber the beam is collimated by an achromatic doublet lens with a focal length of 100 mm leading to a beam radius of 5.3 mm. Subsequently the beam is focused by another achromatic doublet lens with a focal length of 400 mm leading to a waist of 24.8  $\mu\text{m}$  at the crossing point with the atomic sample in the dipole trap. On the other side of the chamber the beam is recollimated by a lens of the same focal length before being reflected forming a standing wave. An overview of the lattice setup is given in Fig. 8.1 and also shows that part of the light is used in an analysis port for ensuring the single-mode structure of the ECDL as well as the possibility to monitor the exact wavelength.

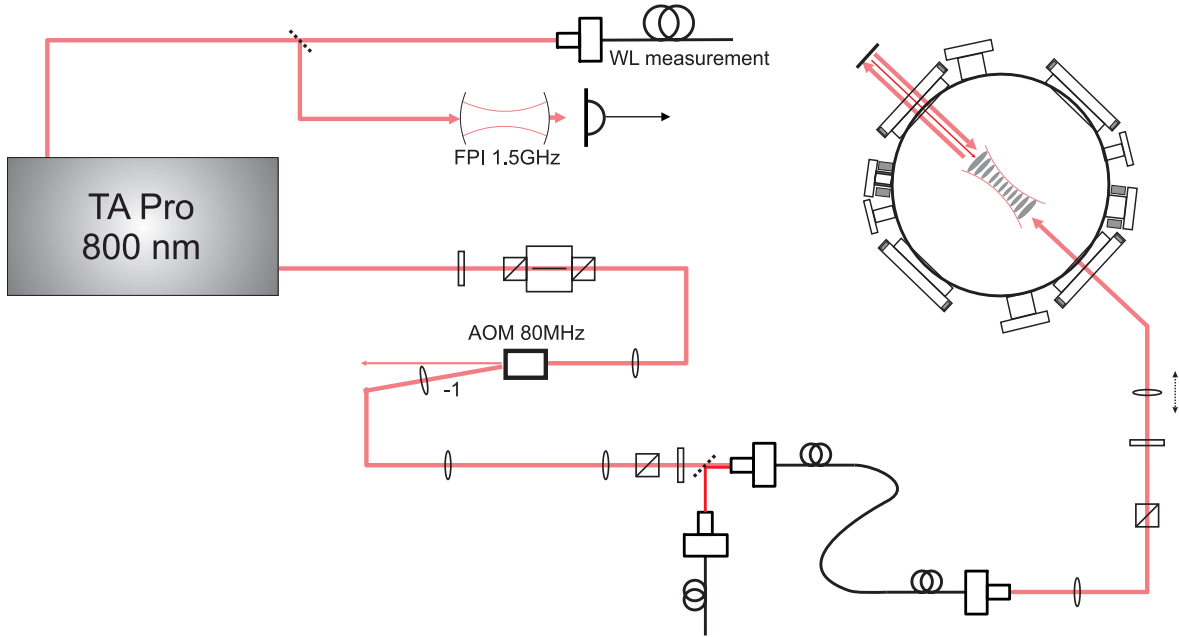


Figure 8.1: Schematic drawing of the newly implemented setup for trapping of atoms inside an optical lattice.

In total a power of up to 1 W is available for the generation of the optical lattice. The polarizability for  $\sigma$  polarized light at 800.8 nm is  $\alpha = h \cdot 54.6 \text{ m}^2\text{Hz}/\text{V}^2$  [Deg04b]. From the parameters a maximum trap depth of  $U_0 = 67 E_{\text{rec}}$  with trapping frequencies of  $\nu_{\text{axial}} = 127 \text{ kHz}$  and  $\nu_{\text{rad}} = 695 \text{ Hz}$  are expected. The trap depth is given in multiples of the recoil energy due to absorption of a lattice photon defined as  $E_{\text{rec}} = \hbar^2 k^2 / 2m_{\text{Ca}}$ . Furthermore the wavelength of the lattice laser is magic for the triplet transition  $^1S_0 - ^3P_1$  of  $^{40}\text{Ca}$  that means that the differential lightshift between the excited and ground state is zero to first order (see Fig. 8.2 taken from [Deg04b]). This simplifies the analysis of the recorded spectra substantially since the line is not artificially broadened due to local variations of the trapping potential, e.g. an atom pair away from the center of the lattice beam would experience a smaller shift due the reduced intensity towards the edge of the Gaussian beam. The beam power will be stabilized by an AOM in front of the fiber leading to experiment using a fraction of the lattice light that leaves the chamber on the side of the spectroscopy laser that is reflected from the vacuum window. The power will be monitored by a photodiode and through a feedback loop by adjusting the output of the VCO controlling the AOM it can be held constant similar to the setup steering the dipole trap ramps. This should also allow evaporative cooling directly in the lattice by slowly reducing the power in the trap beam.

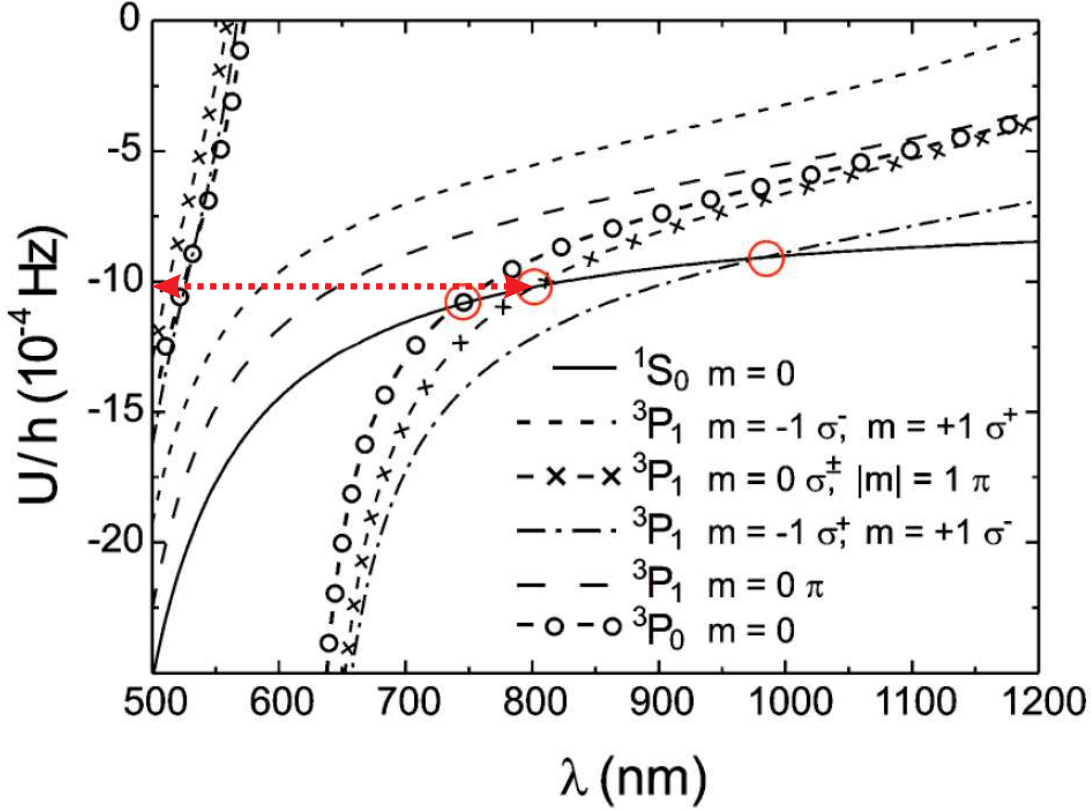


Figure 8.2: Induced ac Stark shift  $U/h$  at a laser intensity of  $1 \text{ W/m}^2$  from [Deg04b]. The horizontal red line indicates the point at which the polarizability of the ground state  $^1S_0$  is equal to the excited state  $^3P_1$  at  $800.8 \text{ nm}$ . The red circles denote other magic wavelength for different polarizations of the light e.g. at  $983$  which is close to the frequency used for the optical dipole trap.

The calcium atoms are stored in multiple flat pancake-like structures spaced by half of the lattice laser wavelength that lead to quantized vibrational states in the axial direction of the lattice beams where predominantly the ground state is populated. In the weakly bound radial direction the atoms are effectively confined to a 2D motion. In this configuration the atoms are in the Lamb-Dicke regime [Dic53] and can be excited by the spectroscopy beam without changing their motional quantum state thus allowing measurements with strongly suppressed Doppler broadening and recoil shift at least along the direction of the optical lattice. This technique has already successfully been employed in optical-clock experiments [Fal14, Nic15b] as well as photoassociation measurements [Rei12] for the alkaline-earth element strontium. In the future this

spectroscopy scheme can also be used in our setup since the retroreflective mirror is specifically designed such that its coating is highly transmissive for light at a wavelength of 657 nm allowing the spectroscopy laser to be used parallel to the axial lattice direction.





# Appendices

## Appendix A: Density conversion

In order to convert the differential equation for the evolution of the local density inside the atomic sample to the experimentally accessible total number of trapped atoms the differential equation is integrated over the trap volume:

$$\begin{aligned}\dot{N} &= \int \dot{\rho}(\vec{r}) d^3r \\ &= - \int 2 \langle K \rangle \rho^2(\vec{r}) d^3r \stackrel{!}{=} -\beta N^2\end{aligned}$$

with  $\beta$  as an atom loss factor. Further I have assumed that the atoms are thermally distributed inside the trap with axial rms radii  $\sigma_x, \sigma_y, \sigma_z$  according to

$$\rho(x, y, z) = \rho_0 \exp\left(-\frac{x^2}{2\sigma_x^2} - \frac{y^2}{2\sigma_y^2} - \frac{z^2}{2\sigma_z^2}\right).$$

By integration of the density the total number of atoms  $N$  follows to

$$\begin{aligned}N = \int \rho d^3r &= \rho_0 \int \exp\left(-\frac{x^2}{2\sigma_x^2} - \frac{y^2}{2\sigma_y^2} - \frac{z^2}{2\sigma_z^2}\right) dx dy dz \\ &= \rho_0 \sqrt{2\pi}^3 \sigma_x \sigma_y \sigma_z\end{aligned}$$

If the thermal distribution of the atoms in the trap is not altered significantly by the losses induced by the photoassociation laser the loss of atoms from the trap can be written as

$$\begin{aligned}\dot{N} &= -2 \langle K \rangle \rho_0^2 \int \exp\left(-\frac{x^2}{2\sigma_x^2} - \frac{y^2}{2\sigma_y^2} - \frac{z^2}{2\sigma_z^2}\right)^2 d^3r \\ &= -2 \langle K \rangle \rho_0^2 \int \exp\left(-\frac{x^2}{\sigma_x^2} - \frac{y^2}{\sigma_y^2} - \frac{z^2}{\sigma_z^2}\right) d^3r \\ &= -2 \langle K \rangle \rho_0^2 \sqrt{\pi}^3 \sigma_x \sigma_y \sigma_z.\end{aligned}$$

By inserting this expression into the initial differential equation, the relation between photoassociation rate  $\langle K \rangle$  and the loss factor for atoms in the trap  $\beta$  can be determined

$$\begin{aligned}\dot{N} &= -2 \langle K \rangle \rho_0^2 \sqrt{\pi}^3 \sigma_x \sigma_y \sigma_z = -\beta \rho_0^2 (2\pi)^3 (\sigma_x \sigma_y \sigma_z)^2 = -\beta N^2 \\ \rightarrow \beta &= \frac{1}{\sqrt{2} V_{\text{DT}}} \langle K \rangle,\end{aligned}$$

where the factor  $V_{\text{DT}} = \sqrt{2\pi}^3 \sigma_x \sigma_y \sigma_z$  is the dipole trap volume.

## Bibliography

- [All03] O. Allard, C. Samuelis, A. Pashov, H. Knöckel and E. Tiemann, “Experimental study of the  $\text{Ca}_2$   $^1\text{S} + ^1\text{S}$  asymptote”, *Eur. Phys. J. D* **26**, 155 (2003).
- [All04] Olivier Allard, *Long-Range Interactions in the Calcium Dimer studied by Molecular Spectroscopy*, PhD thesis Universität Hannover Welfengarten 1 2004 online available at <http://www.tib.uni-hannover.de>.
- [All05] O. Allard, St. Falke, A. Pashov, O. Dulieu, H. Knöckel and E. Tiemann, “Study of coupled states for the  $(4s^2)^1\text{S} + (4s4p)^3\text{P}$  asymptote of  $\text{Ca}_2$ ”, *Eur. Phys. J. D* **35**, 483 (2005).
- [App13] Oliver Appel, *Bose-Einstein Condensation and Narrow-Line Photoassociation Spectroscopy of Calcium*, PhD thesis Fakultät für Mathematik und Physik der Gottfried Wilhelm Leibniz Universität Hannover 2013 08/2013 eingereichte Version.
- [Aut55] S. H. Autler and C. H. Townes, “Stark Effect in Rapidly Varying Fields”, *Phys. Rev.* **100**, 703 (1955).
- [Bev89] N. Beverini, F. Giammanco, E. Maccioni, F. Strumia and G. Vissani, “Measurement of the calcium  $^1\text{P}_1$ - $^1\text{D}_2$  transition rate in a laser-cooled atomic beam”, *J. Opt. Soc. Am. B* **6**, 2188 (1989).
- [Bin01] T. Binnewies, G. Wilpers, U. Sterr, F. Riehle, J. Helmcke, T. E. Mehlstäubler, E. M. Rasel and W. Ertmer, “Doppler cooling and trapping on forbidden transitions”, *Phys. Rev. Lett.* **87**, 123002 (2001).
- [Bla09] S. Blatt, J. W. Thomsen, G. K. Campbell, A. D. Ludlow, M. D. Swallows, M. J. Martin, M. M. Boyd and J. Ye, “Rabi spectroscopy and excitation inhomogeneity in a one-dimensional optical lattice clock”, *Phys. Rev. A* **80**, 052703 (2009).

- [Boh96] John L. Bohn and P. S. Julienne, “Semianalytic treatment of two-color photoassociation spectroscopy and control of cold atoms”, *Phys. Rev. A* **54**, R4637 (1996).
- [Boh99] John L. Bohn and P. S. Julienne, “Semianalytic theory of laser-assisted resonant cold collisions”, *Phys. Rev. A* **60**, 414 (1999).
- [Bor27] M. Born and R. Oppenheimer, “Zur Quantentheorie der Molekeln”, *Annalen der Physik* **20**, 457 (1927).
- [Boy07] Martin M. Boyd, *High Precision Spectroscopy of Strontium in an Optical Lattice: Towards a New Standard for Frequency and Time*, PhD thesis Graduate School of the University of Colorado 2007.
- [Chi01] Cheng Chin, Véronique Leiber, Vladan Vuletić, Andrew J. Kerman and Steven Chu, “Measurement of an electron’s electric dipole moment using Cs atoms trapped in optical lattices”, *Phys. Rev. A* **63**, 033401 (2001).
- [Ciu04] R. Ciuryło, E. Tiesinga, S. Kotochigova and P. S. Julienne, “Photoassociation spectroscopy of cold alkaline-earth-metal atoms near the intercombination line”, *Phys. Rev. A* **70**, 062710 (2004).
- [Ciu06] R. Ciuryło, E. Tiesinga and P. S. Julienne, “Stationary phase approximation for the strength of optical Feshbach resonances”, *Phys. Rev. A* **74**, 022710 (2006).
- [Deg04a] Carsten Degenhardt, *Freie und gespeicherte Calcium-Atome für ein optisches Frequenznormal*, PhD thesis Universität Hannover Welfengarten 1 2004 online available at <http://www.tib.uni-hannover.de>.
- [Deg04b] Carsten Degenhardt, Hardo Stoehr, Uwe Sterr, Fritz Riehle and Christian Lisdat, “Wavelength dependent ac-Stark shift of the  $^1S_0$ - $^3P_1$  transition at 657 nm in Ca”, *Phys. Rev. A* **70**, 023414 (2004).
- [Deg05] Carsten Degenhardt, Hardo Stoehr, Christian Lisdat, Guido Wilpers, Harald Schnatz, Burghard Lipphardt, Tatiana Nazarova, Paul-Eric Pottie, Uwe Sterr, Jürgen Helmcke and Fritz Riehle, “Calcium optical frequency standard with ultracold atoms: Approaching  $10^{-15}$  relative uncertainty”, *Phys. Rev. A* **72**, 062111 (2005).

- [Dic53] R. H. Dicke, “The Effect of Collisions upon the Doppler Width of Spectral Lines”, *Phys. Rev.* **89**, 472 (1953).
- [Dre83] R. W. P. Drever, J. L. Hall, F. V. Kowalski, J. Hough, G. M. Ford, A. J. Munley and H. Ward, “Laser Phase and Frequency Stabilization Using an Optical Resonator”, *Appl. Phys. B* **31**, 97 (1983).
- [Edm57] A. R. Edmonds, *Angular momentum in quantum mechanics*, (Princeton University Press, Princeton, New Jersey, 1957) .
- [Eno07] K. Enomoto, M. Kitagawa, K. Kasa, S. Tojo and Y. Takahashi, “Determination of the s-Wave Scattering Length and the  $C_6$  van der Waals Coefficient of  $^{174}\text{Yb}$  via Photoassociation Spectroscopy”, *Phys. Rev. Lett.* **98**, 203201 (2007).
- [Esc08] Y. N. Martinez de Escobar, P. G. Mickelson, P. Pellegrini, S. B. Nagel, A. Traverso, M. Yan, R. Côté and T. C. Killian, “Two-photon photoassociative spectroscopy of ultracold  $^{88}\text{Sr}$ ”, *Phys. Rev. A* **78**, 062708 (2008).
- [Ess55] L. Essen and J. V. L. Parry, “An Atomic Standard of Frequency and Time Interval: A Caesium Resonator”, *Nature* **176**, 280 (1955).
- [Fal14] Stephan Falke, Nathan Lemke, Christian Grebing, Burghard Lipphardt, Stefan Weyers, Vladislav Gerginov, Nils Huntemann, Christian Hagemann, Ali Al-Masoudi, Sebastian Häfner, Stefan Vogt, Uwe Sterr and Christian Lisdat, “A strontium lattice clock with  $3 \times 10^{-17}$  inaccuracy and its frequency”, *New J. Phys.* **16**, 073023 (2014).
- [Ger10] V. Gerginov, N. Nemitz, S. Weyers, R. Schröder, R. D. Griebisch and R. Wynands, “Uncertainty evaluation of the caesium fountain clock PTB-CSF2”, *Metrologia* **47**, 65 (2010).
- [Gri00] Rudolf Grimm, Matthias Weidemüller and Yurii B. Ovchinnikov, “Optical Dipole Traps for Neutral Atoms”, *Adv. At. Mol. Opt. Phys.* **42**, 95 (2000).
- [Hal05] Jan Hald and Valentina Ruseva, “Efficient suppression of diode-laser phase noise by optical filtering”, *J. Opt. Soc. Am. B* **22**, 2338 (2005).

- [Her50] Gerhard Herzberg, *Molecular Spectra and Molecular Structure: I. Spectra of Diatomic Molecules*, (D. van Nostrand company, Inc., Toronto, New York, London, 1950) 2nd edition.
- [Hun14] Nils Huntemann, *High-accuracy optical clock based on the octupole transition in  $^{171}\text{Yb}$* , PhD thesis Leibniz Universität Hannover 2014.
- [Hun16] N. Huntemann, C. Sanner, B. Lipphardt, Chr. Tamm and E. Peik, “Single-Ion Atomic Clock with  $3 \times 10^{-18}$  Systematic Uncertainty”, *Phys. Rev. Lett.* **116**, 063001 (2016).
- [Ido03] Tetsuya Ido and Hidetoshi Katori, “Recoil-Free Spectroscopy of Neutral Sr Atoms in the Lamb-Dicke Regime”, *Phys. Rev. Lett.* **91**, 053001 (2003).
- [Kah14a] Max Kahmann, *Link Between Photoassociation and Optical Feshbach Resonances Through the Example of Calcium*, PhD thesis QUEST-Leibniz-Forschungsschule der Gottfried-Wilhelm-Leibniz Universität Hannover 2014 online.
- [Kah14b] Max Kahmann, Eberhard Tiemann, Oliver Appel, Uwe Sterr and Fritz Riehle, “Photoassociation spectroscopy of  $^{40}\text{Ca}$  measured with kilohertz accuracy near the  $^3\text{P}_1+^1\text{S}_0$  asymptote and its Zeeman effect”, *Phys. Rev. A* **89**, 023413 (2014).
- [Kat02] Hidetoshi Katori, “Spectroscopy of strontium atoms in the Lamb-Dicke confinement”, in , *Proceedings of the Sixth Symposium on Frequency Standards and Metrology, 9–14 September 2001, St. Andrews, Scotland*, edited by P. Gill, (World Scientific, Singapore, 2002) , S. 323–330.
- [Ket93] Wolfgang Ketterle, Kendall B. Davis, Michael A. Joffe, Alex Martin and David E. Pritchard, “High Densities of Cold Atoms in a Dark Spontaneous-Force Optical Trap”, *Phys. Rev. Lett.* **70**, 2253 (1993).
- [Kim16] Min-Seok Kim, Jeongwon Lee, Jae Hoon Lee, Y. Shin and Jongchul Mun, “Measurements of optical Feshbach resonances of  $^{174}\text{Yb}$  atoms”, *Phys. Rev. A* **94**, 042703 (2016).
- [Kit08] Masaaki Kitagawa, Katsunari Enomoto, Kentaro Kasa, Yoshiro Takahashi, Roman Ciuryło, Pascal Naidon and Paul S. Julienne, “Two-color photoas-

- sociation spectroscopy of ytterbium atoms and the precise determinations of s-wave scattering lengths”, *Phys. Rev. A* **77**, 012719 (2008).
- [Köh06] Thorsten Köhler, Krzysztof Góral and Paul S. Julienne, “Production of cold molecules via magnetically tunable Feshbach resonances”, *Rev. Mod. Phys.* **78**, 1311 (2006).
- [Kra09] Sebastian Kraft, Felix Vogt, Oliver Appel, Fritz Riehle and Uwe Sterr, “Bose-Einstein condensation of alkaline earth atoms:  $^{40}\text{Ca}$ ”, *Phys. Rev. Lett.* **103**, 130401 (2009).
- [Kul12] A. P. Kulosa, J. Friebe, M. P. Riedmann, A. Pape, T. W. Wübbena, D. B. Fim, S. Rühmann, K. H. Zipfel, H. Kelkar, W. Ertmer and E. M. Rasel, “An ultraviolet laser system for laser cooling and trapping of metastable magnesium”, arXiv:1201.3856v1 [physics.atom-ph] (2012).
- [Leg08] T. Legero, J. S. R. Vellore Winfred, Ch. Lisdat, F. Riehle and U. Sterr, “Towards an Optical Lattice Clock with Bosonic Strontium”, in: *Proceedings of the 7th symposium frequency standards and metrology* (2008).
- [Lel87] L. P. Lellouch and L. R. Hunter, “Measurement of the  $4s4p^1P-4s3d^1D$  spontaneous emission rate in calcium by use of a Stark-electric-quadrupole interference”, *Phys. Rev. A* **36**, 3490 (1987).
- [McG15] B. H. McGuyer, M. McDonald, G. Z. Iwata, M. G. Tarallo, A. T. Grier, F. Apfelbeck and T. Zelevinsky, “High-precision spectroscopy of ultracold molecules in an optical lattice”, *New J. Phys.* **17**, 055004 (2015).
- [Met99] Harold J. Metcalf and Peter van der Straten, *Laser Cooling and Trapping*, (Springer, New York, Berlin, Heidelberg, 1999) .
- [Mil94] Y. Millerioux, D. Touahri, L. Hilico, A. Clairon, R. Felder, F. Biraben and B. de Beauvoir, “Towards an accurate frequency standard at  $\lambda = 778$  nm using a laser diode stabilized on a hyperfine component of the Doppler-free two-photon transitions in rubidium”, *Opt. Commun.* **108**, 91 (1994).
- [Müt13] H. Mütinga, H. Ahlers, M. Krutzik, A. Wenzlawski, S. Arnold, D. Becker, K. Bongs, H. Dittus, H. Duncker, N. Gaaloul, C. Gherasim, E. Giese, C. Grzeschik, T. W. Hänsch, O. Hellmig, W. Herr, S. Herrmann, E. Kajari, S.

- Kleinert, C. Lämmerzahl, W. Lewoczko-Adamczyk, J. Malcolm, N. Meyer, R. Nolte, A. Peters, M. Popp, J. Reichel, A. Roura, J. Rudolph, M. Schiemangk, M. Schneider, S. T. Seidel, K. Sengstock, V. Tamma, T. Valenzuela, A. Vogel, R. Walser, T. Wendrich, P. Windpassinger, W. Zeller, T. van Zoest, W. Ertmer, W. P. Schleich and E. M. Rasel, “Interferometry with Bose-Einstein Condensates in Microgravity”, *Phys. Rev. Lett.* **110**, 093602 (2013).
- [Nap94] R. Napolitano, J. Weiner, Carl. J. Williams and Paul S. Julienne, “Line Shapes of High Resolution Photoassociation Spectra of Optically Cooled Atoms”, *Phys. Rev. Lett.* **73**, 1352 (1994).
- [Naz06] T. Nazarova, F. Riehle and U. Sterr, “Vibration-insensitive reference cavity for an ultra-narrow-linewidth laser”, *Appl. Phys. B* **83**, 531 (2006).
- [Naz07] Tatiana Nazarova, *Towards the Quantum Noise Limit in Ramsey-Bordé Atom Interferometry*, PhD thesis Fakultät für Mathematik und Physik der Gottfried Wilhelm Leibniz Universität Hannover 2007 Online available at <http://www.tib.uni-hannover.de>.
- [Naz08] Tatiana Nazarova, Christian Lisdat, Fritz Riehle and Uwe Sterr, “Low-frequency-noise diode laser for atom interferometry”, *J. Opt. Soc. Am. B* **25**, 1632 (2008).
- [Nic15a] T. L. Nicholson, S. Blatt, B. J. Bloom, J. R. Williams, J. W. Thomsen, J. Ye and Paul S. Julienne, “Optical Feshbach resonances: Field-dressed theory and comparison with experiments”, *Phys. Rev. A* **92**, 022709 (2015).
- [Nic15b] T. L. Nicholson, S. L. Campbell, R. B. Hutson, G. E. Marti, B. J. Bloom, R. L. McNally, W. Zhang, M. D. Barrett, M. S. Safronova, G. F. Strouse, W. L. Tew and J. Ye, “Systematic evaluation of an atomic clock at  $2 \times 10^{-18}$  total uncertainty”, *Nature Com.* **6**, 6896 (2015).
- [Pac17] Evgenij Pachomow, Veit Peter Dahlke, Eberhard Tiemann, Fritz Riehle and Uwe Sterr, “Ground-state properties of  $\text{Ca}_2$  from narrow-line two-color photoassociation”, *Phys. Rev. A* **95**, 043422 (2017).



- [Pei04] E. Peik, B. Lipphardt, H. Schnatz, T. Schneider, Chr. Tamm and S. G. Karshenboim, “Limit on the Present Temporal Variation of the Fine Structure Constant”, *Phys. Rev. Lett.* **93**, 170801 (2004).
- [Per98] H. Perrin, A. Kuhn, I. Bouchoule and C. Salomon, “Sideband cooling of neutral atoms in a far-detuned optical lattice”, *Europhys. Lett.* **42**, 395 (1998).
- [Rei12] G. Reinaudi, C. B. Osborn, M. McDonald, S. Kotochigova and T. Zelevinsky, “Optical Production of Stable Ultracold  $^{88}\text{Sr}_2$  Molecules”, *Phys. Rev. Lett.* **109**, 115303 (2012).
- [Res18] B. J. Reschovsky, B. P. Ruzic, H. Miyake, N. C. Pisenti, P. S. Julienne and G. K. Campbell, “Narrow-line photassociation spectroscopy and mass-scaling of bosonic strontium”, arXiv:1808.06507 [physics.atom-ph] (2018).
- [Rie04] Fritz Riehle, *Frequency Standards: Basics and Applications*, (Wiley-VCH, Weinheim, 2004) .
- [Rob19] B. M. Roberts, P. Delva, A. Al-Masoudi, A. Amy-Klein, C. Bærentsen, C. F. A. Baynham, E. Benkler, S. Bilicki, W. Bowden, E. Cantin, E. A. Curtis, S. Dörscher, F. Frank, P. Gill, R. M. Godun, G. Grosche, A. Hees, I. R. Hill, R. Hobson, N. Huntemann, J. Kronjäger, S. Koke, A. Kuhl, R. Lange, T. Legero, B. Lipphardt, C. Lisdat, J. Lodewyck, O. Lopez, H. S. Margolis, H. Álvarez-Martínez, F. Meynadier, F. Ozimek, E. Peik, P.-E. Pottie, N. Quintin, R. Schwarz, C. Sanner, M. Schioppo, A. Silva, U. Sterr, Chr. Tamm, R. LeTargat, P. Tuckey, G. Vallet, T. Waterholter, D. Xu and P. Wolf, “Search for transient variations of the fine structure constant and dark matter using fiber-linked optical atomic clocks”, arXiv:1907.02661 [astro-ph.CO] (2019).
- [She08] A. Shelkownikov, R. J. Butcher, C. Chardonnet and A. Amy-Klein, “Stability of the Proton-to-Electron Mass Ratio”, *Phys. Rev. Lett.* **100**, 150801 (2008).
- [Sim02] A. Simoni, P. S. Julienne, E. Tiesinga and C. J. Williams, “Intensity effects in ultracold photoassociation line shapes”, *Phys. Rev. A* **66**, 063406 (2002).

- [Ste03] Uwe Sterr, Tomas Binnewies, Carsten Degenhardt, Guido Wilpers, Jürgen Helmcke and Fritz Riehle, “Prospects of Doppler cooling on forbidden lines”, *J. Opt. Soc. Am. B* **20**, 985 (2003).
- [Vog07] F. Vogt, Ch. Grain, T. Nazarova, U. Sterr, F. Riehle, Ch. Lisdat and E. Tiemann, “Determination of the calcium ground state scattering length by photoassociation spectroscopy at large detunings”, *Eur. Phys. J. D* **44**, 73 (2007).
- [Vog09] Felix Vogt, *Creation of cold and dense ensembles of calcium atoms*, PhD thesis Gottfried Wilhelm Leibniz Universität Hannover 2009 Online available at <http://www.tib.uni-hannover.de>.
- [Wei03] M. Weidemüller and C. Zimmermann, *Cold Atoms and Molecules*, (Wiley-VCH, 2003).
- [Wig48] Eugene P. Wigner, “On the Behavior of Cross Sections Near Thresholds”, *Phys. Rev.* **73**, 1002 (1948).
- [Yan13] Mi Yan, B. J. DeSalvo, B. Ramachandhran, H. Pu and T. C. Killian, “Controlling Condensate Collapse and Expansion with an Optical Feshbach Resonance”, *Phys. Rev. Lett.* **110**, 123201 (2013).
- [Zel06] T. Zelevinsky, M. M. Boyd, A. D. Ludlow, T. Ido, J. Ye, R. Ciuryło, P. Naidon and P. S. Julienne, “Narrow Line Photoassociation in an Optical Lattice”, *Phys. Rev. Lett.* **96**, 203201 (2006).

# Publications

## Conference contributions

- Uwe Sterr, Evgenij Pachomow, Veit Dahlke, Eberhard Tiemann and Fritz Riehle  
*Ground-state properties of  $Ca_2$  from narrow-line two-color photoassociation* 23rd International Conference on Laser Spectroscopy, Arcachon (poster) 2017
- Veit Dahlke, Evgenij Pachomow, Eberhard Tiemann, Fritz Riehle and Uwe Sterr  
*Precision two-color spectroscopy of  $^{40}Ca$  for the determination of the s-wave scattering length*  
Deutsche physikalische Gesellschaft Frühjahrstagung, Mainz (talk) 2017
- Veit Dahlke, Evgenij Pachomow, Eberhard Tiemann, Uwe Sterr and Fritz Riehle  
*Two-colour photoassociation spectroscopy in  $^{40}Ca$  near the  $^3P_1 - ^1S_0$  asymptote*  
International Workshop on Ultracold Group II Atoms, Paris (poster) 2016
- Veit Dahlke, Evgenij Pachomow, Eberhard Tiemann, Uwe Sterr and Fritz Riehle  
*Understanding two-colour photoassociation and applications for ultracold molecules*  
Research training group 1729 workshop, Hildesheim (talk) 2016
- Veit Dahlke, Evgenij Pachomow, Eberhard Tiemann, Uwe Sterr and Fritz Riehle  
*Analysis of lineshapes and broadening mechanisms of two color-photoassociation spectra of  $^{40}Ca$*   
Research training group 1729 evaluation, Hannover (poster) 2016
- Veit Dahlke, Evgenij Pachomow, Eberhard Tiemann, Uwe Sterr and Fritz Riehle  
*Precision two-color spectroscopy of long-range ground-state vibrational levels in ultracold  $^{40}Ca$*   
Deutsche physikalische Gesellschaft Frühjahrstagung, Hannover (poster) 2016
- Uwe Sterr, Evgenij Pachomow, Veit Dahlke, Eberhard Tiemann and Fritz Riehle  
*Lineshapes in narrow-line one and two-color photoassociation of ultracold calcium*  
23th international conference on spectral line shapes, Torun (talk) 2016

- Fritz Riehle, Evgenij Pachomow, Max Kahmann, Veit Dahlke, Eberhard Tiemann and Uwe Sterr  
*One and two-colour photoassociation spectroscopy in  $^{40}\text{Ca}$  near the  $^3P_1 - ^1S_0$  asymptote*  
International conference on laser spectroscopy, Singapore (poster) 2015
- Veit Dahlke, Evgenij Pachomow, Eberhard Tiemann, Uwe Sterr and Fritz Riehle  
*Prospects of high precision spectroscopy of ultracold calcium molecules in an optical lattice*  
Research training group 1729 workshop, Celle (talk) 2015
- Evgenij Pachomow, Veit Dahlke, Eberhard Tiemann, Uwe Sterr and Fritz Riehle  
*Improved ground-state scattering length of calcium by two-color photoassociation*  
Gordon research conference / atomic physics, Newport RI (poster) 2015
- Veit Dahlke, Evgenij Pachomow, Eberhard Tiemann, Uwe Sterr and Fritz Riehle  
*Improved ground-state scattering length of  $^{40}\text{Ca}$  by two-color photoassociation*  
Deutsche physikalische Gesellschaft Frühjahrstagung, Heidelberg (poster) 2015

## Referred publications

- Evgenij Pachomow, Veit Dahlke, Eberhard Tiemann, Fritz Riehle and Uwe Sterr  
*Ground-state properties of  $\text{Ca}_2$  from narrow line two-color photoassociation*  
Phys. Rev. A, 2017, 95, 043422

# Danksagung

An dieser Stelle möchte ich allen danken, die mich in meiner Studienzeit und während der Arbeit bei der PTB und der Anfertigung dieser Arbeit unterstützt haben. Leider haben mich in dieser Zeit so viele Menschen beeinflusst, dass es unmöglich wäre, jeden namentlich zu erwähnen, weshalb ich mich auf die für mich wichtigsten beschränken möchte:

- Meine Eltern Elke und Peter Dahlke, die es mir ermöglicht haben, ein Studium der Physik aufzunehmen, und in jeder Lebenslage für mich da sind,
- Herrn Prof. Dr. Fritz Riehle und Herrn Dr. Uwe Sterr für die Möglichkeit, meine Dissertation am Calcium Experiment in der PTB durchzuführen, und immer ihr Bestes versucht haben mich zu fördern,
- Herrn Prof. Dr. Eberhard Tiemann für die Unterstützung mit theoretischen Berechnungen, die Diskussion der experimentellen und theoretischen Ergebnisse und nicht zuletzt für seine Bereitschaft als Prüfer für meine Arbeit zu fungieren,
- Herrn Dr. Evgenij Pachomov für die gemeinsame Zeit am Experiment. Ich habe stets bewundert, wie fleißig und gewissenhaft du gearbeitet hast, und werde immer dankbar sein für deine Anleitung und Erklärung des umfangreichen Aufbaus,
- Herrn M. Sc. Florian Krause für die gemeinsame Zeit im Büro und die netten Gespräche auch außerhalb der Arbeit,
- Frau Susanne Ehrenpfordt und Frau Birgit Ohlendorf für die Unterstützung in den Verwaltungsvorgängen und allen Formalien.

# Curriculum Vitæ

---

---

## Persönliche Daten

Name	Veit Peter Dahlke
Anschrift	Hannoversche Straße 11, 38116 Braunschweig
Telefon	+49 151 40609060
E-Mail	veit.dahlke@gmail.com
Geburtsdaten	12. März 1988 in Magdeburg
Staatsbürgerschaft	Deutsch
Familienstand	ledig
Führerschein	B
2000 – 2007	<b>Allgemeine Hochschulreife</b> , <i>Gymnasium Salzgitter-Bad</i> , Salzgitter, Abschlussnote: 1,4. Leistungskurse: Mathematik, Physik

---

## Ausbildung

10/2008 – 09/2011	<b>B.Sc. Physik</b> , <i>Technische Universität Carolo-Wilhemina</i> , Braunschweig, Abschlussnote: 1,6. Thema der Bachelorarbeit: <i>Erstellung von Energiespektrogrammen aus Simulationsergebnissen und Vergleich mit Cassini-Messungen für den Saturnmond Enceladus</i>
10/2011 – 04/2014	<b>M.Sc. Particle Physics</b> , <i>Georg-August-Universität</i> , Göttingen, Abschlussnote: 1,8. Thema der Masterarbeit: <i>Reconstruction of <math>t\bar{t}H(H \rightarrow b\bar{b})</math> events with the ATLAS experiment at the LHC</i>

---

## Berufserfahrung

09/2014 – vsl. 02/2020	<b>Wissenschaftler mit Ziel Promotion</b> , <i>Physikalisch technische Bundesanstalt</i> , Braunschweig, Schwerpunkte: Lasertechnik, Regelungstechnik, Simulation von Absorptionsspektren (C++, MathCad), Analyse von Messdaten, Veröffentlichung und Präsentation von Messergebnissen. Dissertation: <i>High power photoassociation spectroscopy in ultra-cold calcium</i>
---------------------------	--